TOHOKU UNIVERSITY

DOCTORAL THESIS

Collective Transition Behaviors of Coupled Phase Oscillators with Frustration
（フラストレーションを伴う結合位相振動子の集団転移挙動）

Author:
Bojun Li

Supervisor:
Nariya Uchida

Department of Physics
Graduate School of Science

February 25, 2025

TOHOKU UNIVERSITY

Abstract

Department of Physics
Graduate School of Science

Doctor of Science

Collective Transition Behaviors of Coupled Phase Oscillators with Frustration

by Bojun Li

Synchronization is a fundamental phenomenon observed in nature, where coupled systems adjust their rhythms to achieve coherence. It plays a vital role in diverse areas, from biological systems like circadian rhythms and neuronal activity to engineered systems such as power grids and wireless networks. One intriguing aspect of collective dynamics of oscillators is the emergence of chimera states, where synchronized and desynchronized regions coexist within the same system. These states have profound implications for understanding brain function, diagnosing neurological disorders, and improving the stability of complex networked systems.

Motivated by the intrinsic role of synchronization in brain networks, this dissertation aims to investigate how frustration—introduced through phase delays—affects the dynamics of coupled oscillator systems. The research focuses on uncovering the mechanisms that give rise to complex dynamical behaviors, such as chimera states and metastability, and understanding how these states transition under different conditions. To achieve this, the study examines three distinct scenarios:

Nonlocally Coupled Oscillators with Repulsive Coupling: This study explores the effects of frustration in nonlocally coupled oscillators with repulsive interactions. By comparing these systems to Z2-symmetric directed percolation, similarities such as absorbing state transitions and the dynamics of incoherent regions are identified, alongside unique features like traveling wave emissions from incoherent regions.

Mobile Oscillator Systems: Extending the scope to mobile oscillators, the second study examines how mobility influences synchronization. It is shown that mobility changes the basin of attraction of the twisted states, stabilizes those with small twisted numbers, and modifies spatiotemporal patterns by dynamically altering coupling interactions. These findings bridge theoretical insights with applications in mobile sensor networks and neuronal rewiring dynamics.

Hierarchical Networks of Oscillators: The third study focuses on multiple populations of oscillators interacting through hierarchical coupling structures. This framework reveals how hierarchical coupling facilitates metastable dynamics, enabling transitions between synchronization and partial synchronization. These findings are particularly relevant for understanding metastability in brain networks.

By addressing these scenarios, this dissertation contributes to a deeper understanding of how frustration shapes synchronization and chimera state in coupled systems, with broad implications for neuroscience, network engineering, and other interdisciplinary fields where synchronization is critical.

Contents

Chapter 1

Introduction

1.1 Basic conception

Synchronization is a ubiquitous phenomenon in nature, where coupled oscillators spontaneously adjust their rhythms to oscillate in unison. Synchronization plays a crucial role in various biological, physical, and social systems [124]. For example, circadian clock [81, 87, 147], flashing fireflies [15], the dynamics of cilia and flagella [44], gait pattern of animals and human [25, 148], metabolic oscillations [26, 41], phytoplankton population oscillations [99], power grids [28, 29, 35, 103] and consensus formation in social population [48].

The study of synchronization has been greatly facilitated by the concept of phase oscillators. Phase oscillators are simplified models that capture the essential dynamics of oscillatory systems, focusing on the evolution of their phases while neglecting the amplitude variations. The most celebrated model of phase oscillators is the Kuramoto model, proposed by Yoshiki Kuramoto [74]. The Kuramoto model consists of a population of coupled phase oscillators, each characterized by its natural frequency and coupled to others through a sinusoidal interaction. The model has been widely studied due to its mathematical tractability and its ability to capture the essence of synchronization phenomena.

One of the key features of the Kuramoto model is the existence of a critical coupling strength, above which the oscillators spontaneously synchronize. This synchronization transition is characterized by the emergence of a collective rhythm, where the oscillators' phases become locked, despite their inherent frequency differences. The Kuramoto model has been extended in various ways to incorporate more realistic features, such as time delays [4, 21, 31, 32, 62, 102, 109, 137, 149, 172], complex network topologies [8, 131, 136, 152, 175], and noises [6, 43, 60, 110]. These extensions have expanded

the applicability of the model to a wide range of real-world systems, from power grids to social networks.

The study of synchronization and phase oscillators has also led to the discovery of intriguing dynamical phenomena, such as chimera states. Chimera states are characterized by the coexistence of synchronized and desynchronized regions in a network of identical oscillators. The emergence of chimera states in phase oscillator models has attracted significant attention due to their counterintuitive nature and potential implications for real-world systems.

Section 1.1 lays the foundation for understanding the collective behavior of coupled oscillatory systems. By exploring the fundamental concepts and models, such as the Kuramoto model, this section sets the stage for the investigation of more complex dynamical phenomena, including chimera states, which are the focus of the subsequent sections.

1.1.1 Phase oscillators

Since our goal is to study the collective behavior of a network of oscillating units, representing each unit as a high-dimensional dynamical system would make the analysis excessively complex. A common solution is phase reduction, which transforms each oscillatory unit into a phase oscillator. This technique simplifies the description of complex oscillatory systems by focusing on the essential dynamics of a single periodic phase variable for each unit, significantly reducing the system's dimensionality and facilitating the study of collective dynamics (see review [5, 123]).

Denoting the variables $X_i (i = 1, \cdots, M)$ of a degree-M system undergoing limit cycle oscillation as $\mathbf{X}$, it can be described by the following differential equation:

$$\frac{d\mathbf{X}}{dt} = \mathbf{F}(\mathbf{X}) \tag{1.1}$$

This equation has a stable periodic solution $\mathbf{X}(t)$ that revolves around a limit cycle orbit in the state space with period T. By setting an appropriate starting point on the orbit as phase $\theta = 0$ and advancing time from there, the phase increases, and when $\theta = 2\pi$, it returns to the starting point and the phase velocity can be defined as $d\theta/dt = 2\pi/T = \omega$ (Fig. 1.1). The phase of an arbitrary point $\mathbf{X}$ in phase space can be represented by $\theta(\mathbf{X})$ and the phase velocity is

$$\dot{\theta}(t) = \dot{\theta}(\mathbf{X}(t)) = \nabla_{\mathbf{X}}\theta(\mathbf{X}) \cdot \mathbf{F}(\mathbf{X}) \tag{1.2}$$

On the limit cycle, θ gradually increases from 0 to 2π. However, when the oscillator is perturbed, its state temporarily deviates from the limit cycle, necessitating an extension of the phase definition to points outside the limit cycle. Since any trajectory starting within the attraction region of the limit cycle will eventually asymptotically approach it, we consider that the set of initial points that converge to the same state originally share the same phase. This concept allows for the definition of isochrons in the phase space (Fig. 1.2). Analytically, we can uniquely assign a phase to each point in the attraction basin of the limit cycle, by defining $\nabla_{\mathbf{X}}\theta(\mathbf{X}) \cdot \mathbf{F} = \omega$. However, it is rare to obtain an analytical solution for the limit cycle in most cases. Practically, the phase $\theta(\mathbf{X})$ of a given point can be determined numerically by comparing the time it takes for that point to evolve and pass through a reference point with the time taken by a point starting from the limit cycle.

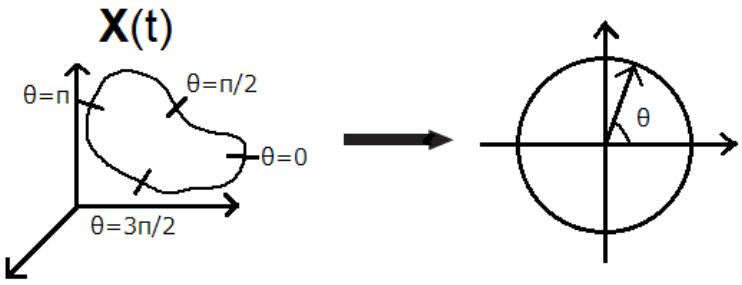

FIGURE 1.1: Conceptual diagram of phase reduction.

When an oscillator with phase θ at state $\mathbf{X}_0(\theta)$ is perturbed and moved to the position $X = \mathbf{X}_0(\theta) + I$, we can define its phase response function.

$$g(\theta; \mathbf{I}) = \theta(\mathbf{X}_0(\theta)_{\mathbf{I}}) - \theta \tag{1.3}$$

Here, we consider weakly coupled oscillators, where "weak" means that for each oscillator, the perturbation caused by external forces or internal coupling is much smaller than the change in the oscillator's own state variables. So that it can be approximated by

$$g(\theta; \mathbf{I}) \approx \nabla_{\mathbf{X}}\theta(\mathbf{X})|_{\mathbf{X}=\mathbf{X}_0(\theta)} \cdot \mathbf{I} = \mathbf{Z}(\theta) \cdot \mathbf{I} \tag{1.4}$$

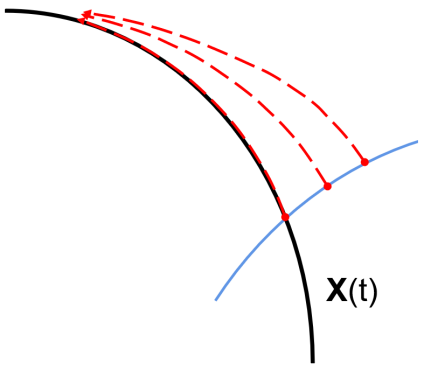

FIGURE 1.2: The trajectories starting from two initial points (red dashed lines) near the limit cycle (black line) asymptotically approach the state of a trajectory starting from a certain initial point on the limit cycle. Therefore, these three points are considered to have the same phase. The set of all such points forms an isochron (blue line).

where $\mathbf{Z}(\theta) = \nabla_{\mathbf{X}}\theta(\mathbf{X})|_{\mathbf{X}=\mathbf{X}_0(\theta)}$ is call the phase sensitivity function. When a large number of oscillators with similar intrinsic dynamics interact, the time evolution of the i-th oscillator is as follows:

$$\frac{d\mathbf{X}_i}{dt} = \mathbf{F}(\mathbf{X}_i) + \delta\mathbf{F}_i(\mathbf{X}_i) + \sum_j V_{ij}(\mathbf{X}_i, \mathbf{X}_j) \tag{1.5}$$

$\mathbf{F}(\mathbf{X}_i)$ is the common dynamics of all oscillators with a stable periodic solution $\mathbf{X}(t)$. $\delta\mathbf{F}_i(\mathbf{X}_i)$ represents the small differences between oscillators. $V_{ij}(\mathbf{X}_i, \mathbf{X}_i)$ is the interaction between oscillators, and we assume that the interaction is weak and that the small differences and interactions between oscillators only slightly alter the shape of the limit cycle orbit, with each oscillator moving in the vicinity of the original limit cycle. According to Eq.(1.2) the dynamics of the phase is

$$\begin{aligned}\dot{\theta}_i(t) &= \nabla_{\mathbf{X}}\theta(\mathbf{X}_i) \cdot \left\{ \mathbf{F}(\mathbf{X}_i) + \delta\mathbf{F}_i(\mathbf{X}_i) + \sum_j V_{ij}(\mathbf{X}_i, \mathbf{X}_j) \right\} \\ &= \omega + \nabla_{\mathbf{X}}\theta(\mathbf{X}_i) \cdot \left\{ \delta\mathbf{F}_i(\mathbf{X}_i) + \sum_j V_{ij}(\mathbf{X}_i, \mathbf{X}_j) \right\}\end{aligned} \tag{1.6}$$

By replacing $\mathbf{X}_i$ (whose phase is $\theta(\mathbf{X}_i)$) with the corresponding point on the limit cycle that has the same phase $\mathbf{X}_0(\theta_i)$, we obtain

$$\begin{aligned}\dot{\theta}_i(t) &\approx \omega + \nabla_{\mathbf{X}}\theta(\mathbf{X})|_{X=X_0(\theta_i)} \cdot \left\{ \delta\mathbf{F}_i(\mathbf{X}_0(\theta_i)) + \sum_j V_{ij}(\mathbf{X}_0(\theta_i), \mathbf{X}_0(\theta_j)) \right\} \\ &= \omega + \mathbf{Z}(\theta_i) \cdot \left\{ \delta\mathbf{F}_i(\theta_i) + \sum_j V_{ij}(\theta_i, \theta_j) \right\} \end{aligned} \tag{1.7}$$

Since the effects of coupling and inhomogeneity are sufficiently small, we can perform an averaging approximation. By introducing a new phase variable $\phi_i = \theta_i - \omega t$ that removes the constant rotation component ωt from each phase θ_i, Eq.(1.7) becomes

$$\dot{\phi}_i(t) = \mathbf{Z}(\phi_i + \omega t) \cdot \left\{ \delta\mathbf{F}_i(\phi_i + \omega t) + \sum_{i=1} V_{ij}(\phi_i + \omega t, \phi_j + \omega t) \right\} \tag{1.8}$$

Since the right-hand side is small, ϕ_i changes slowly, thus, if we fix ϕ_i at its value at time t and average over a limit cycle period, then by reverting to the original phase variable θ_i, we obtain the simplified phase equation:

$$\dot{\theta}_i(t) = \omega_i + \sum_j \Gamma_{ij}(\theta_i - \theta_j) \tag{1.9}$$

This function depends only on the phase difference, making the subsequent analysis much easier.

The phase reduction technique has been widely used in the study of coupled oscillators, as it allows for a tractable mathematical analysis of their collective dynamics. By reducing each oscillator to its phase variable and coupling them through the phase differences, we obtain a simplified model that captures the essential synchronization properties of the system.

1.1.2 Synchronization and Kuramoto model

The Kuramoto model is a well-known model for explaining synchronization phenomena. It consists of N phase oscillators with sine-type all-to-all (global) coupling, where the phases follow the equation:

$$\frac{d\theta_i}{dt} = \omega_i - \frac{K}{N} \sum_{j=1}^{N} \sin(\theta_i - \theta_j), \quad i = 1, \cdots, N. \tag{1.10}$$

K represents the coupling strength, and the natural frequency ω_i of the i-th oscillator follows a certain distribution $g(\omega)$. The state of the entire system can be represented using the complex order parameter:

$$Z(t) = R(t)e^{i\Theta(t)} = \frac{1}{N}\sum_{j=1}^{N} e^{i\theta_j(t)} \tag{1.11}$$

$R(t)$ represents the degree of synchronization among the oscillators and is similar to the magnetization in the 2D XY model. $R = 0$ corresponds to the disordered state, while $R = 1$ corresponds to the state where the phases are completely aligned. Θ represents the average phase. Using Equation (1.11), the time evolution of the oscillators' phases (1.10) can be written as:

$$\frac{d\theta_i}{dt} = \omega_i - KR\sin(\theta_i - \Theta) \tag{1.12}$$

This equation means that the i-th oscillator interacts with the order parameters R and Θ, which represent the state of the entire system. As $t \to \infty$, the system reaches a dynamically steady state, and the order parameters become:

$$R = R(K), \quad \Theta = \Omega t \tag{1.13}$$

The average phase velocity Ω of the entire system is not related to the discussion of synchronization, so it can be set to 0 without loss of generality. The deviation of the phase from the average, $\psi_i = \theta_i - \Theta$, becomes:

$$\frac{d\psi_i}{dt} = \omega_i - KR\sin\psi_i \tag{1.14}$$

From Equation (1.14), it can be seen that the oscillators form two groups. One group consists of oscillators with $\omega_i < KR$ and moves with the same phase velocity as the average phase velocity, i.e., $\dot{\psi}_i = 0$. The other group consists of oscillators with $\omega_i > KR$ and does not have a solution for $\dot{\psi}_i = 0$, moving with a different phase velocity than the average phase velocity. The steady-state distribution of the phases for the former group of oscillators is $\psi_i = \sin^{-1}(\omega/KR)$. On the other hand, the phase distribution for the latter group is determined by the observation that the time spent by each oscillator is inversely proportional to its phase velocity. Summing up the

two distributions, we obtain the phase distribution function $n(\psi)$ that depends on the distribution of the natural frequency $g(\omega)$. Using the relation $W(t) = \int_0^{2\pi} n(\psi)e^i\phi d\psi$ or equivalently $R = \int_0^{2\pi} n(\psi)\cos(\psi)d\psi$, a self-consistent equation for R can be derived:

$$R = KR\int_{-2/\pi}^{2/\pi} g(KR\sin\psi)(cos^2\psi)d\psi \tag{1.15}$$

From this, the critical coupling strength necessary for synchronization is obtained:

$$K_c = \frac{2}{\pi g(0)} \tag{1.16}$$

For example, if the natural frequency distribution $g(\omega)$ is Gaussian, the system is non-synchronous with $R = 0$ for $K < K_c$. When K exceeds K_c, R rises in proportion to $(K - K_c)^{\frac{1}{2}}$, and a collective synchronization transition occurs (Figure 1.3). The above Kuramoto model assumes that the oscillators

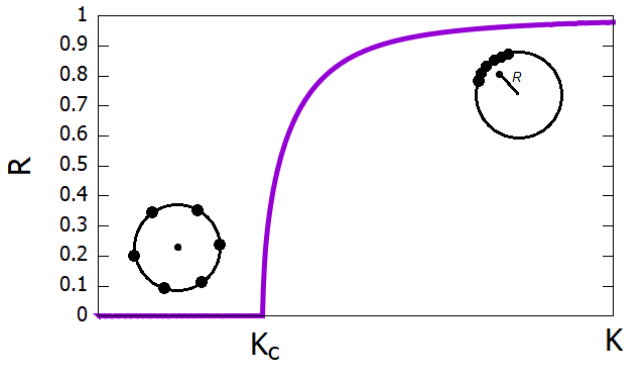

FIGURE 1.3: Dependence of the order parameter R on K in the Kuramoto model.

are globally coupled; however, the properties of a phase oscillator system strongly depend on the coupling scheme, including the coupling function, coupling distance, and natural frequency. For example, nearest-neighbor (local) couplings or short-range (non-local) couplings on a regular lattice are not sufficient to induce synchronization transition. On the other hand, a long-range coupling that decays with an inverse power of the distance induces global synchronization if the exponent of the power law α satisfies $\alpha \leq 3d/2$, where d is the spatial dimension [22], but a critical transition as found in the Kuramoto model is realized only for $\alpha \leq d$ [161].

1.1.3 Chimera states

Chimera states are a fascinating phenomenon observed in networks of coupled oscillators, where coherent and incoherent behaviors coexist within the same system. The term "chimera" is inspired by the mythological creature made up of disparate parts, reflecting the coexistence of distinct dynamical behaviors [1, 73].

Fig. 1.4 illustrates a typical chimera state, where the oscillators are arranged in a ring. The coherent parts are on the sides of the figure, where the oscillators have almost the same phase and frequency. In the middle of the figure, the incoherent part is shown, where the oscillators have different phases and drift at different frequencies.

The discovery of chimera states has spurred a series of new studies in the field of nonlinear coupled oscillators. Chimeras have also been observed in chemical [106, 107, 154, 158], mechanical [**martens2013chimera_mechanical**, 12, 67], optical [9, 140], electronic systems [40, 130]. On the other hand, theoretical research on chimera states, initially focused on one-dimensional ring networks, has gradually expanded to include two and three-dimensional [70, 88, 114, 142], multilayer networks [42, 50, 51, 66, 86, 89, 117]. A substantial body of research has investigated the effects of various coupling schemes and parameters on chimera states, uncovering a wide range of different types of chimeras.

Also, the discovery of chimera states has attracted significant attention due to their potential implications in various fields. In neuroscience, chimera states may offer insights into the mechanisms underlying brain disorders characterized by the coexistence of synchronized and desynchronized neural activity. In power grids, understanding chimera states could help prevent blackouts.

1.1.4 Different types of chimera states

As research on chimera states has progressed, researchers have discovered various types of chimera states in different oscillatory systems, including breathing chimera [2, 11, 78], alternating chimera [54, 90, 92] traveling chimera [101, 171], Amplitude mediated chimera [105, 138], amplitude chimera [7, 160, 173, 174], multichimera [63, 112, 113, 159], imperfect chimeras [67], spiral wave chimera [70, 142].

Spiral wave chimera: In two-dimensional nonlocally coupled oscillator systems, a chimera state can emerge consisting of coherent spiral waves with an incoherent region at their center. This phenomenon was first discovered

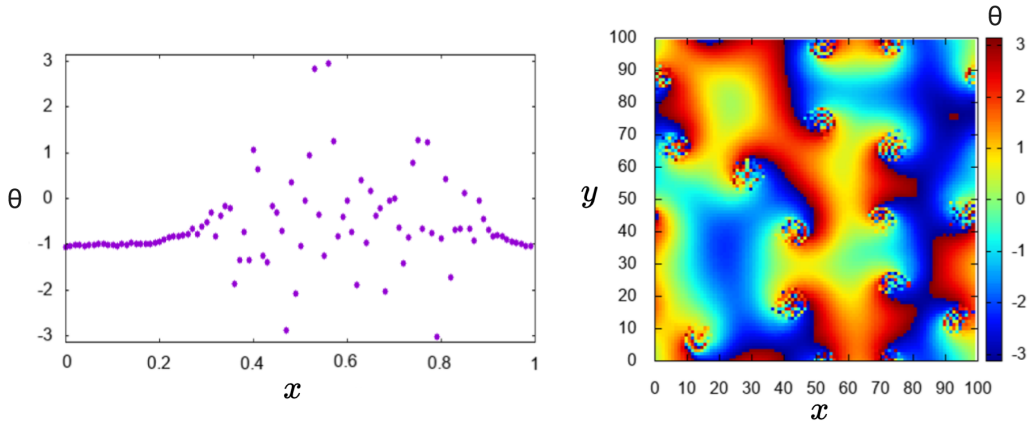

FIGURE 1.4: Spatial patterns of the phase θ in 1D and 2D chimera states. (a)1d chimera state, composed of an incoherent region (middle) and a coherent region (edge). (b) Spiral wave chimera state in 2d with incoherent cores.

by Shima and Kuramoto in [142]. The authors observed a critical radius within which the oscillators are incoherent and outside of which they are coherent. They also realized that the same phenomenon occurs in the distribution of the mean frequency. The frequency patterns are divided into two parts: in the outer region, the oscillators have the same frequency, while in the inner region, they have distributed frequencies. Kim and others further investigated these spiral patterns [70]. They studied the effect of phase-lagged coupling on the dynamics of a two-dimensional coupled oscillator array. They examined the following equation over the entire range of phase shifts α and found that varying α leads to various interesting spatial patterns.

$$\frac{\mathrm{d}\theta_{ij}}{\mathrm{d}t} = \omega_0 - \frac{K}{N(R)} \sum_{r_{mn,ij} \leq R} \sin(\theta_{ij} - \theta_{mn} + \alpha) \tag{1.17}$$

Here, $N(R)$ shows the number of the neighbors of each oscillator within a finite distance R. This is a 2D version of the non-local Kuramoto-Sakaguchi model. Figure 1.4(b) shows an example of phase patterns with system size $\mathcal{N} = 100^2$, $R = 6$, $\alpha = 0.25\pi$.

Multichimera: Omelchenko *et al.* discovered that enhancing the coupling between phase oscillators can lead to the formation of multiple coherent regions within the incoherent regions, which they termed multi-chimera state [113]. They considered a ring of nonlocally coupled FitzHugh-Nagumo (FHN) oscillators with both direct and cross-coupling. For smaller values of

coupling strength, this network exhibited classic chimera states with one coherent and one incoherent region. Increasing the coupling strength resulted in the formation of multiple incoherent regions. Multi-chimera states have also been found in nonlocally coupled Van der Pol oscillators [112], coupled pendulums [63], and networks of leaky integrate-and-fire models [159]. We will further explain the multichimera state in Section. 1.2.

1.1.5 Chimera state in neuronal system

The human brain contains as many as 86 billion neurons [56]. These neurons form networks and repeatedly fire, sending signals to each other, which is fundamental to brain function. We can consider each neuron as a periodically firing oscillating element, the synchronization and desynchronization of neuron populations play crucial roles in various processes. Some studies have shown the appearance of chimera states in neuronal networks, where the synchronized and desynchronized states coexist in the neuronal system [10, 65, 94, 141, 167]. They are classified into the following categories.

Bump state: Chimera state can potentially explain the "bump state" where synchronized neurons with constant firing rates at some spatial location and desynchronized neurons at other spatial positions. This state is crucial for many processes in the brain such as the operation of head direction cells [61].

Unihemispheric sleep: Another piece of evidence for chimera states is the unihemispheric slow-wave sleep. This is observed in some migratory birds and aquatic mammals like dolphins, where one brain hemisphere sleeps while the other remains awake [104, 127, 128]. This means they only shut down one brain hemisphere and close the opposite eye. At the same time, the other half of the brain monitors what is happening in the environment (for migratory birds) and controls breathing functions (for aquatic mammals). In this case, the neurons in the sleeping part of the brain oscillate synchronously, while the neurons in the awake hemisphere oscillate asynchronously.

Brain diseases: The synchronization and desynchronization of neurons are also related to brain diseases. For example, Parkinson's disease is said to occur due to the synchronization of neurons in the basal ganglia [14, 55]. Conversely, Alzheimer's disease is associated with a reduction in brain wave synchronization [72]. Epilepsy occurs when local synchronization increases while long-range synchronization decreases [19, 27].

1.2 Non-local Kuramoto-Sakaguchi model on a ring with a phase lag

In this section, we will discuss the properties of the Kuramoto-Sakaguchi model with a phase lag in the non-local coupling. Consider N coupled identical Kuramoto-Sakaguchi oscillators on a one-dimensional ring, whose dynamical equations are as follows:

$$\dot{\phi}(x,t) = \omega_0 - \sum_{x'} g(x-x') \sin\left(\phi(x,t) - \phi(x',t) + \alpha\right), \tag{1.18}$$

where $\phi(x,t)$ represents the phase of the oscillator at $x = 1, 2, ..., N$ at time t. The intrinsic phase velocity ω_0 is constant and set to zero without losing generality by the transformation $\phi \to \phi - \omega_0 t$. α in eq. (1.18) represents the phase lag, which, combined with the non-local coupling, introduces frustration into the system, leading to a variety of intriguing patterns. This model generalizes the original model introduced by Sakaguchi and Kuramoto [133], where a global coupling $g(x) = 1/N$ is assumed, to an arbitrary coupling function $g(x)$. For convenience in numerical simulations, we use the following coupling function:

$$g(x) \begin{cases} = \dfrac{1}{2R} & (|x| \leq R), \\ = 0 & (|x| > R). \end{cases} \tag{1.19}$$

where R is the coupling range. This system has two apparent solutions: global phase synchronization

$$\phi(x,t) = \Omega t, \tag{1.20}$$

and the twisted state

$$\phi(x,t) = \Omega t + \frac{2\pi q}{N} x. \tag{1.21}$$

where q is an integer with $|q| < \frac{N-1}{2}$. We will call q the winding number in the rest of the paper. In phase synchronization, all oscillators have the same phase, while the twisted state refers to a situation where each pair of neighboring oscillators maintains a constant phase difference. In both of these states, the oscillators drift at the same frequency, and therefore, they are referred to as coherent states.

For $\alpha < 0.5\pi$, the coupling is attractive. If α is sufficiently small, the system that started from a random initial condition eventually reaches a coherent state. When α exceeds a threshold, the frustration destroys coherence and

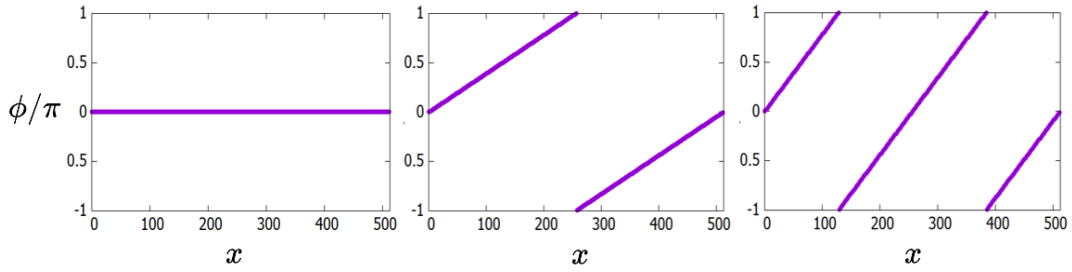

FIGURE 1.5: The phase profiles for (a) global synchronized state, (b) twisted state with $q = 1$, (c) twisted state with $q = 2$.

forms a chimera state or a multichimera state with many coherent and incoherent regions [91]. For a repulsive coupling, i.e. $\alpha > 0.5$, we find coexistence of twisted states with positive and negative phase differences separated by incoherent strips [84].

1.2.1 Attractive coupling

For $\alpha = 0$, i.e., no frustration, this model reduces to the Kuramoto model with uniform natural frequency, which has been researched extensively. In 2006, Wiley and colleagues investigated the ease of reaching the synchronized state in a population of oscillators [169]. They examined the basin of attraction of each fixed point in the system described by eq. (1.18). In the case of global coupling with a normalized coupling distance $r = R/N = 0.5$, the system eventually reaches global synchronization, regardless of the initial state. In this case, global synchronization of the oscillators is the only attractor in the phase space. As r decreases, new stable fixed points emerge when r falls below a critical value $r_c = 0.34$. The $q = \pm 1$ twisted states become stable first. As r decreases further, twisted states with other values of q also become stable. The basin of attraction of a fixed point is the set of states that converge to that fixed point. The larger the basin of attraction, the higher the probability that the system, starting from a randomly chosen initial state, will reach that fixed point.

When $0 < \alpha < 0.5\pi$, frustration under specific parameters can lead to the emergence of chimera states. The paper [91] investigated the dependency of chimera states on r and α. When α is small or the coupling is global, the coherent state is stable. As α approaches 0.5π, multichimera states with h incoherent domains occur, and the number of h increases as r decreases. When r becomes sufficiently small, a complex multi-chimera state with numerous

dynamically generating and annihilating incoherent domains emerges, referred to as phase turbulence in reference [30]. Next, I will introduce the multichimera states when $r \ll 1$ and the coherence-multichimera transition induced by changes in α [68].

In [68], Kawase and Uchida distinguished the states of the oscillators using the phase difference between adjacent oscillators

$$\Delta_x = \frac{\phi_{x+1} - \phi_x}{\pi}. \tag{1.22}$$

Domains where the phase difference is close to 0 indicate that the oscillators in that domain are phase-synchronized. Fig. 1.6(a) shows a spatiotemporal plot of the absolute value of the phase difference. In this plot, the horizontal axis represents the time evolution, and the vertical axis represents the positions of the oscillators on a one-dimensional ring. The plot reveals the presence of incoherent domains with large $|\Delta_x|$ (red) and coherent domains with small $|\Delta_x|$ (blue). The spatial profile of $|\Delta_x|$ along the white line is shown in Fig. 1.6(b). When we fix the coupling distance and gradually increase α, the

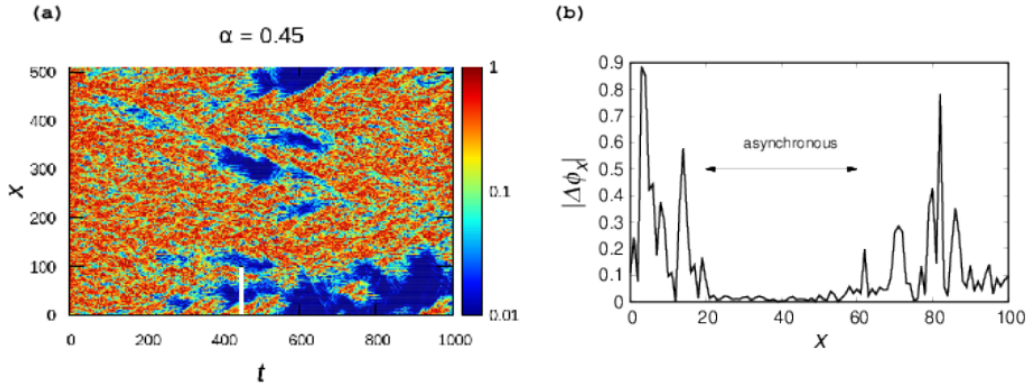

FIGURE 1.6: The multichimera state for $N = 512, R = 5, \alpha = 0.45\pi$. (a) The spatiotemporal pattern of the absolute value of the phase difference between neighbor oscillators $|\Delta_X|$. (b) The spatial profile of the phase difference along the white line in (a), where regions with large phase differences (red) correspond to incoherent domains and regions with small phase differences (blue) correspond to coherent domains. Reused from Ref. [68] with permission of the authors.

system transitions from a coherent state to a multichimera state at a critical value α_c. Fig. 1.7 shows the spatiotemporal plots of the system at different

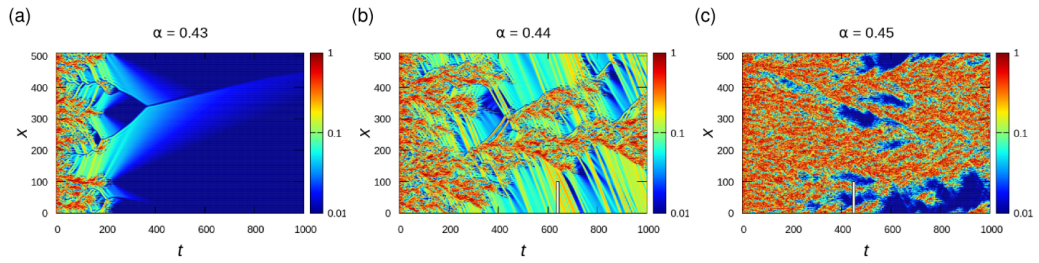

FIGURE 1.7: Spatiotemporal patterns of the phase difference $|\Delta_x|$. For $N = 512, R = 5$. (a) $\alpha = 0.43\pi$, coherent state. (b) $\alpha = 0.44\pi$, bifurcating incoherent domains and numerous traveling waves. (c) $\alpha = 0.45\pi$, a multi-chimera state with numerous incoherent and coherent domains. Reused from Ref. [68] with permission of the authors.

values of α: (a) $\alpha = 0.43\pi$, where the system enters a coherent state after an initial relaxation phase; (b) $\alpha = 0.44\pi$, where bifurcated incoherent domains and propagating waves emerge; (c) $\alpha = 0.45\pi$, where a state of coexistence between coherent and incoherent domains is observed. This type of change in the spatiotemporal plot of the system with varying α is referred to as the coherent-multichimera transition.

1.2.2 Analogy to directed percolation

These spatiotemporal patterns are similar to those of directed percolation phenomena, particularly in terms of the emergence of spatially disordered structures and bifurcating structures beyond a certain threshold.

Directed percolation (DP) refers to phenomena such as the downward infiltration of water in porous rocks due to gravity, the spread of forest fires, or infectious diseases [57]. Consider a square lattice, where each lattice point can be in one of two states: active (A) or inactive (I), with bonds between neighboring lattice points. In the case of porous rocks, the active state (A) corresponds to wet holes, and the inactive state (I) corresponds to dry holes. The connectivity of the system, i.e., the probability that a bond between any two lattice points is open, is denoted by p. The problem here is whether there exists an infinitely long path along open bonds starting from the origin. It is clear that when $p = 0$, such a path does not exist, and when $p = 1$, there are infinitely many such paths. However, how the probability of the existence of such a path changes for intermediate values of p is nontrivial. In reality, a continuous phase transition occurs at a threshold value $p = p_c$, where the

probability of the existence of an infinitely long path changes from 0 to non-zero. This model is called the bond DP.

To introduce the phase transition of DP, we use the simplest (1+1) dimensional Domany-Kinzel model (one spatial dimension, one temporal dimension). Fig. 1.8 shows a schematic diagram of the DK model. Each site s_i lined

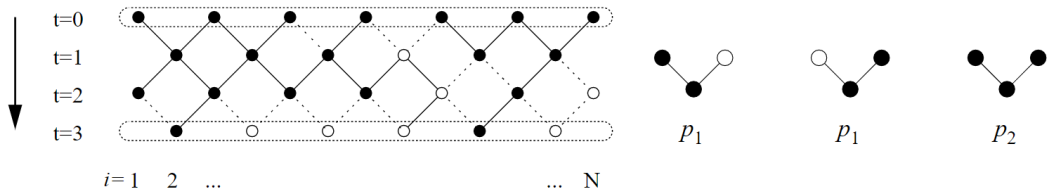

FIGURE 1.8: Configuration of (1+1)-dimensional Domany-Kinzel model and its transition probabilities

up horizontally can be in one of two states: active (black) or inactive (white). The system evolves downward in time, and the state of the i-th site at time $t+1$ is determined by the states of the $i-1$-th and $i+1$-th sites at time t. The transition probability $P(s_{i,t+1}|s_{i-1,t}, s_{i+1,t})$ of the Domany-Kinzel model is given by the following equations.

$$P(I|I,I) = 1 \tag{1.23}$$
$$P(A|A,A) = p_2 \tag{1.24}$$
$$P(A|I,A) = P(A|A,I) = p_1 \tag{1.25}$$

From eq.(1.23), it can be seen that if all sites become inactive, the system cannot escape from that state. This state is called an absorbing state. Eq. (1.24) means that there is a probability of $1-p2$ for an inactive region to occur within an active region. Eq. (1.25) indicates that the boundary between active and inactive regions fluctuates. In special cases of the Domany-Kinzel model, setting $p_2 = p_1(2-p_1)$ corresponds to the bond DP, and setting $p_2 = p_1$ corresponds to the so-called site DP. Fig. 1.9 shows an example of (1+1) dimensional site DP. Starting from a random initial state, the active sites (black) percolate downward along the time axis with a transition probability p. This system shows an inactive phase where percolation stops at a certain time for p_c and an active phase where percolation continues indefinitely for $p > p_c$. This is called an absorbing state transition. Letting $\rho(t) \in [0,1]$ denote the fraction of active sites in the entire system, after a sufficiently long time, $\rho(t)$ becomes 0 in the inactive phase and converges to a certain value ρ_∞ in the active phase. ρ_∞ changes continuously with p, and near the transition point,

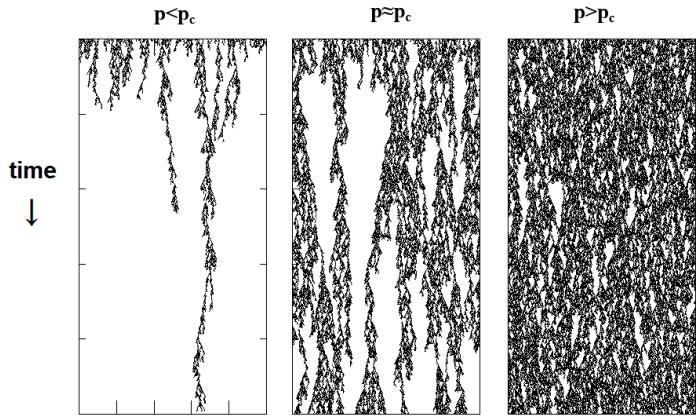

FIGURE 1.9: (1+1)-dimensional site DP. From left to right, inactive phase, transition point, and active phase, respectively.

ρ_∞ follows a power law.

$$\rho_\infty \sim (p - p_c)^\beta \tag{1.26}$$

Additionally, the characteristic length scales in the spatial and temporal directions, $\xi_\perp$ and $\xi_\parallel$ can be represented by the average size of the inactive regions in the active phase. These scales, like ρ_∞, have the following relationships with p and diverge at the transition point.

$$\xi_\perp \sim |p - p_c|^{-\nu_\perp}, \quad \xi_\parallel \sim |p - p_c|^{-\nu_\parallel} \tag{1.27}$$

These three critical exponents $(\beta, \xi_\perp, \xi_\parallel)$ characterize the critical behavior of the DP universality class, and other critical exponents are related to these three through scaling relations. Numerical calculations yield the critical exponents of (1+1) dimensional DP as $\beta = 0.276486, \xi_\perp = 1.096854, \xi_\parallel = 1.733847$ [57]. DP is a representative example of nonequilibrium phase transitions, and various systems, such as the Domany-Kinzel model, the contact process, and the Ziff-Gulari-Barshad model, belong to the DP universality class. In experimental systems, the transition from laminar flow to turbulence in Navier-Stokes fluids [82, 134] and the transition between two turbulent phases in liquid crystal electroconvection [150] can also be understood as DP absorbing state transitions.

Comparing the spatiotemporal patterns of the DP and KS models reveals very similar characteristics between the two:

1. Both models have two fundamental states: active/incoherent and inactive/coherent.

2. Both models have an absorbing state. When all sites become inactive/coherent, the system cannot escape from this state.

3. Both models exhibit phase transitions based on the parameters p (for DP) and α (for KS).

In Ref. [68] the authors discretized each oscillator's state into three categories: synchronized regions (s), asynchronous regions (a), and traveling waves (w). The three states are defined as follows:

$$|\Delta(x,t)| \in [0,\Delta_1], \quad (s) \tag{1.28}$$
$$|\Delta(x,t)| \in [\Delta_1,\Delta_2], \quad (w) \tag{1.29}$$
$$|\Delta(x,t)| \in [0,\Delta_1], \quad (a) \tag{1.30}$$

The thresholds used were $\Delta_1 = 0.1, \Delta_2 = 0.3$. They measured the critical

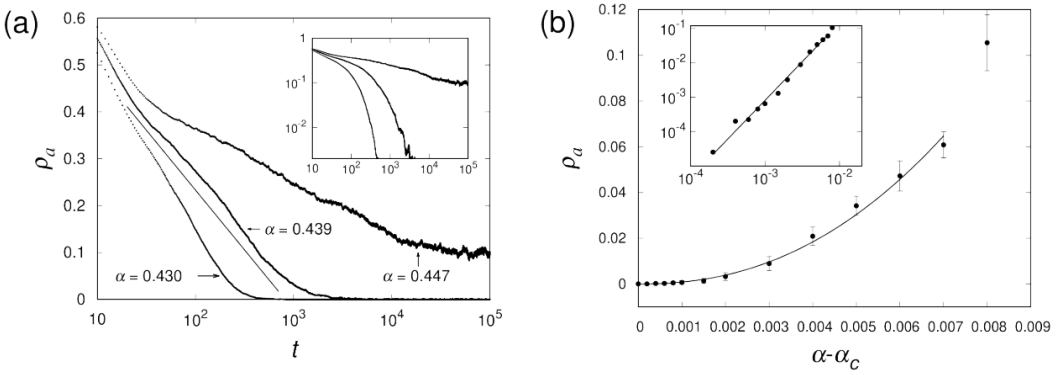

FIGURE 1.10: (a) The time evolution of the fraction of incoherent regions $\rho_a(t)$. For $\alpha \leq \alpha_c = 0.439$, $\rho_a(t)$ decays to 0 over time, while for $\alpha > \alpha_c$, it fluctuates around a certain value ρ_∞. (b) The $\alpha - \alpha_c$ dependence of the fraction of incoherent regions ρ_∞ in the steady state after a long period of time. Reused from Ref. [68] with permission of the authors.

behavior of the coherent-multichimera transition and compared it with the transition behavior of directed percolation. Fig. 1.10(a) shows the time evolution of the spatial fraction of incoherent regions $\rho_a(t)$. For $\alpha \leq \alpha_c = 0.439$, $\rho_a(t)$ decays to 0 over time, whereas for $\alpha > \alpha_c$, it fluctuates around a certain value ρ_∞. Fig. 1.10(b) shows the $\alpha - \alpha_c$ dependence for $\alpha > \alpha_c$. Near the transition point, it follows a power law,

$$\rho_\infty \sim (\alpha - \alpha_c)^{\beta_\alpha}, \quad \beta_\alpha = 2.21 \pm 0.09 \tag{1.31}$$

This value is significantly larger than the corresponding critical exponent $\beta_{DP} \approx 0.277$ for (1+1) dimensional DP. The difference can be attributed to the traveling waves, which collide and reinstate incoherent regions (see Fig. 1.10(b)).

1.2.3 Repulsive coupling

In systems with repulsive interactions, twisted states can occur, and their linear stability was analyzed by Girnyk et al. in 2012 [45]. They found that for $\alpha = \pi$, only twisted states with larger values of the winding number are stable. Furthermore, when the coupling distance is very small, two types of twisted domains with a phase difference of $\Delta = \pm 2\pi q/N$ can appear, with transition regions between them. This is referred to as the multi-twisted state (fig. 1.11). It is worth noting that, in this situation, all the oscillators have the same frequency.

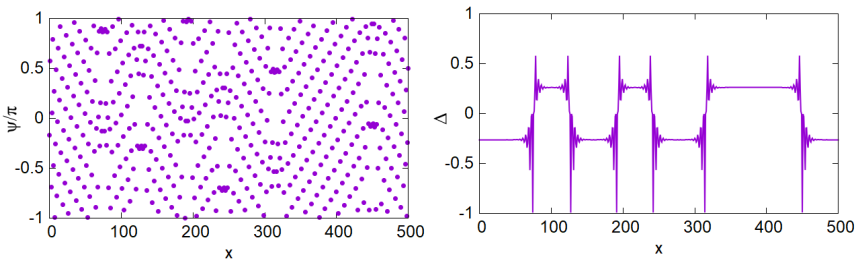

FIGURE 1.11: A snapshot of the phase ϕ (left) and phase difference Δ (right) in a multi-twisted state for repulsive coupling. $N = 500, r = 0.1, \alpha = \pi$.

For the case of $0.5\pi < \alpha < \pi$, it was studied in ref. [91]. The authors found that as α decreases from π, the frequency of some oscillators, which were originally oscillating at the same frequency, begins to drift, leading to the occurrence of multichimera states. As α continues to decrease, the number of incoherent domains in the multichimera state gradually increases. However, in this study, the authors did not focus on the case for $r \ll 1$. We found that for $r = R/N \ll 1$, the system shows very rich behavior, which will be further discussed in Chap. 2.

1.3 Mobile oscillators

Although most research so far has focused on oscillators fixed in space or oscillators on network structures, some studies have focused on an interesting special case: mobile oscillators, which move through space and whose

coupling partners can change over time due to their movement. The research on mobile agents can be traced back to the Vicsek model. In this model, self-propelled agents interact with each other and align their moving directions (phases), which has been used to study animal groups such as fish schools and bird flocks. With the development of research in the field of coupled oscillators, the case of moving agents being phase oscillators has gradually attracted attention due to its potential applications in various fields, such as chemotactic elements [151], robotics [16, 23], and wireless sensor networks [143].

In the past decade, numerous studies have emerged investigating the impact of mobility on oscillator synchronization [17, 38, 39, 47, 93, 111, 118, 121, 122, 145, 163, 165]. For example, the authors of Ref. [163] elucidates a simple case of mobile oscillators' motion and dynamics. N phase oscillators, each occupying the position of a node in a 1d lattice of size N are considered. Nodes can interact with their neighbors within a radius R, and mobility is introduced by swapping positions with one of the nearest neighbors at random times. These random times are generated by a Poisson distribution with rate λ, which is independently distributed. The system can be described by the dynamics of locally coupled oscillators in a rotating reference frame as follows:

$$\frac{\mathrm{d}\phi_i}{\mathrm{d}t} = \frac{\kappa}{n_i} \sum_{|x_{i'} - x_i| \leq R} \sin\left(\phi_i(t) - \phi_{i'}(t)\right), \tag{1.32}$$

where ϕ_i is the phase of ith oscillator, r is coupling range, n_i is the size of the interaction neighborhood, and κ is the coupling strength. The initial phases are uniformly randomly distributed within the interval $[0, 2\pi]$. The boundary conditions are non-periodic, so oscillators at the boundaries can only interact and exchange positions with neighbors on one side.

The model comprises two time scales: $1/\kappa$ accounts for the phase dynamics, and $1/\lambda$ represents the motion dynamics. Therefore, the parameter λ/κ is representative of the interplay of two time scales. For $\kappa = 1, R = 1, N = 100$, the snapshot of spatial phase profile is shown in Fig. 1.12. Due to the chosen boundary conditions, oscillators starting from a random distribution of initial phases gradually move towards phase synchronization, passing through snaky phase patterns containing multiple spatial modes with different wavelengths. For non-mobile nodes, i.e., $\lambda/\kappa = 0$, the transition to synchronization is very slow. When dealing with mobile oscillators, as the value of λ/κ increases, the patterns are dominated by longer wavelength modes. For high values of the λ/κ coefficient, the snaky patterns do not appear, and the oscillators quickly move towards complete synchronization. Intuitively,

as the value of the λ/κ parameter increases, the time that neighboring oscillators remain coupled together before exchanging positions becomes shorter. This prevents neighboring oscillators from aligning their phases before moving elsewhere; however, the chances to encounter and interact with other oscillators also increase, and overall, mobility accelerates the synchronization process, causing all phases to quickly converge to the population's average phase.

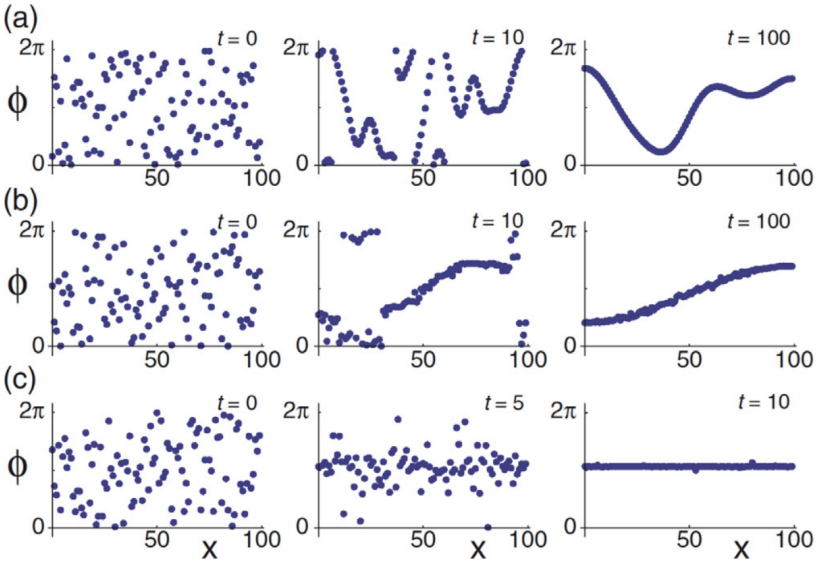

FIGURE 1.12: Snapshot of spatial phase profile. (a)$\lambda/\kappa = 0$, (b)$\lambda/\kappa = 10$, $\lambda/\kappa = 10^4$. Reprinted figure with permission from Ref. [163].

To characterize this transient dynamics, one can use the correlation function ρ between two lattice sites

$$\rho(d,t) = \langle \cos(\phi_{k+d}(t) - \phi_k(t)) \rangle_k \,. \tag{1.33}$$

It quantifies the average correlation of two phases at a distance d. If $\rho \approx 0$, then the two phases at this distance are uncorrelated; if $\rho = \pm 1$, they are correlated. The time evolution of $\rho(d,t)$ reflects the dynamics of the system as it relaxes to the synchronized state. The correlation function ρ follows an exponential function $1 - \rho = e^{-t/T_c}$, where T_c is the relaxation time. It has been shown that mobility affects the characteristic time in an intermediate range: between $\lambda/\kappa = 1$ and the onset of mean-field behavior (very high

λ/κ). In this range, T_c satisfies

$$T_c \approx \frac{N^2}{\pi^2 \kappa} \frac{1}{1+\lambda/\kappa}. \tag{1.34}$$

For very high mobility, $T_c \approx 0.5$, indicating that the oscillators behave as a mean-field system. For low mobility, T_c depends strongly on system size. By comparing the characteristic time T_c in the mobile oscillator system with that of nonmobile oscillators with a coupling range, one can obtain an effective coupling range of mobile oscillators

$$R_e = \frac{-3+\sqrt{49+48\lambda/\kappa}}{4}, \tag{1.35}$$

in the regime where the longest spatial mode keeps its sinusoidal shape, i.e., for $(\lambda/\kappa)/N^2 \ll 1$. This result demonstrated that mobility is equivalent to increasing the effective coupling distance between oscillators, thereby enhancing synchronization.

Besides, many other research contribute to this field. Ref. [118] investigated the impact of mobility on locally coupled moving phase oscillators affected by noise on a one-dimensional ring and showed that mobility can destabilize twisted solutions and enhance synchronized solutions. Ref. [121] studied systems with delay coupling and found that mobility can lead to the occurrence of chimera states. Ref. [111] considered cases where the movement and phase of oscillators can mutually influence each other and discovered various swarming and synchronization patterns. However, little is known about the combined effects of phase lag and mobility on twisted and chimera states. Recently, two studies have considered phase lag. Ref. [165] demonstrated the transition between synchronous states and chimera states with one or two coherent regions, while Ref. [145] demonstrates that positional disorder among oscillators, introduced as static (quenched) randomness or dynamic random motion (diffusive or ballistic), disrupts synchrony and promotes the stability of chimera states in a nonlocally coupled oscillator array. These papers focus on systems with the phase lag α close to 0.5π, and a study spanning a wide range of α is still lacking.

1.4 Contributions of the dissertation

The purpose of this study is to explore the effects of frustration in coupled oscillator systems and to deepen our understanding of how frustration influences complex dynamical behaviors, particularly with regard to chimera states and applications in neuroscience. This dissertation examines the following three scenarios: (1) the impact of frustration on the dynamics of oscillators with nonlocal repulsive coupling, (2) the combined effects of frustration and mobility when oscillators can move in space, and (3) the role of frustration in hierarchical network structures composed of multiple populations of oscillators. The findings indicate that frustration induces a wide variety of rich dynamical behaviors under different conditions, which have significant implications for physical, engineering, and biological systems.

The structure of this dissertation includes both a literature review and original research: Chapters 1 and 4 serve as background introductions and reviews of previous studies, while Chapters 2, 3, and 5 present the author's original contributions. Chapter 1 introduces the fundamental theories of coupled phase oscillators, synchronization, chimera states, and mobile oscillators, providing the necessary theoretical framework for the subsequent research. Chapter 2 investigates the effects of frustration in systems with nonlocal repulsive coupling. The study reveals similarities between the oscillator dynamics under this coupling and directed percolation phenomena. Chapter 3 examines the combined effects of frustration and mobility when oscillators can move in space. This study provides new insights into synchronization in mobile devices with delayed communication and neuronal networks with rewiring. Chapter 4 reviews the application of the Ott-Antonsen reduction method in analyzing complex oscillator systems and discusses the research progress of coupled oscillator systems in neuroscience. Chapter 5 explores the effects of frustration in multi-population oscillator systems, focusing on how these systems behave in hierarchical network structures and their metastable properties. This research offers a theoretical basis for understanding how different regions of the brain transition between partial synchronization and desynchronization.

Through these studies, this dissertation not only deepens the understanding of the relationship between coupled oscillator systems and frustration effects but also makes significant contributions to the practical applications of these systems in neuroscience and the study of chimera states.

Chapter 2

A ring of nonlocally coupled oscillators with a repulsive coupling

In this chapter, we explore the dynamic behaviors of a ring of nonlocally coupled oscillators under repulsive coupling, focusing on the effects of phase lag. The chapter begins with a linear stability analysis of twisted states, examining their stability range under varying system parameters. Next, we investigate the spatiotemporal patterns that emerge as the phase lag changes. We then draw parallels between these patterns and directed percolation models, particularly the Z2-symmetric directed percolation (DP2), emphasizing their similarities and differences. Finally, we discuss the critical behavior observed near the transition point and examine the resurgence of multichimera states under specific conditions.

The content of this chapter is adapted from the author's published work: B. Li and N. Uchida, Phys. Rev. E 104, 054210 (2021). DOI: 10.1103/PhysRevE.104.054210

2.1 Linear stability analysis

In this chapter, we discuss the stability of the twisted state through linear stability analysis. The linear stability for the case of $\alpha = 1$ and for any α in finite-sized systems has been investigated in previous studies [45, 100]. However, in this study, we generalize it to the continuous limit $N \to \infty$ for any α.

First, we add a small perturbation to the solution of the twisted state (1.21):

$$\phi(x,t) = \Omega t + Qx + \sum_K A_K e^{iKx+\Lambda_K t}, \quad Q = \frac{2\pi q}{N} \tag{2.1}$$

where the coefficient $A_K \ll 1$, and Λ_K is the linear growth rate for the wavenumber $K = 2\pi k/N$. The summation is taken over $k = 1, 2, \cdots, N-1$. By substituting this into eq. (1.18) and linearizing, the zeroth-order term of the perturbation is

$$\Omega = -\frac{1}{2R} \sum_{\substack{s=-R \\ s\neq 0}}^{R} \sin(-Qs + \alpha\pi), \tag{2.2}$$

and the first-order term is

$$\sum_K \Lambda_K A_K e^{iKx+\Lambda_K t} = -\frac{1}{2R} \sum_{\substack{s=-R \\ s\neq 0}}^{R} \cos(-Qs + \alpha\pi) \sum_K A_K e^{iKx+\lambda t}(1 - e^{iKs}) \tag{2.3}$$

where $s = y - x$. From eq. (2.3), taking the real part of both sides, the linear growth rate of the perturbation can be written as

$$\mathrm{Re}\Lambda_K = -\frac{1}{2R} \cos\alpha\pi \sum_{\substack{s=-R \\ s\neq 0}}^{R} \cos Qs \,(1 - \cos Ks)\,. \tag{2.4}$$

Note that the sign of $\mathrm{Re}\Lambda_K$ does not depend on α in the interval $0.5\pi < \alpha \leq \pi$. Fig. 2.1(a) shows the normalized linear growth rate $\mathrm{Re}\Lambda_K/(-\cos\alpha\pi)$ for

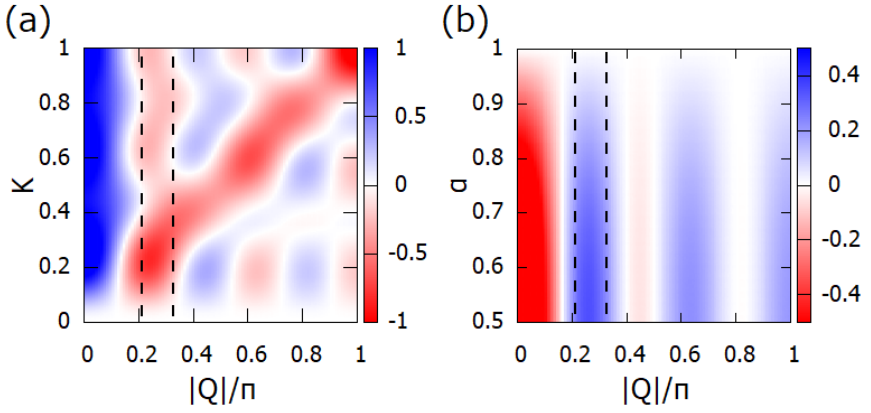

FIGURE 2.1: (a) Normalized linear growth rate $\mathrm{Re}\Lambda_K/(-\cos\alpha\pi)$. (b) Phase velocity Ω of the twisted state. The dashed lines indicate the linear stability range $0.215 < |Q|/\pi < 0.323$. Figures are reprinted from [84].

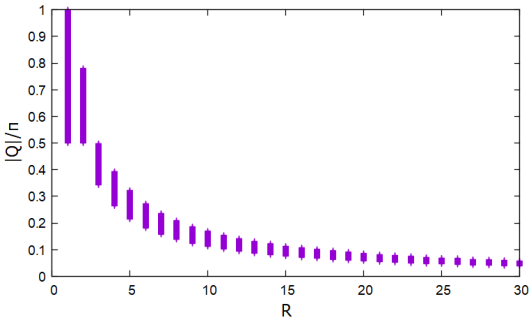

FIGURE 2.2: Linear stability range of Q for each coupling distance R.

$R = 5$. The twisted state is linearly stable when $\mathrm{Re}\Lambda_K < 0$ for all wavenumbers K. The stability range is approximately given by $0.215\pi < Q < 0.323\pi$. Fig. 2.2(b) shows the phase velocity Ω for $R = 5$. The sign of Ω changes with the value of Q, and it is always positive within the range of Q where the twisted state is linearly stable. As the phase delay α approaches 1, the absolute value of Ω converges to 0. Additionally, it can be shown that the stable range of Q becomes narrower as R increases (Fig. 2.2). This is considered to be due to the increased frustration as the number of interacting oscillators increases.

2.2 Spatiotemporal pattern

In this study, we used the Runge-Kutta method, with a coupling distance of $R = 5$ and a number of oscillators $N = 10000$. Therefore, $r = R/N = 5 \times 10^{-4} \ll 1$. We numerically integrated equation (1.18) with a time step of $\Delta t = 0.01$. The initial phases were given as uniform random numbers in the range $(-\pi : \pi]$, and periodic boundary conditions were used.

For several values of α, the spatial profiles and histograms of the phase difference between neighboring oscillators $\Delta(x,t) = (\phi(x+1,t) - \phi(x,t))/\pi$ are shown in Fig. 2.3. For $\alpha = 0.5\pi$, $\Delta(x)$ is randomly distributed (Fig. 2.3(a)(b)). As α increases, a chimera state appears where twisted and incoherent regions coexist (Fig. 2.3(c)). Two types of twisted regions with positive and negative phase differences alternately appear, with incoherent regions in between. The distribution of $\Delta(x)$ has two peaks within the linear stability range (Fig. 2.3(d)). As α increases further, the twisted regions expand, and the distribution of $\Delta(x)$ becomes sharper (Fig. 2.3(e)-(h)). Near the boundary between incoherent and twisted regions, $\Delta(x)$ oscillates and converges

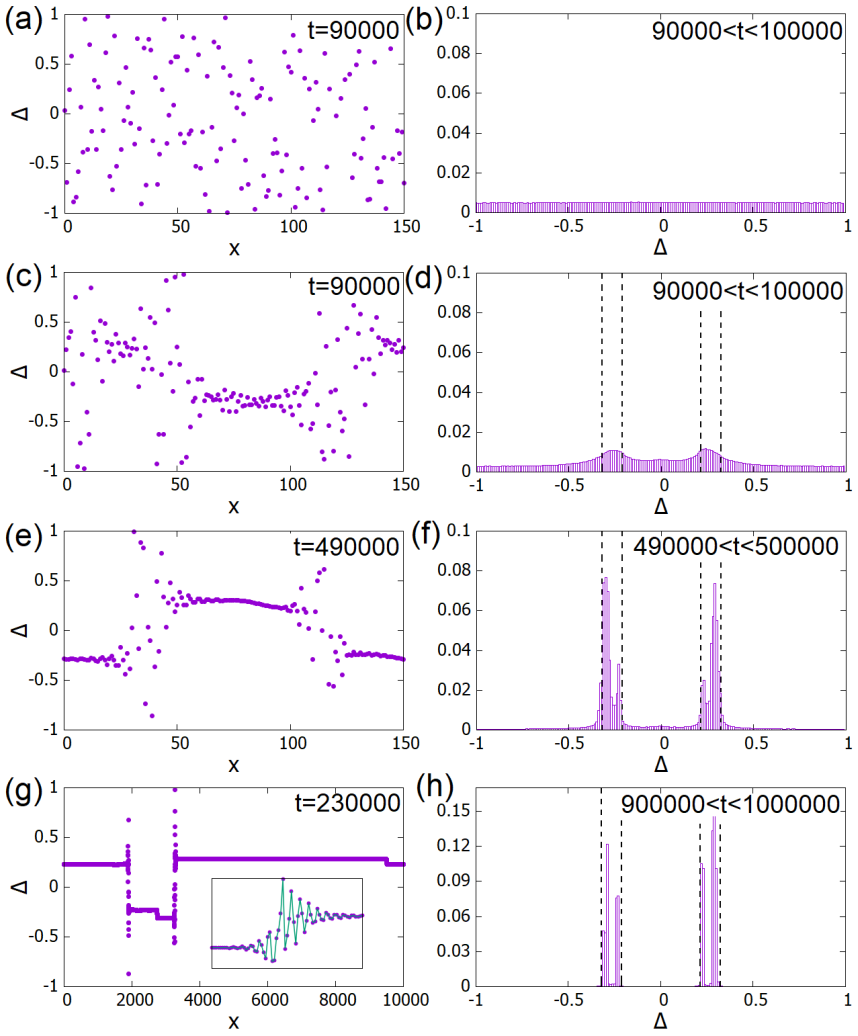

FIGURE 2.3: Spatial profiles (left) and histograms (right) of $\Delta(x)$. (a)(b) $\alpha = 0.5\pi$, (c)(d) $\alpha = 0.65\pi$, (e)(f) $\alpha = 0.70\pi$, (g)(h) $\alpha = 0.73\pi$. (a)(c)(e) show only 150 oscillators in part of the system. (g) shows the entire system. Insets are magnifications of the boundary between two twisted regions. The dashed lines in histograms (d)(f)(g) indicate the linear stability range $0.215 < |\Delta| < 0.323$. Figures are reprinted from [84].

to a stable value in the twisted region, similar to the Gibbs phenomenon in Fourier series (Fig. 2.3(h), inset).

The spatiotemporal patterns of the phase difference $\Delta(x,t)$ are shown in Fig. 2.4(a)-(l). Yellow and light blue indicate twisted regions with positive and negative phase differences, respectively, with narrow incoherent regions present. For $\alpha \leq 0.74\pi$, pair creation and annihilation of incoherent regions (separation and merging of twisted regions) are observed. For $\alpha > 0.74\pi$, various patterns, such as traveling waves and wavy patterns with constant speed, were observed. These will be analyzed and classified in the following sections.

2.3 Directed percolation with two absorbing states

The Z2-symmetric directed percolation (DP2) is an extended model from the previous DP model, with examples including the monomer-dimer model, cellular automata, and the non-equilibrium Ising model [58]. In DP2, each site can be in an active state A or one of two inactive states I_1 or I_2. The system evolves over time according to the following rules:

1. From an active region, two inactive sites I_1 and I_2 are generated with equal probability.
2. The boundary between active and inactive regions fluctuates.
3. An active site A is generated at the boundary between two different inactive regions I_1 and I_2.

Rules 1 and 2 are direct extensions of the DP rules, where active and inactive regions compete, resulting in a phase transition. Rule 3 is unique to DP2, which distinguishes between the two types of inactive regions. The transition probabilities of the extended Domany-Kinzel model are defined as follows ($i = 1, 2$):

$$P(I_i|I_i, I_i) = 1 \tag{2.5}$$
$$P(A|A, A) = 1 - 2P(I_i|A, A) = p_2 \tag{2.6}$$
$$P(A|I_i, A) = P(A|A, I_i) = p_1 \tag{2.7}$$
$$P(A|I_1, I_2) = 1 \tag{2.8}$$

Equations (2.5)–(2.7) extend equations (1.23)–(1.25), and the newly added equation (2.8) corresponds to rule 3. The spatiotemporal patterns when $p_2 =$

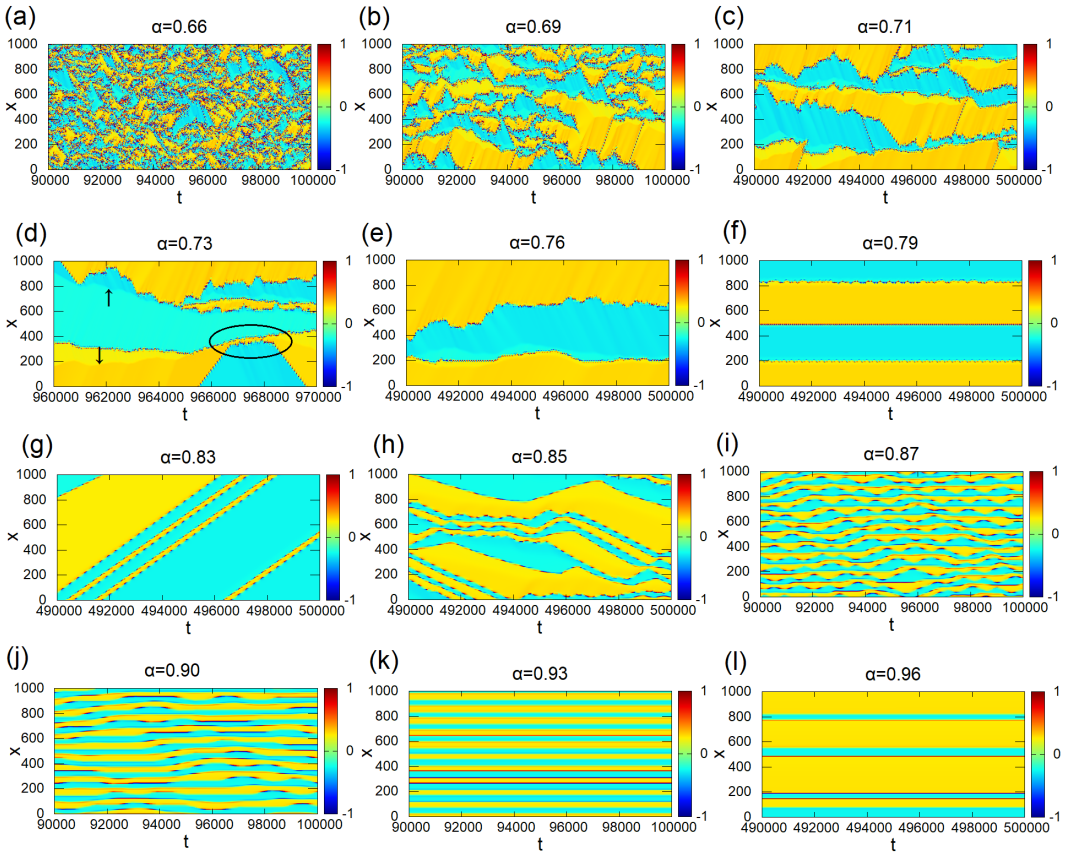

FIGURE 2.4: (a)-(k): Spatiotemporal patterns of the phase difference $\Delta(x,t)$ for various α. The figures show only 1000 oscillators in part of the system. Yellow and light blue indicate twisted regions with positive and negative phase differences, respectively, with incoherent regions at their boundaries. The arrows in (d) indicate boundaries of regions with slightly different same-sign phase differences, and the circles indicate the approach and subsequent repulsion of two incoherent regions after some time interval. Figures are reprinted from [84].

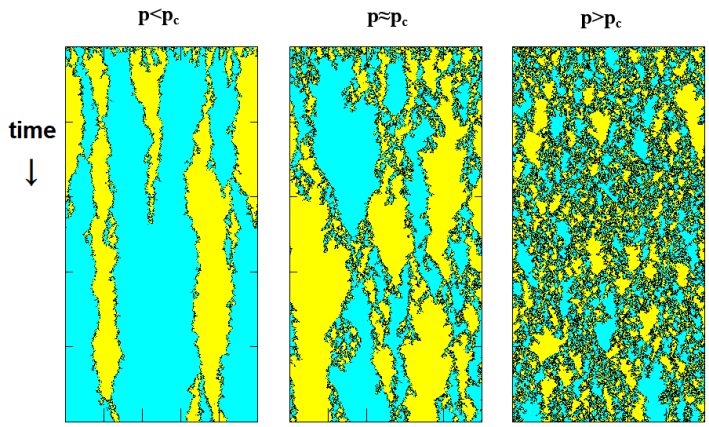

FIGURE 2.5: Spatiotemporal patterns of the Domany-Kinzel model with two types of absorbing states. Yellow and light blue represent the two types of inactive sites, and black represents the active sites at their boundaries.

$p_1 = p$ are shown in Figure 2.5. Yellow and light blue correspond to the two types of inactive regions, with a narrow active region in black at their boundaries. In the inactive phase with $p < p_c$, the system reaches an absorbing state where either I_1 or I_2 occupies all sites. A significant difference between this system and DP is that the proportion of active sites in the inactive phase, ρ, decays as a power function $\rho(t) \sim t^{-1/2}$ in DP2, compared to exponential decay in DP. Viewing the time evolution of inactive sites as the trajectory of a single particle, the change in $\rho(t)$ can be attributed to pair creation ($A \to 3A$) and pair annihilation ($2A \to \emptyset$), with the power exponent $-1/2$ interpreted as the diffusion of particles being a random walk.

The occurrence of active sites between the two absorbing states makes the system more likely to remain active compared to regular DP, expanding the parameter range of the active phase. When starting from an initial state with only one active site and all other sites inactive, the probability $P(t)$ that the active region generated from that one site remains active at time t and the mean square displacement $R^2(t)$ from the origin follow:

$$P(t) \sim t^{-\delta}, \quad R^2 \sim t^z \tag{2.9}$$

with critical exponents δ and z related to β, $\xi_\perp$, and $\xi_\parallel$ by:

$$\delta = \frac{\beta}{\nu_\parallel}, \quad z = \frac{2\nu_\perp}{\nu_\parallel} \tag{2.10}$$

Numerical simulations for one-dimensional DP2 yield critical exponents $\delta = 0.285$, $z = 1.15$, and $\beta = 0.90$ [58]. It is important to note that the symmetry between the two absorbing states is a necessary condition for the DP2 universality class. If this symmetry is broken (for example, if $P(A|I_1, A) \neq P(A|A, I_2)$ in equation 2.7), the critical exponents revert to those of regular DP.

2.4 Discretization of oscillator states

To compare the system eq. 1.18 with DP2, it is necessary to define discrete state variables. Therefore, we distinguish between twisted regions and incoherent regions using the local standard deviation of phase differences:

$$\sigma_\Delta(x,t) = \sqrt{\frac{1}{2R}\sum_{y=x-R}^{x+R-1}[\Delta(y,t) - \overline{\Delta}]^2} \tag{2.11}$$

We define a site x as being in a twisted state when $\sigma_\Delta(x) < \delta_c$, and in an incoherent state when $\sigma_\Delta(x) > \delta_c$. We chose a threshold δ_c of 0.1, approximately the width of the linear stability range.

The discrete state variable $s(x,t)$ is then represented as follows: twisted sites with positive and negative phase differences $\Delta(x)$ are denoted as $s(x,t) = 1$ and $s(x,t) = -1$, respectively, and incoherent sites are denoted as $s(x,t) = 0$. Fig. 2.6 shows an example of the spatiotemporal pattern after discretization. Notably, traveling waves can be emitted from incoherent regions at a constant speed (indicated by arrows in the figure). Additionally, the phase differences in the twisted regions on both sides of the traveling wave have the same sign, meaning they do not serve as boundaries of the twisted regions. This is a feature not seen in DP2.

2.5 Similarities to absorbing state transitions

The spatiotemporal patterns for $\alpha < 0.79\pi$ (Fig. 2.4(a)-(e)) exhibit features similar to DP2 in the following ways:

1. An incoherent region always exists between twisted regions with opposite signs, and the proportion of the system occupied by incoherent regions changes due to pair creation and annihilation.

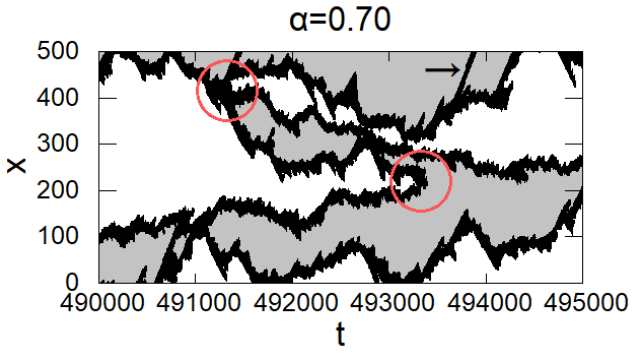

FIGURE 2.6: Spatiotemporal pattern after discretization for $\alpha = 0.70\pi$. Black: $s = 0$ (incoherent), white and gray: $s = \pm 1$ (twisted). Pair creation and annihilation of incoherent regions are indicated by red circles, and arrows indicate the emission of traveling waves. Figures are reprinted from [84].

2. As α increases, the proportion of incoherent regions decreases and disappears at a certain threshold.

At the same time, as shown in Fig. 2.4(d), there are differences such as the presence of slightly different same-sign phase differences within a single twisted region, and the approach and repulsion (rather than annihilation) of two incoherent regions.

The proportion of incoherent sites is defined as follows:

$$\rho(t) = \frac{1}{N} \sum_{x=1}^{N} [1 - s(x,t)^2] \tag{2.12}$$

The time evolution of $\rho(t)$ for $0.66\pi \leq \alpha \leq 0.78\pi$ is shown in Figure 2.7. Depending on the value of the phase delay α, $\rho(t)$ either decays to 0 or approaches a positive constant value after a sufficiently long time. For each value of α, the time and ensemble averages of $\rho(t)$ in the long-term steady state are denoted as $\rho_\infty(\alpha)$. Figure 2.8 shows the dependence of the proportion of incoherent sites $\rho_\infty(\alpha)$ in the steady state on α. As α increases, $\rho_\infty(\alpha)$ becomes 0 at $\alpha = \alpha_c = 0.722\pi$, indicating the disappearance of incoherent regions. Fitting with a power function $\rho_\infty(\alpha) \sim (\alpha_c - \alpha)^\beta$, we obtain $\beta = 0.755 \pm 0.028$ (Figure 2.8(b)). Thus, the system with $\alpha < \alpha_c = 0.722\pi$ has properties similar to the active phase of DP2, and we refer to this as "phase I". Conversely, for $\alpha_c \leq \alpha < 0.79\pi$, the number of incoherent regions becomes 0 or a small even number close to 0, since the number of incoherent

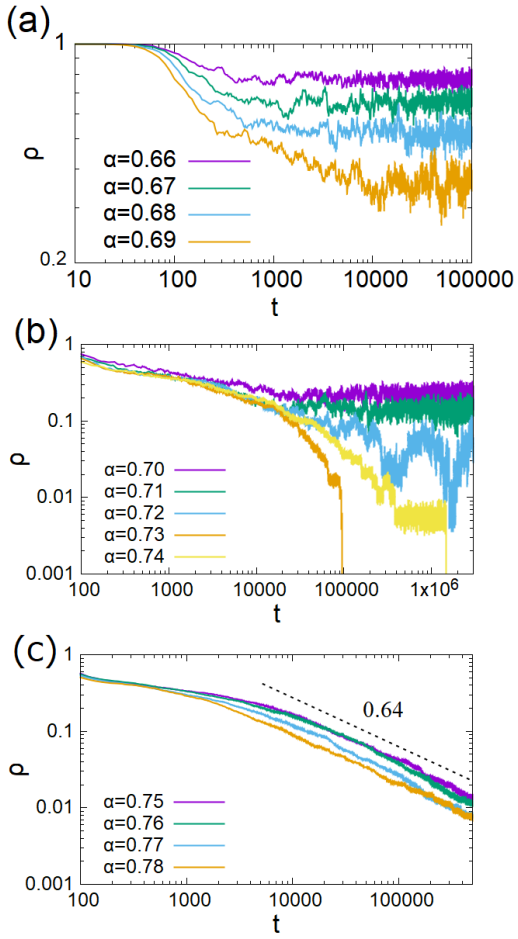

FIGURE 2.7: Time dependence of the proportion of incoherent regions $\rho(t)$. Figures are reprinted from [84].

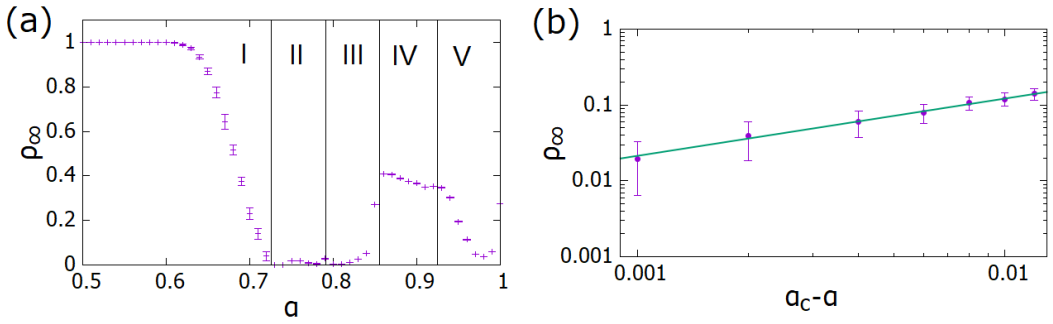

FIGURE 2.8: Dependence of the proportion of incoherent sites $\rho_\infty(\alpha)$ in the dynamic steady state on α. Figures are reprinted from [84].

regions is always an integer multiple of 2 due to pair creation and annihilation processes. When $\rho(t) = 0$, all oscillators are in a single twisted state, preventing the generation of incoherent sites, thus satisfying the definition of an "absorbing state". This corresponds to the inactive phase of DP2, which we will call "phase II". For $0.75\pi \leq \alpha \leq 0.78\pi$, six out of seven simulations with different initial conditions resulted in $\rho(t) = 0$ by $t = 5 \times 10^6$, but the decay time greatly depended on the initial conditions. In the range $0.75\pi \leq \alpha \leq 0.78\pi$, ensemble averages of $\rho(t)$ were fitted with a power function $\rho(t) \sim t^{-\delta}$ from 40 simulations with different initial conditions and $t < 5 \times 10^5$, yielding $\delta = 0.64 \pm 0.04$. Notably, to determine the exponents β and ρ with an accuracy of 0.1, a system size of $N = 10^4$ or larger is required. Each incoherent region has a width of about $5R$, and the change in $\rho(t)$ due to pair creation and annihilation is discrete, changing in steps of $\Delta\rho \sim 10R/N$ (where $R \ll N$). For small systems with $N \leq 10^3$, it is not possible to fit $\rho(t)$ and $\rho_\infty(\alpha)$ with smooth functions. In contrast, for $0.75\pi \leq \alpha \leq 0.78\pi$, all incoherent regions in systems with $N = 10^3$ disappeared within the simulation time, while incoherent regions remained in systems with $N = 10^4$ even after $t = 5 \times 10^6$. The larger the system, the longer it takes for the last few incoherent regions to collide and annihilate, suggesting that the mean lifetime of incoherent regions scales with $N^{1/\delta}$, although the large dispersion prevents quantitative determination of the N dependence of the mean lifetime of incoherent regions.

The transition from phase I to phase II is also evident from the behavior of the phase velocity $\dot{\phi}$. Fig. 2.9 shows the average phase velocity $\bar{\omega}$ and its standard deviation σ_ω of all oscillators at the end of the simulation time. $\bar{\omega}$ peaks around α_c and σ_ω decays to 0. For $\alpha > 0.74\pi$, both $\bar{\omega}$ and σ_ω increase to non-zero values similar to $\rho_\infty(t)$ and return to 0 at $\alpha = 0.93\pi$.

Next, we define the characteristic length scale $\xi_\perp$ in the spatial direction as the average spatial interval between adjacent twisted regions. By measuring the distribution of spatial intervals of twisted regions in the time interval $90000 < t < 100000$, we calculate the mean. In the range $0.64\pi \leq \alpha \leq 0.69\pi$, the number of twisted regions with large widths decreases exponentially (Figure 2.10(a)). Meanwhile, the mean follows a power law (Figure 2.10(b)):

$$\xi_\perp \sim |\alpha - \alpha_c|^{-\nu_\perp} \tag{2.13}$$

Fitting within $|\alpha - \alpha_c| < 0.1$ yields $\nu_\perp = 1.68 \pm 0.05$, compared to $\nu_{\perp DP} \approx 1.82$ for DP2. This analysis highlights the similarities and differences between the transition dynamics in our system and those observed in DP2, providing deeper insight into the behavior of incoherent and twisted regions as α varies.

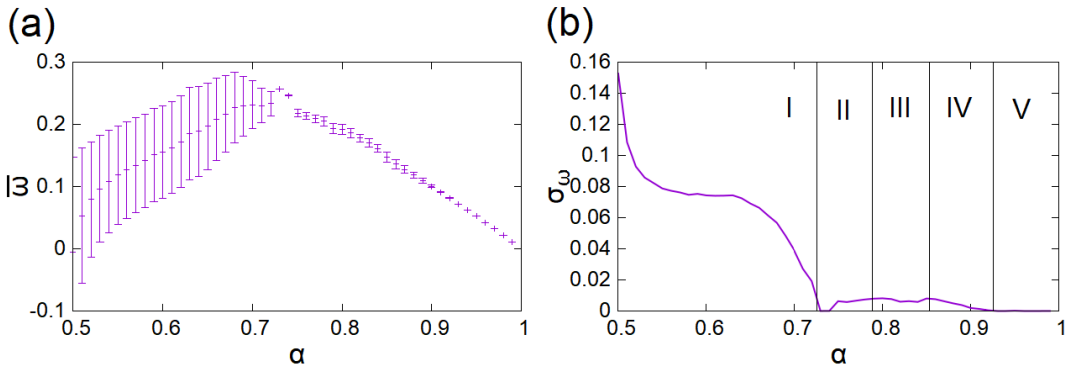

FIGURE 2.9: Dependence of the average phase velocity $\bar{\omega}$ and its standard deviation σ_ω of oscillators on α. Figures are reprinted from [84].

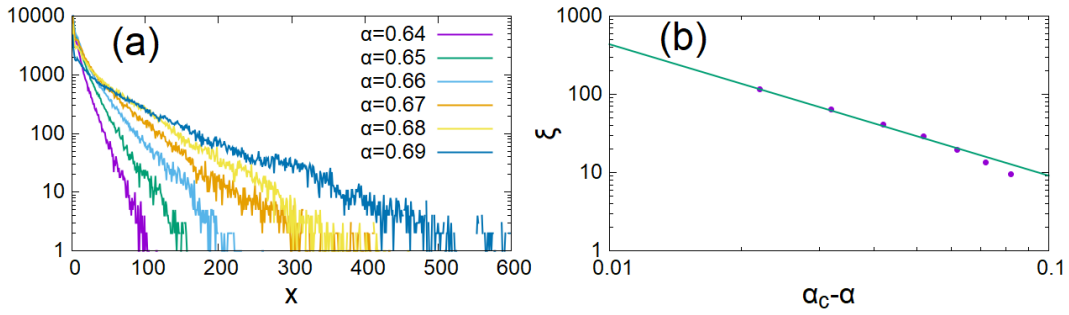

FIGURE 2.10: (a) Distribution of spatial intervals of twisted regions. (b) Dependence of the mean spatial interval on α.

2.6 Resurgence of the multichimera states

For $\alpha \geq 0.79\pi$, the spatiotemporal patterns of phase differences between oscillators change significantly compared to those for $\alpha < 0.79\pi$ (Fig. 2.4(f)-(l)). These patterns were statistically analyzed using the spatiotemporal correlation function of the state variable defined by

$$G(x,t) = \langle [1 - s(x',t')^2][1 - s(x'+x,t'+t)^2] \rangle_{s(x',t')=0}. \tag{2.14}$$

This function represents the probability that $s(x'+x,t'+t) = 0$ given that $s(x',t') = 0$. The spatiotemporal correlation functions calculated in the interval $90000 < t' < 100000$ are shown in Figure 2.11. Based on the characteristics of $\rho_\infty(\alpha)$, σ_ω, and $G(x,t)$, we classified the system into "Phase III" through "Phase V". The spatiotemporal patterns of the phase velocity $\dot{\psi}(x,t)$ in each phase are shown in Fig. 2.11. In Phases I and II, incoherent regions diffuse from their original positions (Fig. 2.11(a), 2.12(a)), whereas for $\alpha = 0.79\pi$, incoherent regions do not move, and the correlation function shows a linear spatiotemporal pattern (Fig. 2.11(b)). In the range $0.80\pi \leq \alpha < 0.85\pi$ (phase III), incoherent regions begin to travel at a constant speed (Fig. 2.11(c), 2.12(b)), and the proportion of incoherent regions ρ_∞ in the steady state increases to around 0.4 with increasing α. In the range $0.85\pi \leq \alpha < 0.93\pi$ (phase IV), the phase difference $\Delta(x,t)$ exhibits a distinctive pattern of alternating straight and zigzag stripes (Fig. 2.12(c)). Moreover, the direction of travel of the incoherent regions is related to the phase velocity of the surrounding oscillators. On both sides of zigzagging incoherent regions, the phase velocities differ, with the phase velocity always being lower on the side of the direction of travel. On the other hand, the phase velocities are the same on both sides of non-traveling incoherent regions, resulting in a mesh-like spatiotemporal pattern of $\dot{\phi}(x,t)$ (Figure 2.12(d)). For $\alpha = 0.91\pi, 0.92\pi$, the zigzag stripes start to disappear, indicating a transition to the next phase. As shown in Figure 2.9(b), in phase IV, the standard deviation of the phase velocity decreases with increasing α, becoming zero at $\alpha = 0.93\pi$. In the range $0.93\pi \leq \alpha < \pi$, all incoherent regions become straight (Fig.2.12(e)), and the entire system, including twisted and incoherent regions, attains the same phase velocity (Fig.1.11(f)). With increasing α, the proportion of incoherent regions decreases again, and each incoherent region becomes unevenly spaced (Figures 2.11(e)(f)).

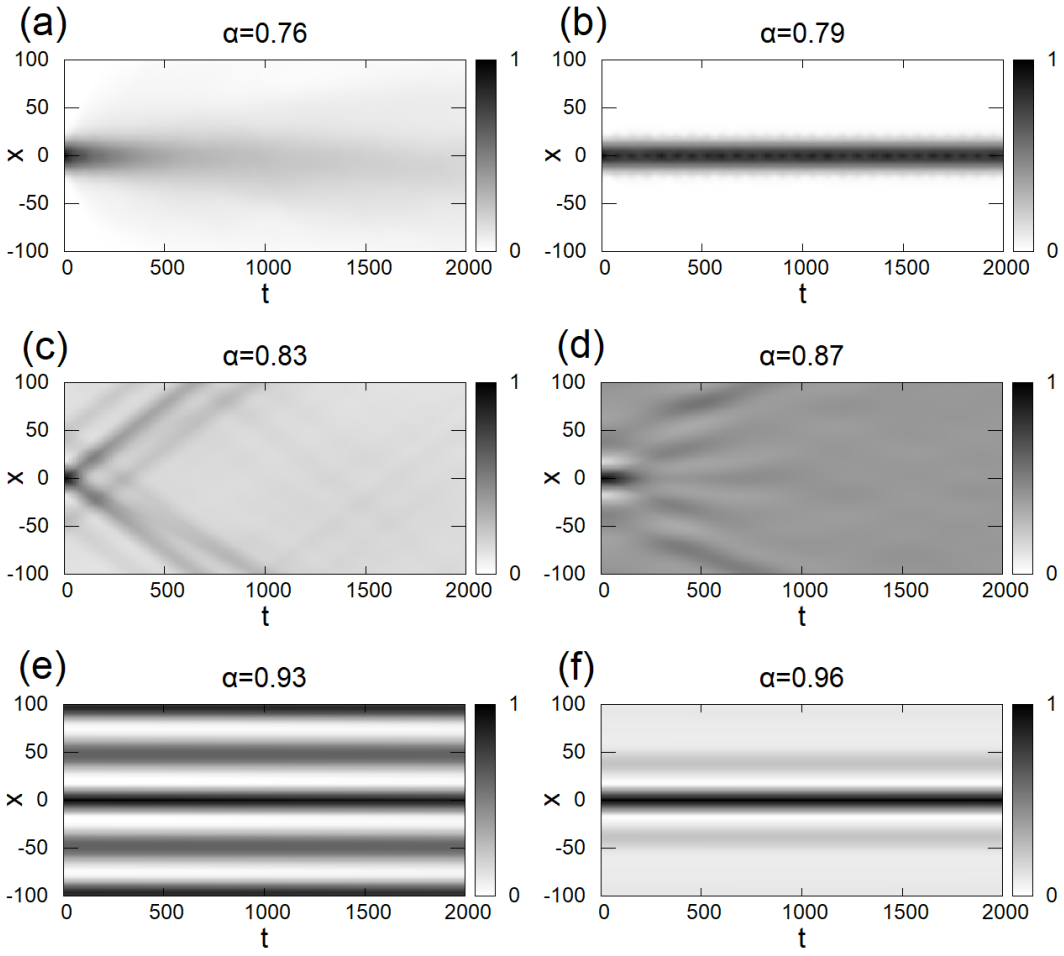

FIGURE 2.11: Spatiotemporal correlation function $G(x,t)$ of incoherent sites, with the grayscale representing the strength of the correlation. Figures are reprinted from [84].

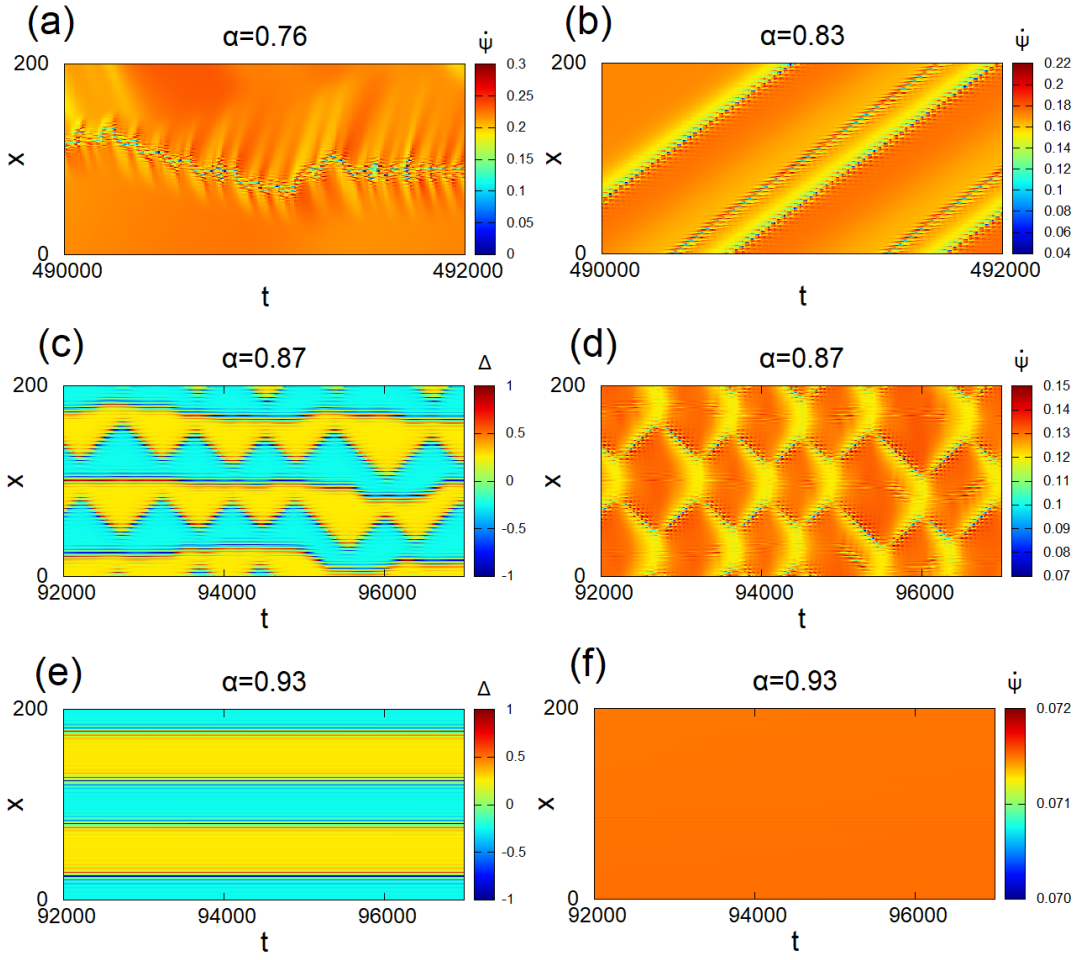

FIGURE 2.12: Spatiotemporal patterns of phase velocity $\dot{\psi}(x,t)$: (a) $\alpha = 0.78\pi$, (b) $\alpha = 0.83\pi$, (d) $\alpha = 0.87\pi$, (f) $\alpha = 0.93\pi$. Spatiotemporal patterns of phase difference $\Delta(x,t)$: (c) $\alpha = 0.87\pi$, (e) $\alpha = 0.93\pi$. Figures are reprinted from [84].

2.7 Conclusion and discussion

In this study, we investigated the statistical properties of a one-dimensional nonlocal coupled oscillator system with repulsive interactions and classified its spatiotemporal patterns into five phases based on the value of the phase delay α. The transition from phase I to phase II qualitatively resembles DP2 in two aspects: (i) Pair creation and annihilation of incoherent sites. (ii) The proportion of incoherent sites ρ_∞ becomes zero at the critical point $\alpha = \alpha_c = 0.722\pi$ (absorbing state transition).

Simulations with large system sizes allowed us to compare the critical behavior near the transition point with DP2. The critical exponent $\beta = 0.755 \pm 0.028$ characterizing ρ_∞ at the critical point and the spatial correlation length exponent $\xi_\perp = 1.68 \pm 0.05$ for our oscillator system differ from the corresponding critical exponents for DP2 ($\beta_{DP} \approx 0.90$, $\xi_{\perp DP} \approx 1.82$). Additionally, the decay exponent $\delta = 0.64 \pm 0.04$ describing the decay of $\rho(t)$ is larger than the DP2 value of $\delta_{DP} = 0.5$. This suggests that the trajectories of incoherent regions in our system exhibit faster motion compared to the random walk observed in DP2. These results indicate that although the transition from phase I to phase II shows spatiotemporal patterns similar to DP2, it does not belong to the same universality class.

The differences from DP2 can be attributed to the traveling waves emitted from incoherent regions for $\alpha < \alpha_c$ (Fig. 2.4(b)(c)(l)) and the occasional straight-line motion of incoherent regions for $\alpha_c < 0.75$ (Fig. 2.4(d)). This straight-line motion accelerates the pair annihilation of incoherent regions and the decay of $\rho(t)$ compared to random walk motion. Although no traveling waves or straight-line motion of incoherent regions were observed for $0.75\pi \leq \alpha < 0.79\pi$, the decay exponent $\delta > 0.5$ indicates the presence of long-range correlations.

Another difference is that while each site in DP2 can only take three discrete states, the phase difference $\Delta = 2\pi q/N$ in the twisted state of our system can take any integer value within the allowable range. As a result, subregions with two different phase differences Δ can form within a single twisted region. Such boundaries of slightly different Δ can be seen at $x \approx 2800, 9500$ in Fig. 2.3(g) and the arrows in Fig. 2.4(d). These boundaries repel the two approaching incoherent regions, preventing their pair annihilation (see circles in Fig. 2.4(d)).

For $\alpha > 0.79\pi$, we found that the proportion of incoherent sites ρ_∞ in the steady state exhibits a non-monotonic change as a function of α, leading to the classification into phases III to V. This non-monotonic change and the

formation of zigzag spatiotemporal patterns in phase IV are intriguing, and explaining the underlying mechanisms remains a future challenge.

Chapter 3

Effect of mobility on nonlocally coupled oscillators

This chapter investigates the influence of mobility on the dynamics of nonlocally coupled oscillators. We begin by introducing the model where oscillators are allowed to move in space, altering their coupling partners over time. Next, we present an analysis of the spatiotemporal patterns observed in the system, focusing on the transitions between coherent and incoherent states. Following this, we investigate how mobility affects the coherent state.

The content of this chapter is adapted from the author's published work: B. Li and N. Uchida, Phys. Rev. E 106, 054210 (2022). DOI: 10.1103/PhysRevE.106.054210

3.1 Model

Mobile oscillators differ from traditional fixed oscillatory systems by their spatial dynamics. These oscillators can move along trajectories defined by the underlying equations of motion, often leading to complex and rich behaviors. The interaction between mobility and nonlinearity results in phenomena such as synchronization, pattern formation, and wave propagation, which are pivotal to the understanding of various natural and engineered systems.

In this chapter, we investigate the combined effects of phase lag and mobility on the collective phase dynamics of non-locally coupled oscillators on a one-dimensional ring. We consider N oscillators on a ring with N sites. Each site on the ring is occupied by only one oscillator at a given time. This model is based on the equations for non-mobile oscillators: eq. (1.18)(1.19).

We extend this model by allowing the oscillators to move randomly by swapping positions with their nearest neighbors at a constant rate. This is implemented through a set of discrete dynamic rules with a small time step

δt. Specifically, at each time step, we let each oscillator swap positions with its right neighbor with a probability p (see fig.1), resulting in phase changes

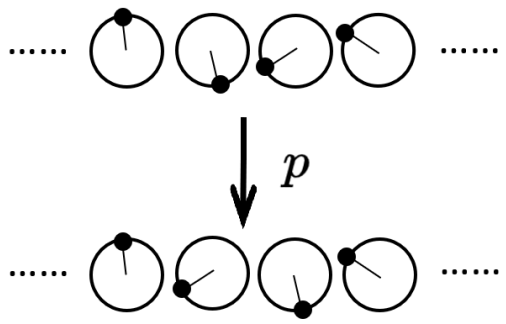

FIGURE 3.1: At each time step, two neighboring oscillators exchange their phases with probability p.

of

$$\phi(x, t+\delta t) = \phi(x+1, t), \tag{3.1}$$
$$\phi(x+1, t+\delta t) = \phi(x, t). \tag{3.2}$$

Since each oscillator's average number of moves per unit time is $2p/\delta t$, the mean square displacement (MSD) is given by

$$\langle (\Delta x)^2 \rangle \equiv \langle \left[x(t'+t) - x(t') \right]^2 \rangle = \frac{2p}{\delta t} t, \tag{3.3}$$

Its diffusion coefficient is $D = p/\delta t$. Therefore, this model can be characterized by three parameters: R, α and p.

We use the Runge-Kutta method to numerically solve eq. (1.18), with a time step of 0.01. Unless otherwise stated, we set $R = 5$ and $N = 500$. The initial conditions for the phases are random values uniformly distributed between 0 and 2π. Mobility is implemented by randomly selecting a position x and swapping the phases of oscillators at positions x and $x+1$ with a probability p. This process is repeated N times within each time interval δt, with δt also set to 0.01. Note that the upper limit for the probability $p\delta t$ is 1, hence $p \leq 100$. We checked smaller values of δt and confirmed that they do not significantly alter the results presented in the next section.

3.2 Spatiotemporal patterns and the strength of incoherence

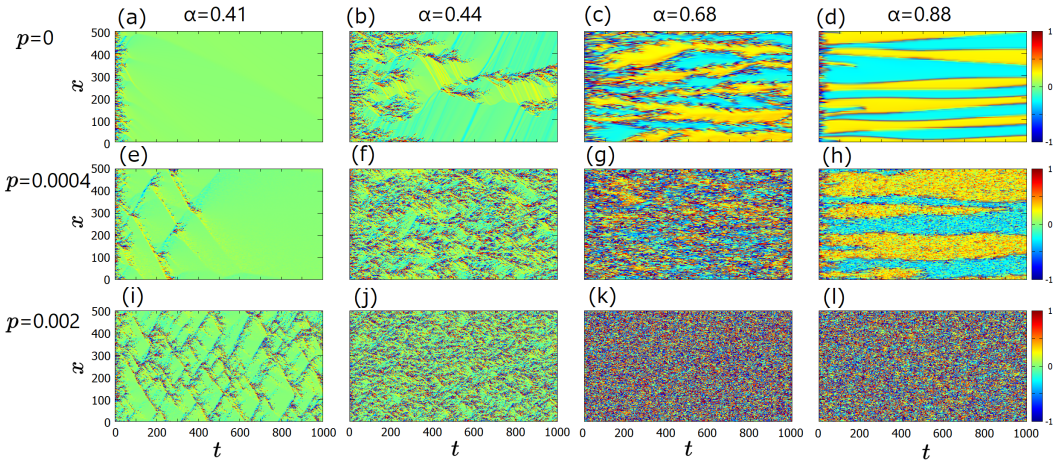

FIGURE 3.2: Spatiotemporal patterns of the phase difference $\Delta(x,t)$, for $\alpha = 0.41\pi, 0.44\pi, 0.68\pi, 0.88\pi$ from the left to the right column, and $p = 0, 0.0004, 0.002$ from the top to the bottom row. Figures are reprinted from [83].

In Fig. 3.2, we plot the spatiotemporal patterns of the phase difference between two neighboring oscillators, $\Delta(x,t) = (\phi(x+1,t) - \phi(x,t))/\pi$, truncated to the range $[-1:1)$. The first row shows the patterns for $p = 0$ with α with varying α. We vary α in the range $0 \leq \alpha < \pi$ and present a few sample cases. For $\alpha < 0.44\pi$, the system reaches a coherent state, and the Δ values are uniform and very small (Fig. 3.2(a)). For $0.44\pi \leq \alpha < 0.5\pi$, incoherent regions continuously branch and disappear, forming multi-chimera states [30, 68] (Fig. 3.2(b)). For repulsive coupling ($\alpha > 0.5\pi$), twisted states of positive and negative Δ values are separated by incoherent stripes with a width proportional to R; when α is just above 0.5π, randomly branching multi-chimera states appear (Fig. 3.2(c)), which transition into coexistence of twisted states with smooth boundaries as α increases (Fig. 3.2(d)) [84].

The mobility of the oscillators introduces novel spatiotemporal patterns. The second and third rows of Fig. 3.2 show the patterns for $p = 0.0004$ and 0.002, respectively. For $0.38\pi \leq \alpha < 0.44\pi$, we observe mesh-like patterns composed of intersecting traveling waves (Fig. 3.2(e)(i)). For the chimera state at $\alpha = 0.44\pi$, mobility introduces finer structures in the incoherent regions (Fig. 3.2(f)(j)). For $\alpha > 0.5\pi$, noise spots are added to the multi-chimera

states (Fig. 3.2(g)(h)). At $p = 0.002$, the patterns become further randomized, and the original patterns at $p = 0$ are no longer recognizable (Fig. 3.2(k)(l)).

As a measure of incoherence intensity, we follow previous studies [49] and use the standard deviation of the phase differences within a distance R from position x,

$$\sigma_\Delta(x,t) = \sqrt{\frac{3}{2R}\sum_{x'=x-R}^{x+R-1}(\Delta(x,t)-\overline{\Delta}(x,t))^2}, \tag{3.4}$$

where $\overline{\Delta}(x,t)$ is the mean phase difference over the interval $[x-R, x+R]$, and the prefactor is chosen so that the maximum value of $\sigma_\Delta(x,t)$ is 1. The incoherence intensity for the entire system is represented as $\overline{\sigma_\Delta}(t) = \langle \sigma_\Delta(x,t)\rangle_x$. Fig. 3.3 shows the values of $\overline{\sigma_\Delta}(t)$ at $t = 1000$, averaged over 10 independent samples for each set of (α, p). The full range of mobility ($0 \le p \le 1$) is shown in Fig. 3.3(a), while a zoomed-in view of the range $0 \le p \le 0.005$ is shown in Fig. 3.3(b). We obtained coherent states ($\overline{\sigma_\Delta} \ll 1$) for small α values, regardless of the value of p. Coherence sharply increases at $\alpha = \alpha_c \simeq 0.4\pi$, with the threshold α_c having little dependence on p. On the other hand, for $\alpha > 0.5\pi$, the system falls into a fully incoherent state ($\overline{\sigma_\Delta} \sim 1$) for most parameter ranges except for very small p. These changes introduced by mobility will be further discussed in the following sections.

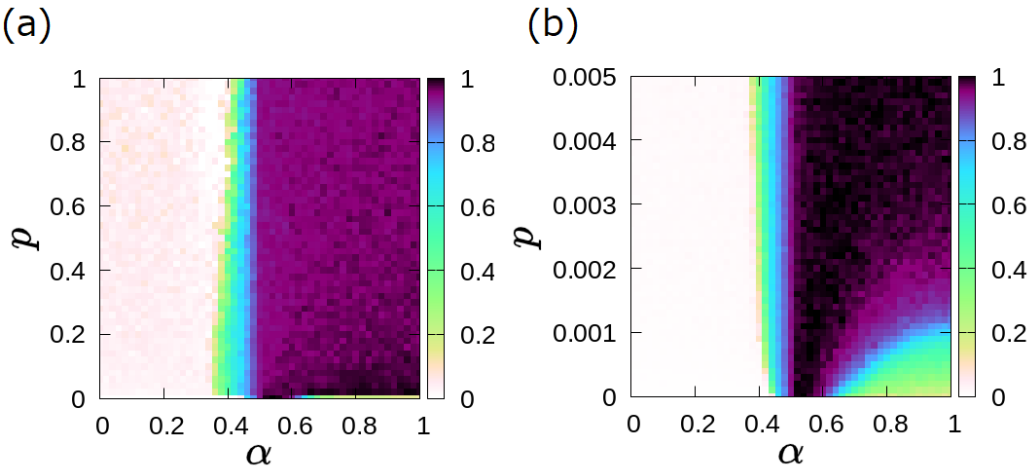

FIGURE 3.3: The strength of incoherence $\overline{\sigma_\Delta}$ on the (α, p) plane, for (a) $0 \le p < 1$ and (b) $0 \le p < 0.005$. The color scale shows a coherent state ($\overline{\sigma_\Delta} \ll 1$) in light colors, and an incoherent state ($\overline{\sigma_\Delta} \sim 1$) in dark colors. Figures are reprinted from [83].

3.2.1 The effect of mobility on the coherent states

We first focus on the effect of mobility on the coherent state for $\alpha < \alpha_c(p)$. In this parameter range, the system is multistable, meaning it can reach a synchronized state or a twisted state depending on the initial conditions. The phase difference in these states can be written as $\Delta = 2q/N$, where $q = 0$ represents the synchronized state, and non-zero integers $|q| \leq \frac{N-1}{2}$ correspond to twisted states.

In our simulations, we calculate the winding number q as

$$q = \frac{1}{2}\sum_{x=1}^{N} \Delta(x,t) \tag{3.5}$$

where $t = 1000$. Unless otherwise stated, we average over 100 samples for each (α, p) value, including the incoherent states where $\Delta(x,t)$ is spatially non-uniform. We also measure the root mean square (RMS) of q, denoted as σ_q. Fig. 3.4 shows the histograms of q for specific (α, p) values. For $p = 0$, the distribution is wide, with the maximum $|q|$ reaching 6. As p increases, the distribution narrows, indicating that mobility increases the size of the attraction basin for smaller $|q|$ values. For $p = 1$, the peak at $\alpha = 0.3\pi$ is higher than the peak at $\alpha = 0$. This implies that phase lag enlarges the attraction basin for the synchronized state.

Fig. 3.5(a) shows the root mean square (RMS) of the winding number on the (α, p) plane. Here, we focus on the coherent (synchronized or twisted) states for $\alpha < \alpha_c(p)$. Within the coherent region on (α, p) plane, the RMS decreases as α and p increase. Notably, for large p and values of α close to $\alpha_c(p)$, the RMS is nearly zero (Fig. 3.5(c)), indicating that for most samples, the synchronized state $q = 0$ is achieved.

In Fig. 3.5(b), we plot σ_q for $\alpha = 0$ as a function of the mobility parameter p. In the range $0.1 \leq p \leq 1$, the data fits a power law $\sigma_q \sim p^{-\beta}$ with an exponent $\beta = 0.239 \pm 0.005$.

The reason why mobility enhances synchrony can be explained by the disturbance of the twisted states. In a twisted state, swapping two oscillators changes the phase differences at three consecutive positions from $\{\Delta, \Delta, \Delta\}$ to $\{2\Delta, -\Delta, 2\Delta\}$. The total change in phase difference is 4Δ, which is larger for higher $|q|$ values since $\Delta = 2q/N$. In contrast, twisted states with smaller $|q|$ are less affected, and the fully synchronized state remains unaffected by the swap. If the perturbation caused by mobility outweighs the effect of interactions that restore the initial (twisted) state, the system will exit its attraction basin and transition to another, as previously demonstrated for

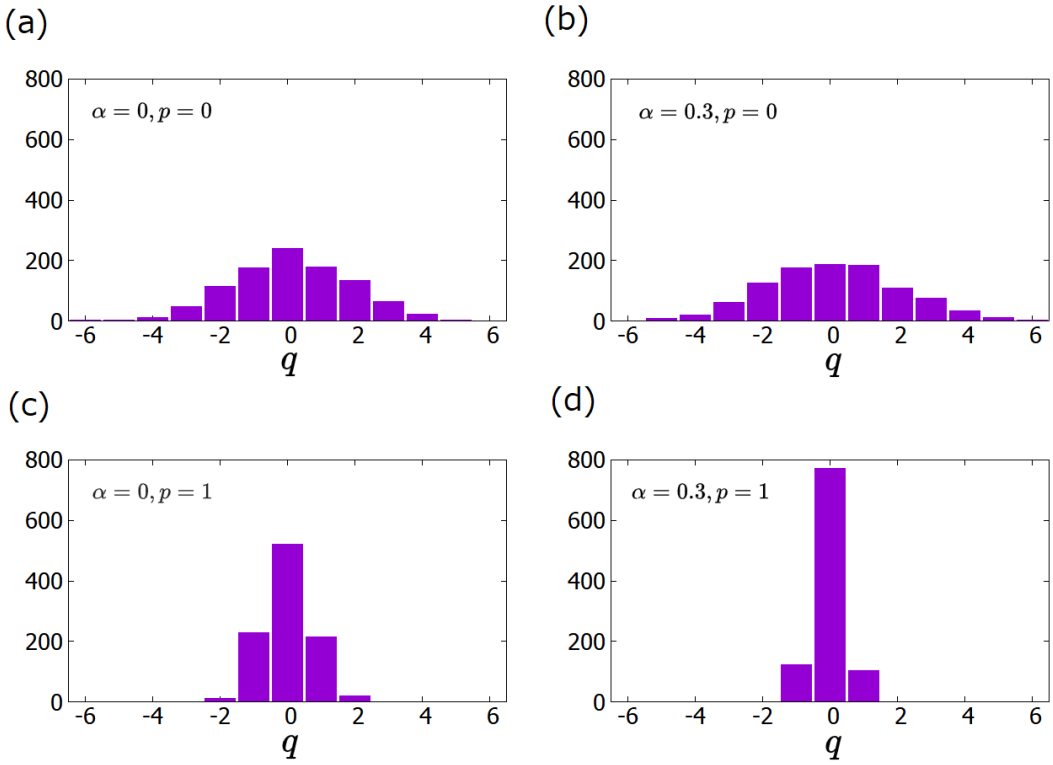

FIGURE 3.4: Histograms of the winding number q for 1000 independent samples. (a) $(\alpha, p) = (0, 0)$, which gives $\sigma_q = 1.79$, (b) $(\alpha, p) = (0.3\pi, 0)$, $\sigma_q = 2.02$. (c) $(\alpha, p) = (0, 1)$, $\sigma_q = 0.76$. (d) $(\alpha, p) = (0.3\pi, 1)$, $\sigma_q = 0.48$. Figures are reprinted from [83].

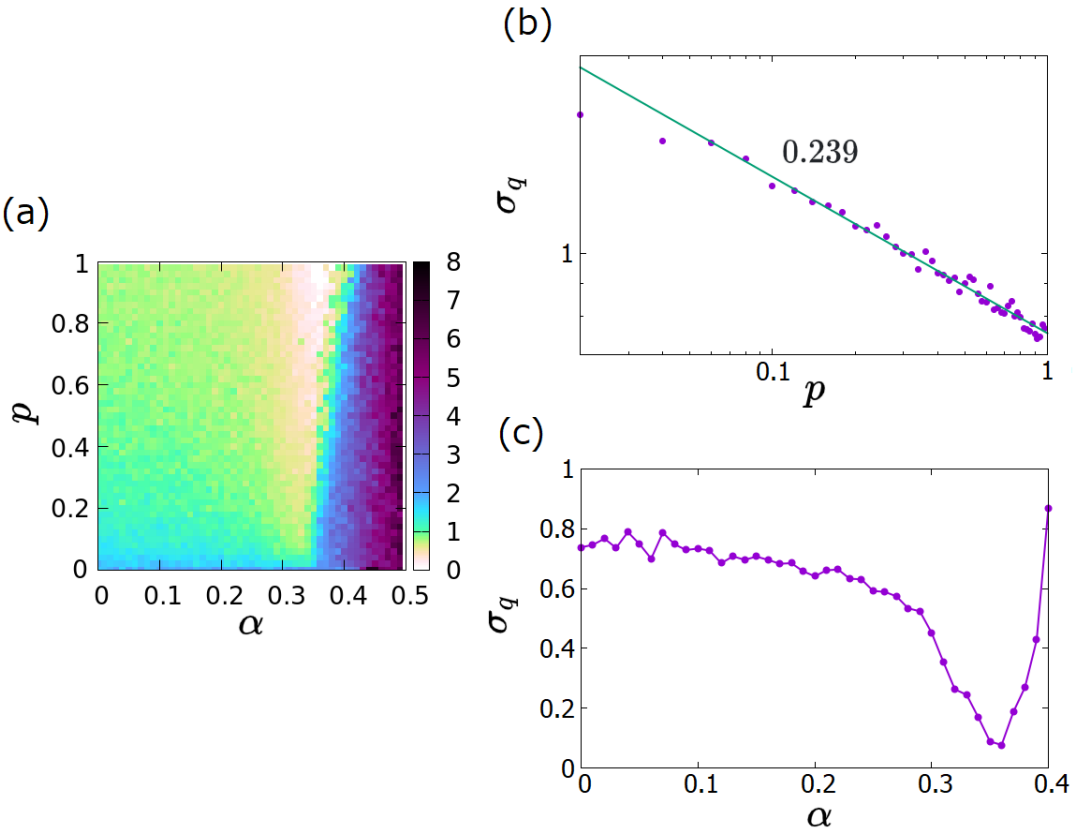

FIGURE 3.5: (a) The RMS of the winding number σ_q for each (α, p). (b) The RMS σ_q versus p for $\alpha = 0$. (c) The RMS σ_q versus α for $p = 1$. The data in (b)(c) are averages over 1000 independent samples. Figures are reprinted from [83].

$\alpha = 0$ [169]. Below, we quantitatively analyze the balance between mobility and coupling by calculating the timescales for perturbation and the restoration of the twisted states.

A system in a twisted state is divided into $|q|$ blocks of size $N/|q|$. In each block, the phase changes by 2π. Without coupling, the time required to randomize the phase difference should be proportional to the time needed for each oscillator to traverse the distance $N/|q|$ (the block size). By substituting $N/|q|$ into the left side of equation (3.3), the characteristic time for randomization is written as:

$$\tau_{\text{rand}} \sim \frac{N^2 \delta t}{2pq^2}. \tag{3.6}$$

This can be verified by calculating the spatial correlation of the phase difference:

$$G_\Delta(x,t) = \left\langle \cos\left[\Delta(x'+x,t)\pi - \Delta(x',t)\pi\right]\right\rangle_{x'} \tag{3.7}$$

for a system with mobility p but without phase coupling. Here the average is taken over x' and 100 independent samples. Note that the function has the maximal value of 1 when the phase difference is spatially uniform and that it vanishes if the phase difference is spatially random. We choose the q-twisted state as the initial condition. In this case, the function has little dependence on x because the phase difference is uniform in the initial state, and the randomization takes place uniformly. Below, we use data for $x = N/2$, denoted as $G_\Delta(t)$. Starting from a twisted state, $G_\Delta(t)$ decays exponentially over a wide range of p and q values, as shown in Fig. 3.6(a)(b).

By fitting $G_\Delta(t)$ with an exponential function, we obtain

$$G_\Delta(t) = \exp\left(-\frac{2pq^2}{a^2 N^2 \delta t} t\right) \tag{3.8}$$

with the coefficient $a \approx 0.11$. We now redefine the randomization timescale τ_{rand} as the time when $G_\Delta(\tau_{\text{rand}}) = 0.1$, yielding

$$\tau_{\text{rand}} \approx 1.4 \times 10^{-4} \times \frac{N^2}{pq^2}. \tag{3.9}$$

On the other hand, the coupling between oscillators tends to restore the twisted state. We turned off mobility and calculated the strength of incoherence $\overline{\sigma_\Delta}$ as a function of time starting from a random state; see Fig. 3.6(c) for the attractive coupling case ($0 \le \alpha \le 0.4\pi$) and Fig. 3.6(d) for the repulsive coupling case ($0.8\pi \le \alpha \le \pi$). In the attractive case, the decay of $\overline{\sigma}_\Delta$ is

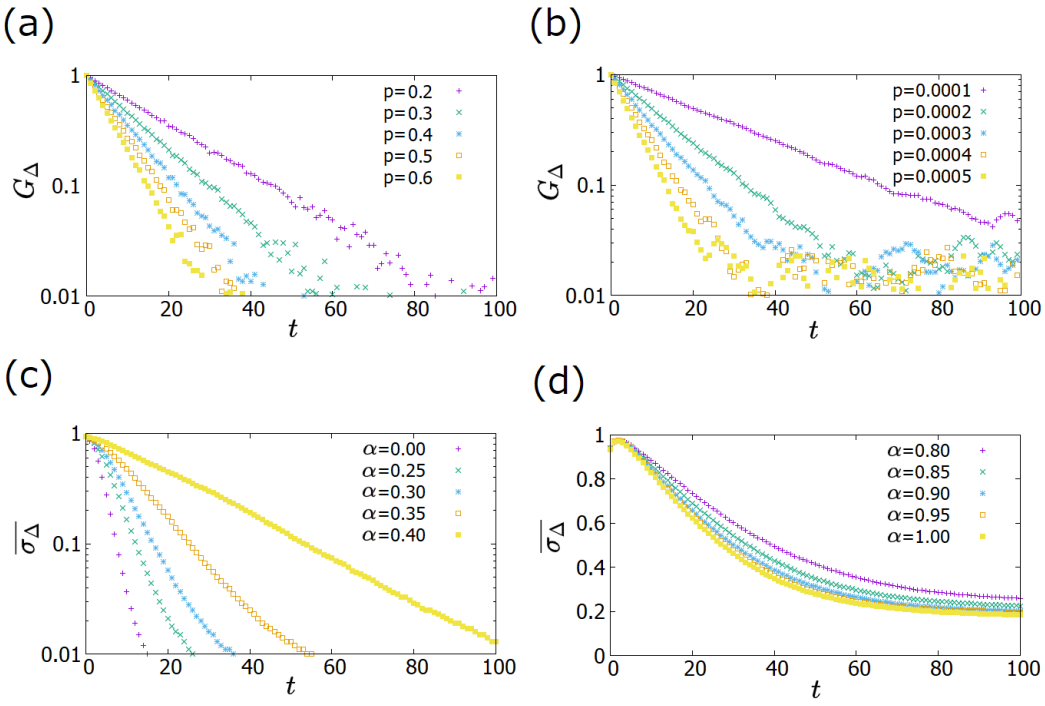

FIGURE 3.6: (a)(b) Temporal correlation of the phase difference $G_\Delta(N/2, t)$, obtained without coupling and starting from the twisted state with (a) $q = 2$ and (b) $q = 67$. It shows the effect of mobility in randomizing the phase difference. (c)(d) The strength of incoherence $\overline{\sigma_\Delta}$ obtained without mobility and starting from the random state, for (c) $0 \leq \alpha \leq 0.4\pi$ and (d) $0.8 \leq \alpha \leq \pi$. It shows the effect of coupling to restore the twisted states. Figures are reprinted from [83].

slower for larger α, which is explained by the frustration introduced by the phase lag. We define the timescale for restoring coherence τ_{coh} as the time it takes for $\overline{\sigma_\Delta}$ to decrease from 1 to 0.1. Fig. 3.7(a) shows that τ_{coh} increases as α increases from 0 to 0.4π.

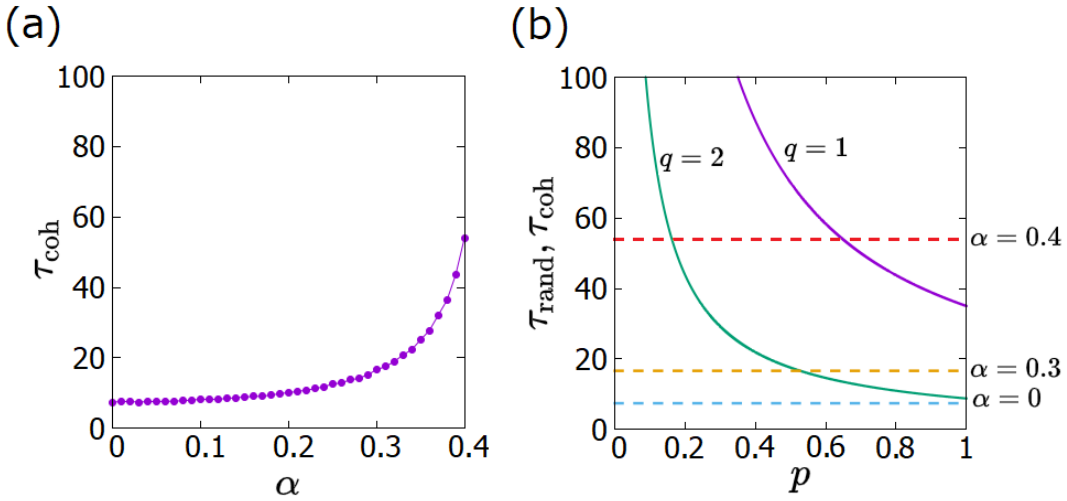

FIGURE 3.7: (a) The timescale for restoring coherence τ_{coh} vs. α. (b) Comparison of the timescales. Solid lines: τ_{rand} for $q = 1, 2$. Dashed lines: τ_{coh} for $\alpha = 0, 0.3\pi, 0.4\pi$. Figures are reprinted from [83].

Now we compare the timescales τ_{rand} and τ_{coh} to analyze the competition between mobility and coupling. In Fig. 3.7(b), the solid lines represent τ_{rand} for $q = 1, 2$ (given by eq. (3.9)), and the dashed lines represent τ_{coh} for $\alpha = 0, 0.3\pi, 0.4\pi$. For $\alpha = 0$, we have $\tau_{\text{coh}} = 7.4$, which is less than τ_{rand} for all p and $q = 1, 2$. This is consistent with the result that the $q = 1$ and 2 twisted states are stable up to $p = 1$ (Fig. 3.4(c)). For $\alpha = 0.3\pi$, we get $\tau_{\text{coh}} = 16.6$, which exceeds τ_{rand} for $q = 2$ at $p \gtrapprox 0.5$. This indicates that the $q = 2$ twisted state is unstable, while the $q = 1$ twisted state remains stable for all p, also consistent with the full numerical results (Fig. 3.4(c)). For $\alpha = 0.4\pi$ and large p, $\tau_{\text{coh}} = 54.0$ is even less than τ_{rand} for $q = 1$, explaining the result that only the synchronized state remains stable (Fig. 3.5(a)). Thus, we have shown that the stability of twisted states for $\alpha < \alpha_c(p)$ is determined by the competition between mobility and coupling, and the independently measured timescales can explain the results: if the perturbation induced by mobility is faster, the twisted state is unstable; if the coupling restores coherence faster, the state is stable.

3.2.2 Traveling waves in the transition region

Next, we consider the effect of mobility in the transition region for $\alpha = \alpha_c(p)$, where the strength of incoherence $\overline{\sigma_\Delta}$ lies between 0 and 1. The spatiotemporal patterns obtained in this range are characterized by the spatiotemporal correlation function of σ_Δ:

$$G_\sigma(x,t) = \left\langle \sigma_\Delta(x',t')\sigma_\Delta(x'+x,t'+t) - \sigma_\Delta^2(x',t') \right\rangle_{x',t'} \tag{3.10}$$

In Fig. 3.8, we show this function calculated over the time window $500 < t' < 1000$ and averaged over 100 independent samples.

For $p = 0$, the random branching patterns of the incoherent state (Fig. 3.2(b)) give a monotonically decaying correlation function in Fig. 3.8(a). For $p > 0$, the mesh-like patterns composed of intersecting traveling waves (Fig. 3.2(i)) show a V-shaped correlation pattern in Fig. 3.8(b). To measure the speed of the traveling waves, we identify the average trajectory $x_w(t)$ of each wave by locating the position where $G_\sigma(x,t)$ is maximized at each t. The average wave speed v_w is measured by fitting $x_w(t)$ to a straight line. Fig. 3.8(c) shows the relationship between v_w and the mobility p. The speed increases linearly with p and slightly decreases when α exceeds α_c.

We define α_c as the minimum α that gives a non-zero value of $\overline{\sigma_\Delta}$. For $p = 0$, α_c is known to be approximately 0.44π. We obtain $\alpha_c(p)$ in Fig. 3.9 by observing whether the system reaches a coherent state over a long period (5×10^5 time units). For each α, we calculate $\overline{\sigma_\Delta}$ for 10 independent samples. If the system reaches a coherent state ($\overline{\sigma_\Delta}$=0) in every sample, we consider $\alpha < \alpha_c$. If any sample shows a non-zero $\overline{\sigma_\Delta}$ at $t = 5 \times 10^5$, we consider $\alpha > \alpha_c$. Fig. 3.9 shows the non-monotonic variation of α_c with p. In the range $0 < p < 0.0002$, increasing p lowers the threshold. For $p > 0.0002$, α_c slowly increases with p. For any $p > 0$, traveling waves above α_c are replaced by chimera states at larger α. The direct transition from coherent to chimera states is only observed at $p = 0$.

3.2.3 The effect of mobility for repulsive coupling

Next, we consider the effect of mobility under repulsive coupling ($\alpha > 0.5\pi$). In the absence of mobility, the spatiotemporal patterns consist of multiple twisted state domains with positive and negative q values, separated by incoherent stripes. The range of the winding number q is determined by a linear stability analysis [84], which shows that the stable range of phase differences is $0.215 < |\Delta| < 0.323$. (For a single-domain twisted state with $N = 500$, this

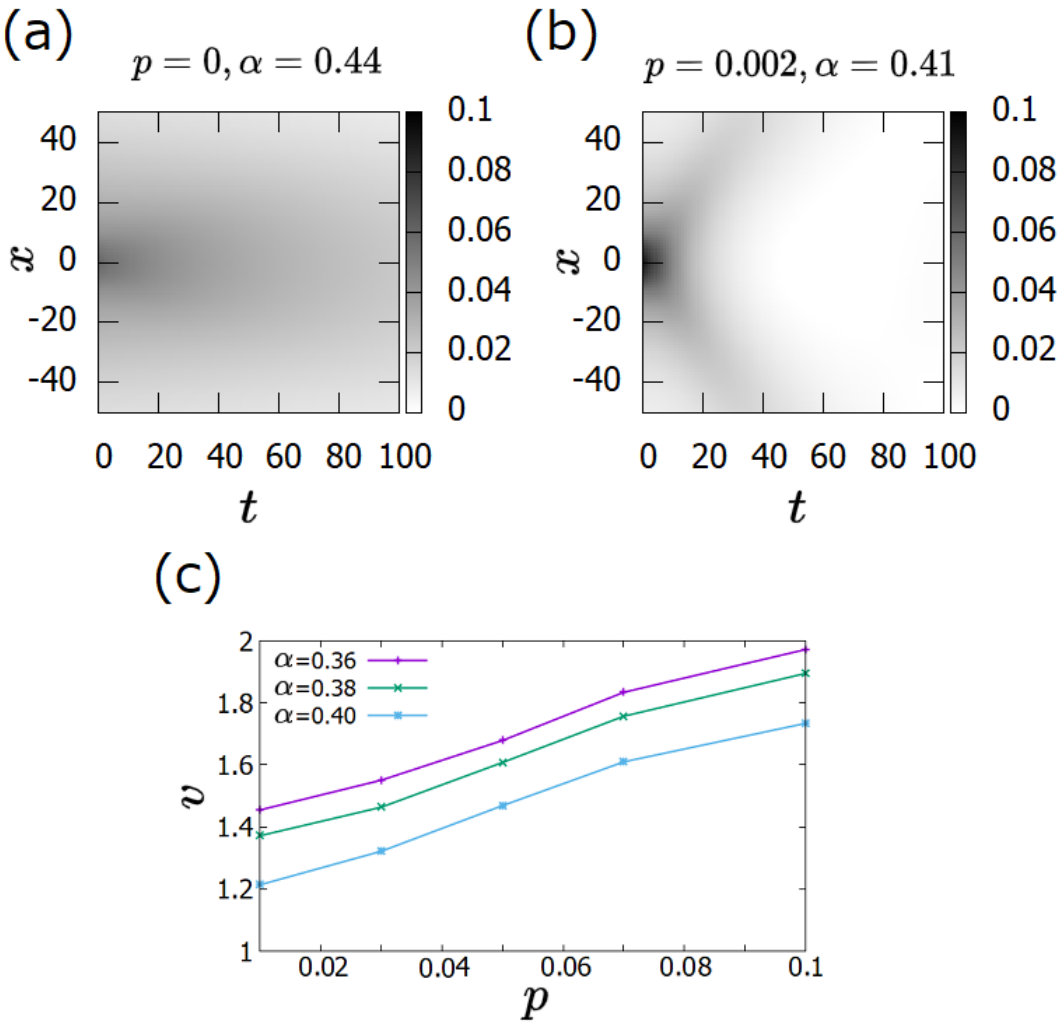

FIGURE 3.8: The spatiotemporal correlation function $G_\sigma(x,t)$ for (a) $(\alpha, p) = (0.44\pi, 0)$, and (b) $(\alpha, p) = (0.41\pi, 0.002)$, which corresponds to the patterns in Fig.3.2 (b) and (i), respectively. The grayscale represents the strength of correlation. (c) The average speed of the traveling wave v_w versus p. Figures are reprinted from [83].

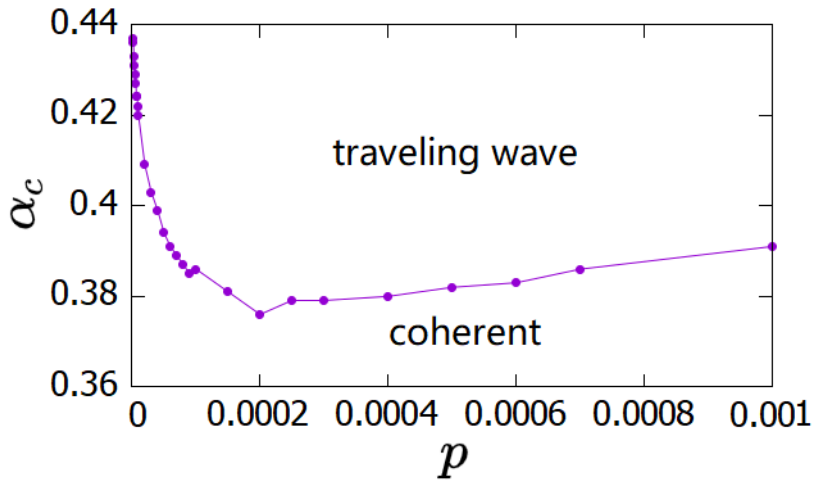

FIGURE 3.9: The transition threshold $\alpha_c(p)$. For $\alpha < \alpha_c$, only the coherent states remain in the long-time limit, while traveling waves appear for $\alpha > \alpha_c$. Figures are reprinted from [83].

corresponds to $54 < |q| < 80$). Due to the larger phase differences, mobility more easily perturbs the twisted states compared to the attractive case. This explains the result that the system falls into a fully incoherent state except for small mobility ($p\delta t \ll 1$), as shown in Fig. 3.3. The typical spatiotemporal pattern in the small mobility region is shown in Fig. 3.2(h), where the perturbation effect appears as noise spots on the twisted domains. The transition threshold from the noise pattern to fully incoherent can also be explained by the competition between two timescales. As seen in Fig. 3.6(d), the decay timescale of $\overline{\sigma_\Delta}(t)$ is on the order of ten time units and is weakly dependent on α. (Note that in the steady state, σ_Δ does not drop to zero due to the coexistence of multiple domains. In this case, redefining the time to decay to 0.5 as τ_{coh} is reasonable.)

Meanwhile, in the absence of coupling, the time for the system to become completely random follows eq. (3.9). Here, by replacing N/q with $2/\Delta$ and using the values $0.215 < |\Delta| < 0.323$, we obtain $\tau_{\text{rand}} \sim 10^{-2}/p$. Thus, if p is on the order of 10^{-3} or smaller, the two timescales are comparable, which matches the threshold found in Fig. 3.3(b).

3.3 Discussion and Conclusion

In this chapter, we investigated the combined effects of mobility due to random exchanges of oscillators and frustration coupling due to phase lag. First, for $\alpha < 0.5\pi$, we show that mobility destabilizes twisted states with large $|q|$ and enlarges the attraction basin of twisted states with small $|q|$, including the fully synchronized state. This is reflected in the decay of the root mean square of q with p. For $\alpha = 0$, we obtain a power law $\sigma_q \sim p^{-1/4}$, explained as follows. In previous studies of non-moving oscillators [169], a relationship between the coupling range R and the standard deviation of q was shown as $\sigma_q \approx 0.19\sqrt{N/R} - 0.11$, which simplifies to $\sigma_q \sim R^{-1/2}$ for $R \ll N$ for $R \ll N$. On the other hand, mobility effectively extends the coupling range. As derived in Ref. [163], for large p, $R_{\text{eff}} \sim p^{1/2}$, meaning that the effective coupling range R_{eff} is given by the mean square displacement of each oscillator in a given microscopic time. Combining these two results, we obtain the power law $\sigma_q \sim p^{-1/4}$.

Second, we analyzed the timescales of randomization and restoration of coherence by considering mobility and coupling separately. By comparing these two timescales, we derive the critical mobility that destabilizes twisted states. For the attractive case, the instability of twisted states leads to jumps to the attraction basins of other twisted states with smaller $|q|$ or to the fully synchronized state. On the other hand, for the repulsive case, the coexistence of twisted states with large $|q|$ is disrupted by small mobility, leading to a fully incoherent state. Thus, mobility has opposite effects on attractive and repulsive couplings.

Third, we identified the grid-like pattern of traveling waves in the attractive coupling case as coherence starts to be lost. We argue that local defects in the phase pattern induced by oscillator exchanges trigger the traveling waves. For p close to 0, increasing p makes traveling waves easier to generate, thereby lowering the critical α_c. For very large p values, all twisted states become unstable, and only the synchronized state survives. In this case, phase patterns are not affected by oscillator exchanges and cannot generate traveling waves. However, the exact mechanism of their formation remains unclear and is subject to future studies.

Chapter 4

Mean-field description of oscillators and brain network

Many biological and neural systems can be viewed as networks comprised of interacting periodic processes, with their collective dynamics shaping their functionality. The dynamics of the system are collectively determined by the microscopic characteristics of individual units, the structure of the network, and their interactions. However, in the case of large systems such as the brain, which contains a vast number of units, analysis is typically feasible only on a simplified model at a coarse level. This limitation arises not just from computational constraints but also from the fact that a detailed understanding of every component does not necessarily enhance our comprehension of the system as a whole. The Ott-Antonsen reduction, a mean-field reduction technique for networks of oscillators is introduced. This method enables the use of a limited number of mean-field variables to describe the network's dynamics, simplifying the analysis of the oscillator network while maintaining a connection between the macroscopic descriptions and the microscopic properties of the underlying system.

The brain is composed of vast networks of neurons, the fundamental units of information processing. Neurons communicate through action potentials (spikes), which are rapid changes in membrane voltage triggered when a neuron's voltage surpasses a certain threshold. The membrane voltage reflects the electrical potential difference across the neuronal membrane and fluctuates dynamically due to ion exchanges mediated by ion channels. These dynamics underlie the generation and propagation of spikes, which are transmitted to other neurons via synaptic connections. Together, these processes form the foundation of neuronal computation and signal transmission, enabling the emergence of collective behaviors such as synchronization. At different scales, synchronization in the neuronal system can be observed, ranging from the microscopic interaction of individual neurons to macroscopic activities spanning entire brain regions.

At the microscopic level, synchronization of single neurons or small neuronal populations (ranging from tens to hundreds) can be observed through single-cell or multi-channel recordings. At the mesoscopic level, neuronal populations within local brain regions achieve coherent activity through electrical dynamics, such as brain waves measured via EEG or MEG. At this scale, the synchronization of beta band oscillations (13–30 Hz), associated with motor control and cognitive stability, and gamma band oscillations (30–100 Hz), crucial for sensory integration and memory encoding, is particularly prominent. At the macroscopic level, the BOLD signal, derived from changes in blood oxygenation and flow, captures low-frequency oscillations (<0.1 Hz) in resting-state networks and reflects large-scale interactions between brain regions, providing insights into functional connectivity. The synchronization observed at different levels plays a crucial role in facilitating various brain functions such as memory [34], computational tasks [37], cognition [166], attention [36], information routing [71], and breathing [146]. As we saw in Section 1.1.5, chimera states are implicated in neurological disorders like epilepsy and Parkinson's disease [53, 80, 132, 162].

In this chapter, we will explain the mean-field description of oscillators and brain networks using the application of the Ott-Antonsen (OA) reduction. We demonstrate the derivation of the OA equation and use a two-population oscillator model as an example to illustrate the application of the OA equation. Following this, we introduce recent advancements in the study of more complex hierarchical networks with a population count greater than two. We then cover some fundamental concepts in the neural system, including basic neural dynamics models and synchronization in neuronal networks. Finally, we focus on the application of the Kuramoto model in brain networks and its connection to the Quadratic-Integrate-and-Fire (QIF) model.

4.1 Ott-Antonsen ansatz

Under certain assumptions, a network of coupled oscillators can be described by a low-dimensional system of differential equations involving several mean-field variables. For instance, for the Kuramoto model with N oscillators, we can derive a two-dimensional system for the complex order parameter $Z = R^{i\Theta}$(see Eq. 1.11).

First, we consider an oscillator system containing many ($N \to \infty$) populations. Each population contains many oscillators where the phase follows

the equation:

$$\frac{\mathrm{d}\theta_k^\sigma}{\mathrm{d}t} = \omega_k^\sigma + \mathrm{Im}\left(H_k^\sigma(t)e^{-i\theta_k^\sigma}\right), \tag{4.1}$$

where θ_k^σ is the phase of oscillator k in population σ, and H_k^σ is the input to oscillator θ_k^σ from the other oscillators. For the single population Kuramoto model 1.10, we have

$$\begin{aligned} \frac{\mathrm{d}\theta_k}{\mathrm{d}t} &= \omega_k + \mathrm{Im}\left(\frac{K}{N}\sum_{j=1}^{N} e^{i(\theta_j-\theta_k)}\right) && (4.2)\\ &= \omega_k + \mathrm{Im}\left(KZ(t)e^{-i\theta_k}\right), && (4.3) \end{aligned}$$

where $Z(t)$ is the complex Kuramoto order parameter defined in Eq. 1.11. The Kuramoto model is equivalent to Eq. 4.1 with $H(t) = KZ(t)$, meaning that the oscillators' interaction depends only on the order parameter. This is called a mean-field coupling where each oscillator is coupled to an average of all oscillators in the system.

System of form Eq. 4.1 also includes other models ranging from the Kuramoto-Sakaguchi model to more specific neuron models. If we consider a system of M populations with N Kuramoto-Sakaguchi oscillators in each population,

$$\frac{\mathrm{d}\theta_k^\sigma}{\mathrm{d}t} = \omega_k^\sigma - \sum_{\tau=1}^{M}\frac{K_{\sigma\tau}}{N}\sum_{l=1}^{N}\sin(\theta_k^\sigma - \theta_l^\tau + \alpha_{\sigma\tau}), \tag{4.4}$$

the Kuramoto order parameter for each population σ is defined as

$$Z_\sigma = \frac{1}{N}\sum_{l=1}^{N} e^{i\theta_l^\sigma}. \tag{4.5}$$

Thus, the driving force for each oscillator in Eq. 4.1 is given by the linear combination of the mean fields of all the population:

$$H_\sigma = \sum_{\tau=1}^{M} K_{\sigma\tau}e^{-i\alpha_{\sigma\tau}}Z_\tau. \tag{4.6}$$

The Theta neuron and quadratic integrate-and-fire neurons also satisfy Eq. 4.1. The Theta neuron [33] is a model used in computational neuroscience to describe the dynamics of neuronal activity, particularly focusing on the timing of action potentials (spikes) rather than their detailed shapes. By representing the neuronal membrane potential as an angle variable on a circle

(hence "Theta"), the model captures essential features of oscillatory behavior and synchronization in neural populations. It is instrumental in studying phenomena such as brain wave patterns, neural synchronization, and the role of rhythmic firing in cognitive processes. Consider a single population of Theta neurons:

$$\dot{\theta}_k = 1 - \cos\theta_k + (1 + \cos\theta_k)(\eta_k + \kappa I), \tag{4.7}$$

where $\theta_k \in [-\pi : \pi]$ is the phase variable and η_k is the excitability of the k-th neuron, respectively. The neurons fire when the phase cross $\theta = \pi$. κ is the coupling strength, and I is an input current which can be attributed to both external input and network interactions. Eq. 4.7 can be transformed into the form of Eq. 4.1 by letting

$$\omega_k = 1 + \eta_k + \kappa I, \tag{4.8}$$
$$H_k = i(\eta_k + \kappa I - 1). \tag{4.9}$$

The neuron described by this equation undergoes a saddle-node bifurcation as $\eta_k + \kappa I$ is varied. For $\eta_k + \kappa I < 0$, the Theta neuron is excitable: the phase will relax to the quiescent state if the phase is under the threshold, and a spike will be emitted if the phase exceeds the threshold. For $\eta_k + \kappa I > 0$, the Theta neuron will periodically fire. The Theta neuron is identical to the so-called quadratic integrate and fire neurons if we set $V_k = \tan(\theta_k/2)$; here, V_k is the membrane voltage of neuron k and obeys:

$$\dot{V}_k = V_k^2 + \eta_k + \kappa I. \tag{4.10}$$

All of these models are reduced to Eq. 4.1, indicating that they can be subjected to the Ott-Antonsen reduction.

4.1.1 Derivation of Ott-Antonsen equation

Considering an infinite number of oscillators ($N \to \infty$), suppose that the driving force is equal for all oscillators in any given population $H_k^\sigma = H^\sigma$, and that the natural frequencies of the oscillators ω_k^σ in a population is drawn from a distribution $g_\sigma(\omega)$. The state of a population is described by the probability density $f_\sigma(\omega^\sigma, \theta^\sigma, t)$. Conservation of the number of oscillators implies that Eq. 4.1 can be represented by the continuity equation

$$\frac{\partial f_\sigma}{\partial t} + \frac{\partial}{\partial \theta^\sigma}(f_\sigma v_\sigma) = 0, \tag{4.11}$$

where $v_\sigma = \omega_\sigma + \mathrm{Im}\left(H_\sigma(t)e^{-i\theta}\right)$. Ott and Antonsen [115] discovered the existence of an invariant manifold; here the invariant manifold refers to a specific form of the phase distribution function $f(\omega,\theta,t)$. If $f(\theta,\omega,0)$ lies on this manifold, it will remain on the manifold for any $t \geq 0$. The Kuramoto order parameter Z can be expressed as

$$Z(t) = \int_{-\infty}^{\infty}\int_{0}^{2\pi} f(\omega,\theta,t)e^{i\theta}\mathrm{d}\theta\mathrm{d}\omega. \tag{4.12}$$

Subsequently, we will see that the time evolution of the system on this invariant manifold can be described by the time evolution equation of Z. Firstly, expanding $f(\omega,\theta,t)$ in a Fourier series in θ, we get

$$f(\omega,\theta,t) = \frac{g(\omega)}{2\pi}\left(1 + \sum_{n=1}^{\infty} f^{(n)}(\omega,t)e^{in\theta} + \text{c.c.}\right), \tag{4.13}$$

where c.c. stands for complex conjugate. Then Ott and Antonsen considered a special class of $f^{(n)}$ such that

$$f^{(n)}(\omega,t) = [a(\omega,t)]^n, \tag{4.14}$$

where $|a(\omega,t)| < 1$ .This is the key ansatz that the Fourier coefficients are powers of a single function $a(\omega,t)$. Substituting Eq. 4.13 into Eq. 4.11 we obtain

$$\frac{\partial a}{\partial t} + i\omega a + \frac{1}{2}(Ha^2 - \overline{H}) = 0, \tag{4.15}$$

where the overline represents the complex conjugate. Then substituting Eq. 4.14 into Eq. 4.12

$$Z = \int_{-\infty}^{\infty} \overline{a}(\omega,t)g(\omega)d\omega, \tag{4.16}$$

Thus the system is reduced to a θ-independent single ordinary differential equation. More specifically, we can use the residue theorem to get the exact form of the Z, if the distribution of nature frequency $g(\omega)$ is Lorentzian,

$$g(\omega) = \frac{1}{\pi}\frac{\Delta}{(\omega-\omega_0)^2 + \omega^2}, \tag{4.17}$$

where Δ is the width and ω_0 is the mean of the distribution. Since $g(\omega)$ has 2 poles at $\omega = \omega_0 \pm i\Delta$, under the assumption that $|a(\omega,t)| \to 0$ as $\mathrm{Im}(\omega) \to -\infty$, it can be obtained that $Z = \overline{a}(\omega_0 - i\Delta, t)$. Finally, the time

evolution equation of the order parameter can be obtained as

$$\dot{Z} = (-\Delta + i\omega_0)Z + \frac{1}{2}H - \frac{1}{2}\overline{H}Z^2. \tag{4.18}$$

This is called the Ott-Antonsen equation. If the system initially satisfies Eq. 4.14, the system will always be on the invariant manifold. Even if it is not on the manifold, Ott and Antonsen showed that there are densities f that are attracted to the invariant manifold, which means the Ott-Antonsen equation can describe the long-term dynamics of a large range of the initial phase distribution $f(\omega, \theta, t)$.

4.1.2 OA ansatz on 2 population of oscillators

Using the OA equation, describing the mean-field behavior of a system with an infinite number of oscillators is very simple. If the natural frequencies of the oscillators follow a Lorentzian distribution, the system's Kuramoto order parameter R follows

$$\dot{R} = \left(-\Delta + \frac{K}{2} - \frac{K}{2}R^2\right) R. \tag{4.19}$$

It is not difficult to know that when $K < K_c = 2\Delta$, $R = 0$, and when K exceeds 2Δ, a pitchfork bifurcation occurs, making the solution $R = \sqrt{1 - 2\Delta/K}$ stable and the solution $R = 0$ unstable.

When the oscillator system is composed of multiple populations, even if they are identical (that is, the populations exhibit completely identical behavior when uncoupled), when they are coupled together, they can exhibit a form of dynamical symmetry-breaking behavior, the chimera state. In 2008, Abrams *et al.* used the OA reduction to study a system where the oscillators are divided into two populations and investigated its chimera state [2]. The oscillators are all-to-all coupled, and the time evolution of their phases follows Eq. 4.4 with $M = 2, N \to \infty$, with a strong coupling within each population $k_s = k_{11} = k_{22}$ and a weak coupling between the populations

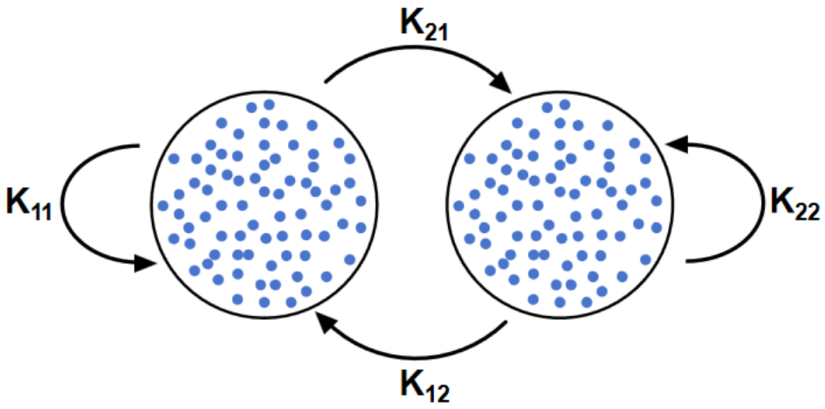

FIGURE 4.1: Schematic diagram of the two populations model.

$k_n = k_{12} = k_{21}$. Using Ott-Antonsen reduction, they reduced it to the 3-dimensional system

$$\dot{r}_1 = \frac{1-r_1^2}{2}(k_s r_1 \cos(\alpha_s) + k_n r_2 \cos(\alpha_n - \psi)), \tag{4.20}$$

$$\dot{r}_2 = \frac{1-r_2^2}{2}(k_s r_2 \cos(\alpha_s) + k_n r_1 \cos(\alpha_n + \psi)), \tag{4.21}$$

$$\dot{\psi} = \frac{1+r_1^2}{2r_1}(k_s r_1 \sin(\alpha_s) + k_n r_2 \sin(\alpha_n - \psi)) - \frac{1+r_2^2}{2r_2}(k_s r_2 \sin(\alpha_s) + k_n r_1 \sin(\alpha_n + \psi)), \tag{4.22}$$

where $\psi = \phi_1 - \phi_2$, and α_s and α_n are intra-population and inter-population phase lag.

For homogeneous phase lag $\alpha_s = \alpha_n$, Ref. [2] shows that the system displays bifurcation between chimera states. Let $A = (k_s - k_n)/(k_s + k_n)$. For α close to $\pi/2$, increasing A from 0 first leads to a saddle-node bifurcation that results in a stable chimera state, i.e., $r_1 = 1$ and $r_2 = r < 1$. As A increases, a supercritical Hopf bifurcation occurs, causing the stable chimera to become a breathing chimera where $r_1 = 1$ and r_2 oscillates. Further increasing A leads to the disappearance of the breathing chimera in a homoclinic bifurcation. In addition, there are many variations in the study of the two-population model, such as introducing frequency heterogeneity [75], network heterogeneity [79], noise [77], and phase lag heterogeneity [97]. There are also studies involving three populations [95, 96].

As the simplest hierarchical network, this 2-population model has been experimentally confirmed to exhibit chimera states where one population is

synchronized while the other is not [98] and has the potential to be used for simulating the left and right hemispheres of the brain. The 2-population model is well-studied, but its extended version, the M-population model, has not been thoroughly investigated due to the increased complexity, making analytical solutions relatively difficult. Again taking neuroscience as an example, the M-population model is also very important because the brain is not just divided into the left and right hemispheres; it can be more finely divided into many different brain regions which can be viewed as a hierarchical network formed by the interactions of M oscillator populations (Figure 4.2). Using the OA reduction method, the behavior of each population can be described by two variables, allowing the system of M brain regions to be described by $2M$-dimensional dynamics (this will be explained in detail in the subsequent sections).

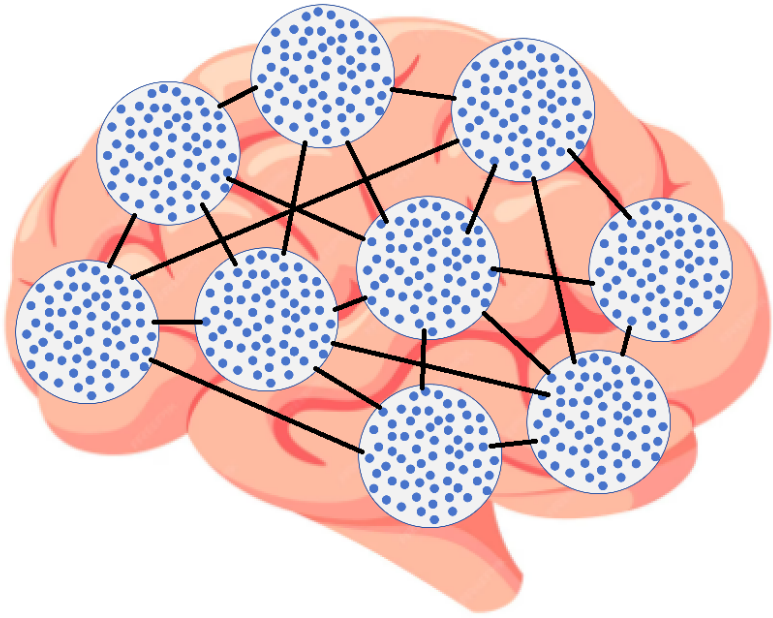

FIGURE 4.2: A schematic diagram of the brain network. The cerebral cortex is divided into multiple brain regions, and interactions exist between these regions.

4.1.3 Hierarchical network

Hierarchical networks are characterized by their multi-level organization, where nodes are grouped into modules or populations that are further organized into larger modules, creating a nested structure, and providing a framework to understand complex dynamical behaviors arising from the interplay between local and global interactions. In coupled phase oscillator networks, the synchronization process can exhibit distinct patterns at different hierarchical levels. For instance, oscillators within the same population may synchronize rapidly due to strong intra-cluster coupling, while synchronization between different populations occurs more gradually, reflecting weaker inter-population coupling. This multi-scale synchronization process can lead to complex temporal patterns and spatial coherence, which are not observed in simpler network topologies.

The hierarchy of local and global synchrony, i.e., synchrony within and between populations of Kuramoto oscillators is studied in Ref. [144]. Utilizing the Ott-Antonsen ansatz, local synchrony within communities and global synchrony between communities can be described by low-dimensional equations. The research highlights the hierarchical nature of synchrony, where local synchrony often precedes global synchrony depending on the relative strengths of intra-community and inter-community coupling. Analytical and numerical results reveal that community structure significantly influences the transition to synchrony, with bifurcations indicating different synchronization regimes.

On the other hand, a hierarchical system has the ability to generate a large repertoire of metastable chimera states which reflects properties common to many real-world complex dynamical systems [139]. The model comprises 8 populations of 32 Kuramoto-Sakaguchi oscillators with identical natural frequencies. Each oscillator is fully connected within its community and has random connections to oscillators in other communities. The measures of metastability and chimera-like states proposed are,

$$\lambda = \langle \mathrm{Var}_T(R_\sigma(t)) \rangle_\sigma , \tag{4.23}$$

$$\chi = \langle \mathrm{Var}_\sigma(R_\sigma(t)) \rangle_T . \tag{4.24}$$

λ shows the variation in the synchronization degree of each population over time. If this value is high, it indicates that the degree of variation in the synchronization degree of each population over time is large. In other words, these populations do not remain consistently in a synchronized or desynchronized state but instead switch back and forth between the two states.

This suggests that these populations exhibit metastability. And χ shows the variance of the synchronization degree of all populations at each moment, representing the chimera-like degree of the system.

Ref. [76] investigates the behavior of chimera states in networks of coupled oscillators organized in a ring. They focused on networks with varying numbers of populations and different levels of frequency heterogeneity. The findings reveal that macroscopic chaos emerges when more than five populations are considered, but this chaotic behavior vanishes as the number of populations increases. The paper provides new insights into the stability and dynamics of chimera states across different network configurations, bridging the gap between small and large network studies.

Although a few previous studies, including those mentioned above, have explored the hierarchical structure of oscillator networks consisting of multiple populations, the effects of the phase lag parameter α remain unexplored. In Chapter 5, we will discuss the impact of α on a ring of nonlocally coupled M-population system with each population described by the mean-field OA equation.

4.2 Oscillators model in neuronal network

4.2.1 Computational model of the brain

The cerebral cortex of mammalian brains serves as an excellent example of a hierarchically coupled system, ranging from the microscopic level of individual neurons, through the mesoscopic level of local neural circuits and columns, to the macroscopic level of nerve fiber projections connecting different brain areas. To study the brain, many computational models from the celebrated Hodgkin-Huxley model [59], which describes the temporal evolution of ionic flux across neuronal membranes and thus gives rich dynamics and precise prediction, to simple models like integrate-and-fire models, which are used for their tractability and computational efficiency, have been proposed to simulate the activities of neurons and neural networks, helping researchers understand the mechanisms of information processing in the brain. By simulating individual neurons or neural networks, these models can explain phenomena such as neuronal firing patterns and synaptic plasticity, revealing how neurons transmit and integrate information. A practical way to categorize these computational models is by their scale of neurophysiological activity, which can be broadly divided into:

1. Microscopic models, focusing on the level of single cells and microcircuits;
2. Mesoscopic models, targeting the level of neural masses and neural fields;
3. Macroscopic models, incorporating the larger scale structures of the connectome or white matter.

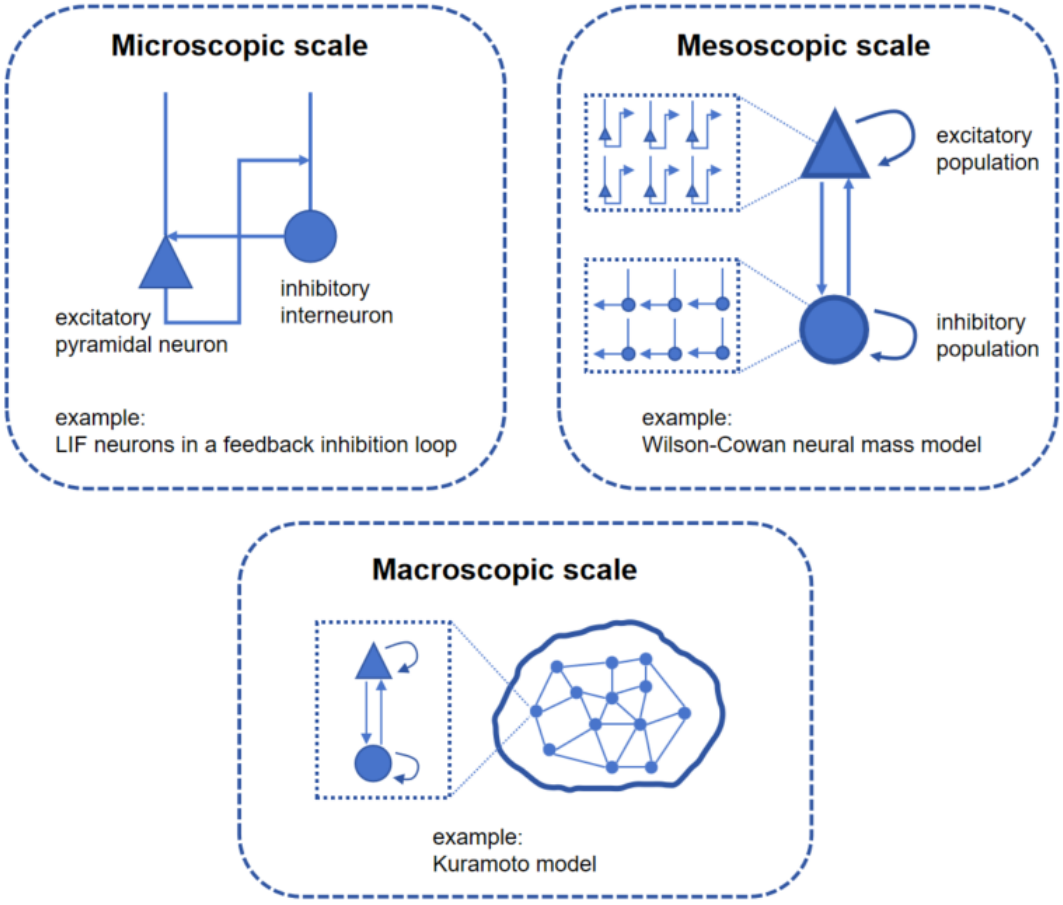

FIGURE 4.3: Illustration of computational model at the three scales.

Figure 4.3 illustrates the hierarchical structure of different models. At the microscopic level, an example of a circuit composed of two leaky integrate-and-fire neurons is shown here. The triangle represents a pyramidal neuron, which is connected to a circular interneuron via an excitatory synapse. The interneuron, in turn, connects back to the pyramidal neuron via an inhibitory

synapse, forming an inhibition feedback loop. The dynamics of these two neurons follow the equation:

$$\tau \frac{\mathrm{d}V_i}{\mathrm{d}t} = -(V_i(t) - V_L) + RI_i(t) \tag{4.25}$$

where V_i is the membrane potential of the neurons, V_L is the resting membrane potential, R is the constant representing the corresponding membrane resistance, I_i is the synaptic input from other neurons and background, and τ is the time constant that determines the leakage rate of V_i. When the membrane potential V_i reaches a threshold, a spike is fired, and V_i is reset to V_L. Also, many other neuronal models including the QIF model are examples of microscopic models.

At the mesoscopic level, the Wilson-Cowan model [170] serves as a good example. In this model, a population of excitatory neurons (E) is coupled with a population of inhibitory neurons (I). The equations no longer describe the behavior of individual neurons but the mean activity of a large number of neurons (typically the average firing rate of neurons), and read

$$\tau \frac{\mathrm{d}E(t)}{\mathrm{d}t} = -E(t) + (1 - E(t)) f_E(w_{EE}E - w_{EI}I + h_E(t)), \tag{4.26}$$

$$\tau \frac{\mathrm{d}I(t)}{\mathrm{d}t} = -I(t) + (1 - I(t)) f_I(w_{IE}E - w_{II}I + h_I(t)), \tag{4.27}$$

The terms $w_{EE}, w_{EI}, w_{IE}, w_{II}$ represent the connection weights between the neuronal populations, indicating how different types of neurons influence each other's activity. $h_{E,I}$ is the external input. The function $f_{E,I}$ is often represented as a sigmoid function, used to convert the input into the population's firing rate, which describes how many neurons in the population reach the firing threshold.

At the macroscopic level, the brain is viewed as a network composed of many brain regions (nodes). Many researchers use the Kuramoto model to represent the activity of a brain region [13, 18, 110, 135]. The Kuramoto model treats each brain region as an oscillator, describing the dynamics of each region through changes in phase and coupling between phases. It is computationally efficient, making it particularly useful for large-scale networks, especially when studying synchronization between brain regions. However, it is important to note that while the Kuramoto model excels at describing oscillatory synchronization, it is a highly abstract model with no specific biophysical basis. This means it cannot directly explain biological mechanisms of neuronal populations, such as synaptic transmission, neuromodulation, or

electrochemical processes.

4.2.2 Synchronization in neuronal network

The phenomenon of synchronization in neural networks refers to the spontaneous coordination of firing behaviors among a large number of neurons under specific conditions, causing them to generate action potentials in the same or similar rhythms. Although neurons typically fire independently, external stimuli, coupling, or activity from other neurons can lead to synchronized activity. This synchronization plays a crucial role in many brain functions, from perception and motor control to cognitive processes. Synchronization can also occur at different spatial scales:

Microscopic level: This refers to the synchronized firing of neurons within smaller regions of a neural network. For example, specific groups of neurons in the cortex may exhibit synchronized activity while performing a task, which manifests as synchronized local field potentials or brainwaves. Specifically, when a large number of neurons fire simultaneously or in a coordinated manner, the resulting electric fields can superimpose, creating measurable electrical activity detectable through techniques such as EEG [46, 155]. These brainwaves are usually categorized into different frequency bands, with each band associated with distinct neuronal synchronization patterns and functional states of the brain:

1. Alpha rhythm (8-12 Hz): Associated with attention and wakefulness.

2. Gamma rhythm (30-100 Hz): Linked to cognitive functions, memory processing, perception, and conscious activities.

3. Theta rhythm (4-8 Hz): Related to learning, memory, and navigation, particularly in the hippocampus.

The amplitude of brainwaves is closely related to the degree of synchronization among neuron populations. When neurons engage in highly synchronized activity, the resulting brainwave amplitude is typically larger. Conversely, when neuronal activity is asynchronous, the brainwave amplitude is lower. High-amplitude brainwaves usually indicate that more neurons are participating in collective activity at the same time.

Phase synchronization of brainwaves across different brain regions can also be detected. For instance, during the execution of a task, the prefrontal cortex and sensory cortex may engage in synchronized activity at the same frequency, which can be detected as cross-regional phase synchronization via

EEG. This synchronization is believed to play a crucial role in functional connectivity and information processing within the brain.

Macroscopic level: This refers to the synchronized activity of neuron populations across distant regions of the brain. This phenomenon is crucial for communication between different brain areas and serves as the basis for information integration, decision-making, and consciousness. The neural electrical activity associated with global synchronization is primarily recorded using techniques like EEG or MEG, while fMRI, through the detection of blood-oxygen-level-dependent (BOLD) signals [18], indirectly reflects functional connectivity between brain regions.

In the following paragraphs, we will focus on the model that describes the coupling dynamics between brain regions at a macroscopic level, which is called a brain network model.

4.3 Brain network model

Brain network models aim to simplify and understand the complexity of brain-wide communication by representing brain regions as nodes and the connections between them as edges. These models are grounded in neuroimaging data, such as diffusion MRI (dMRI) and functional MRI (fMRI), and utilize graph theory and dynamic systems to simulate interactions between different brain areas. The construction of such models involves two key elements: the choice of parcellation method and the selection of node dynamics.

Parcellation Methods: Parcellation is the process of dividing the brain into distinct regions of interest (ROIs) that act as the nodes in a network model. Different parcellation schemes can significantly affect the spatial resolution and topological properties of the resulting brain model. Commonly used anatomical criteria for parcellation include gross anatomy, cytoarchitecture, myeloarchitecture, chemoarchitecture and gene expression profiles. Functional parcellation, on the other hand, divides brain regions based on correlations in activity during resting-state or task-based fMRI. Functional parcellations generally outperform anatomical atlases in capturing functional connectivity (FC) patterns at finer voxel scales, but anatomical parcellations offer clearer interpretability when considering results in light of existing neuroscience literature.

Node Dynamics: Node dynamics describe the temporal evolution of activity in each brain region. Each node typically represents the mean activity

of a population of neurons, and the dynamics of this ensemble can be reduced to a low-dimensional description. Several models are used to simulate these dynamics, ranging from simple phenomenological models, such as the Kuramoto model, to more biologically detailed ones, like the Wilson-Cowan model or thalamocortical motifs. For example, the Kuramoto model treats each node as a phase oscillator, where its dynamics are governed by a natural frequency and interactions with other nodes. This model is useful for understanding large-scale synchrony across brain regions. In contrast, more detailed models like the Wilson-Cowan model account for excitatory-inhibitory interactions, providing a richer depiction of neural dynamics. Some models, like bifurcation models, can capture both asynchronous and synchronous states, allowing for the study of transitions between different dynamic regimes.

Many other points also can be taken into consideration, like the inclusion of conduction delays or noise. For example, delays which account for the time it takes for signals to propagate across brain regions are important in electrophysiological studies, but may be less relevant when modeling slower BOLD signals in fMRI data. Transmission delays can significantly impact network synchronization and oscillation frequencies, highlighting the importance of tuning these parameters based on the scale of the dynamics being studied.

4.3.1 Kuramoto model in brain network

Modern approaches often involve using phase oscillators to model the dynamics of brain regions, allowing for the study of phenomena such as phase locking and synchrony between brain areas, which are crucial for understanding large-scale brain activity[3, 13, 18, 20, 64, 108, 110, 116, 119, 120, 125, 129, 135, 153, 164, 168, 176]. For example, Ref. [18] constructs a large-scale neural dynamic model to investigate the relationship between local network oscillations and resting-state functional connectivity (FC). The model aims to explain why distinct brain regions exhibit synchronous activity during rest, i.e., functional connectivity. Specifically, the authors utilized structural connectivity (SC) data from the human brain, where each network node represents a population of neurons oscillating spontaneously in the gamma frequency range (30-80 Hz). By combining structural connectivity and conduction delays, they employed the Kuramoto phase oscillator model to simulate the interactions between these nodes.

Structural Connectivity (SC): The SC data used in the model was derived from diffusion spectrum imaging (DSI) of the human brain, including the structural connectivity between 66 brain regions, with each region acting

as a network node. The 66 brain regions are downsampled from the high-resolution connection matrix (998 regions of interest) obtained by Hagmann et al. [52].

Conduction Delays: The conduction delays were computed based on the fiber lengths between brain regions, reflecting the time it takes for neural signals to propagate through the brain. The model uses an average delay parameter to represent the transmission speed between nodes.

The node dynamics follows:

$$\frac{\mathrm{d}\theta_n}{\mathrm{d}t} = \omega_n + k \sum_{p=1}^{N} C_{np} \sin\left(\theta_p(t - \tau_{np}) - \theta_n(t)\right) + \eta_n(t) \tag{4.28}$$

where ω_n is the intrinsic frequency of the node, drawn from a Gaussian distribution centered around 60 Hz, C_{np} is the coupling strength from node p to node n, derived from the SC matrix. τ_{np} is the conduction delay between node p and node n. So this model integrated a realistic setting of both empirical anatomical connectivity and axonal conduction speed.

To compare the model's neural activity with the BOLD signal from fMRI, the authors of [18] used the Balloon-Windkessel model, which simulates the transformation of neural activity into BOLD signals. The BOLD signal reflects low-frequency fluctuations, particularly those below 0.1 Hz. The study demonstrated that slow-wave fluctuations in the local field potentials (LFPs) of the gamma range are associated with the low-frequency components of the BOLD signal. The model found that under certain combinations of coupling strength k and conduction delay τ, local brain regions form partially synchronized clusters, while the global brain network does not fully synchronize. The synchronization within these local clusters leads to significant correlations in BOLD signals, successfully reproducing the experimentally observed resting-state networks (RSNs).

4.3.2 Kuramoto model for populations of QIF neurons

Although the Kuramoto model has been used in many studies for the dynamics of nodes in brain networks and is indeed useful, as previously mentioned, it is somewhat lacking in biological realism as a phenomenological model and does not relate well to parameters in neuroscience. However, a recent work by Clusella *et al* [24] showed that the KS model can be derived from a population of weakly coupled, nearly identical quadratic integrate-and-fire (QIF) neurons, establishing a direct relationship between the phase lag α and the electrical and chemical coupling strengths.

In their paper, the authors considered the QIF model, which is a simplified quadratic equation that captures the membrane potential changes and spiking behavior of neurons. The detailed aspects of the QIF model used in their paper are as follows:

$$\tau \frac{dV_i}{dt} = V_i^2 + \eta_i + \epsilon I_{i,syn}(t) \tag{4.29}$$

where V_i is the membrane potential of neuron i, τ is the membrane time constant, and η_i represents the external current input, which can vary from neuron to neuron. The quadratic term V_i^2 introduces nonlinearity, enabling the model to capture the rapid increase in membrane potential that occurs when a neuron fires. When the membrane potential V_i reaches a peak value V_p, the

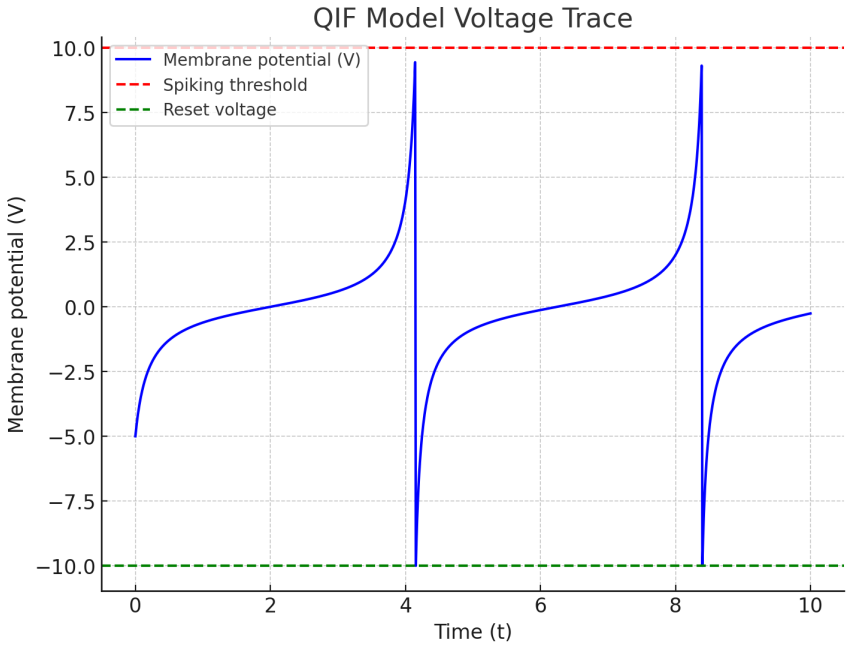

FIGURE 4.4: QIF model's membrane potential V over time t. The voltage increases quadratically, and once it reaches the spiking threshold (marked by the red dashed line), it resets to the reset voltage (marked by the green dashed line). This cycle repeats, representing the periodic spiking behavior of the QIF neuron.

model assumes the neuron fires an action potential, and the membrane potential is instantaneously reset to a reset value V_r. In this paper, a symmetric resetting rule is used, where $V_p = -V_r$, and the peak value V_p tends toward infinity. This makes the QIF model equivalent to the "theta neuron model"

in certain conditions. In this model, neurons interact via both chemical and electrical synapses, represented by the synaptic input $I_{i,syn}(t)$, which consists of two components:

$$I_{i,syn}(t) = g(v(t) - V_i) + J_{\tau r}(t). \tag{4.30}$$

Electrical Synapses (coupling strength g): Neurons are coupled diffusively through the average membrane potential $v(t)$ of the network, expressed as:

$$v(t) = \frac{1}{N}\sum_{j=1}^{N} V_j(t). \tag{4.31}$$

Chemical Synapses (coupling strength J): These synapses are mediated by the average firing rate $r(t)$ of the neuronal population, expressed as:

$$r(t) = \frac{1}{N}\sum_{j=1}^{N}\sum_{k}\delta\left(t - t_j^{(k)}\right) \tag{4.32}$$

where $\delta(t)$ is the Dirac delta function, and $t_j^{(k)}$ is the time of the k-th spike of neuron j. Here, the QIF model demonstrates self-sustained oscillatory behavior. In the absence of synaptic input ($I_{i,syn}(t) = 0$), neurons can generate periodic oscillations due to the positive external currents η_i, which mimics the spontaneous firing behavior observed in biological neurons.

The authors derive a version of the KM that is valid for populations of QIF neurons. The KM is shown to approximate the dynamics of QIF neurons when both chemical and electrical couplings are weak

$$\dot{\theta}_i = \omega_i + \frac{K}{N}\sum_{j=1}^{N}\sin(\theta_j - \theta_i - \alpha) + \sin\alpha \tag{4.33}$$

$$K = \frac{\epsilon}{\tau}\sqrt{\left(\frac{J}{\pi}\right)^2 + g^2} \tag{4.34}$$

$$\alpha = \arctan\left(\frac{J/\pi}{g}\right) \tag{4.35}$$

(see derivation in Appendix C). They found that the phase lag parameter α corresponds to the balance between chemical coupling J and electrical coupling g and plays a crucial role in the synchronization properties of the network. In particular, networks with both types of coupling can achieve synchronization at certain coupling strengths. Also, they compare their derived

KM with exact mean-field models, confirming that the KM provides a good approximation of the dynamics of QIF neurons under the conditions of weak coupling and weak heterogeneity.

Building on the discussions in the previous sections—where the Kuramoto-Sakaguchi model was validated as a reasonable representation of individual neurons at the microscopic level, and the Ott-Antonsen reduction was shown to effectively capture the dynamics of KS oscillator populations—we were motivated to apply the OA-reduced model to represent node dynamics within a brain network. Although OA-reduced oscillator models have been widely studied, most previous research has focused on interactions between two populations. The study of large-scale networks, where multiple OA-reduced oscillator populations interact with each other to form hierarchical networks, remains to be explored. We will address this issue in the next chapter.

4.3.3 Metastability in the brain

Metastability refers to the ability of a system to remain in a quasi-stable state for extended periods before transitioning to another state. In the brain, metastability allows neural networks to flexibly switch between different activity states, achieving a balance between local synchronization (integration) and global desynchronization (segregation) [157]. This dynamic equilibrium underpins cognitive flexibility, enabling the brain to adapt to diverse tasks and stimuli without becoming locked into fixed patterns of activity. This balance between integration and segregation is essential for supporting the complex cognitive, sensory, and motor functions of the brain [69]. Studies using neuroimaging techniques, such as EEG and fMRI, have provided neurophysiological evidence of metastability [126, 156]. For instance, Popa et al. observed alternating patterns of synchrony and quasi-independent activity in the gamma frequency bands within neural ensembles of the cat brain [126].

Chapter 5

Multi-populations of Kuramoto-Sakaguchi oscillators

This chapter explores the dynamics of systems composed of M populations of phase oscillators. We begin by introducing the model framework, detailing the coupling schemes and the interactions between populations. Next, we examine the spatiotemporal patterns that arise within and between populations. This is followed by an analysis of traveling wave solutions and their dependence on system parameters. Subsequently, we investigate the metastable properties of the system, with a focus on the transitions between coherence and partial synchronization.

The content of this chapter is adapted from the author's published work: B. Li and N. Uchida, Chaos 35, 013105 (2025). DOI: 10.1063/5.0220321

5.1 Model

We consider a KS model consisting of M populations, each containing N oscillators. The governing equations are as follows:

$$\frac{\mathrm{d}\theta_k^\sigma}{\mathrm{d}t} = \omega_k^\sigma - \sum_{\tau=1}^{M} \frac{K_{\sigma\tau}}{N} \sum_{l=1}^{N} \sin(\theta_k^\sigma - \theta_l^\tau + \alpha_{\sigma\tau}), \tag{5.1}$$

where σ is the index of the population, and k is the index of the oscillator within the population. Here we assumed that the N oscillators in each population (σ) have the all-to-all coupling with the coupling constant $K_{\sigma\sigma}$ and are also coupled to the oscillators in the other populations ($\tau \neq \sigma$) with the strength $K_{\sigma\tau}$. In the thermodynamic limit $N \to \infty$, the collective dynamics can be described by the oscillator density $f^\sigma(\theta, \omega)$, which, through the OA ansatz [115] (see Appendix A for details), can be reduced to a low-dimensional mean-field dynamics. The complex order parameter is given

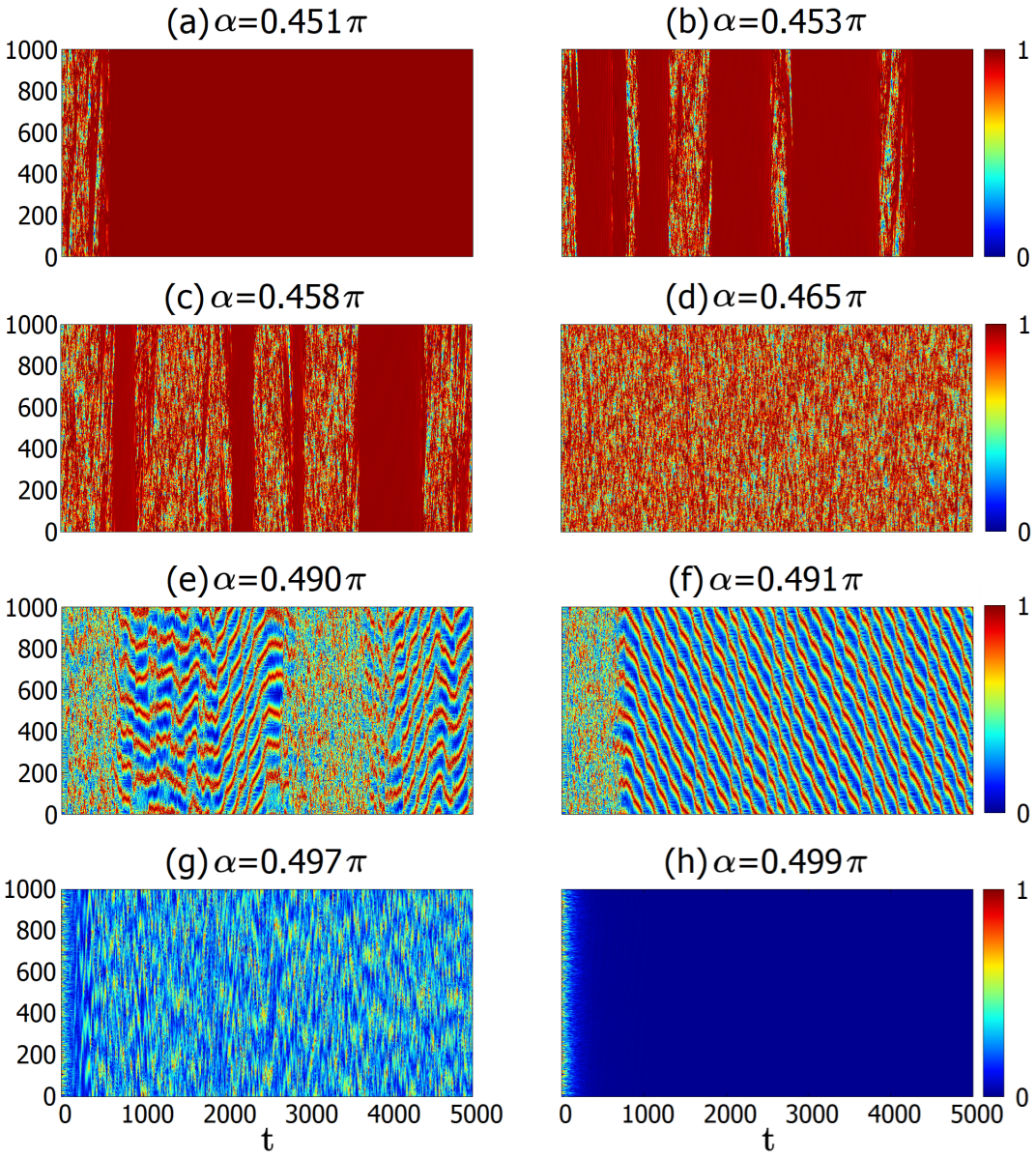

FIGURE 5.1: Spatiotemporal patterns of amplitudes $r_\sigma(t)$. The vertical axis represents the index of the oscillators and the horizontal axis shows the time evolution. (a) Coherent state. (b)(c) Transitions between coherent state and partially synchronized states. (d) Partially synchronized state. (e) Transitions between partially synchronized state and modulated state. (f) Modulated state. (g)(h) The degree of incoherence increases and finally reaches a complete incoherent state. Figures are reprinted from [85].

by

$$\frac{dz_\sigma^*}{dt} = -(\Delta_\sigma + i\Omega_\sigma)z_\sigma^* + \sum_{\tau=1}^{M} \frac{K_{\sigma\tau}}{2}\left[e^{i\alpha_{\sigma\tau}}z_\tau^* - e^{-i\alpha_{\sigma\tau}}z_\tau(z_\sigma^*)^2\right], \tag{5.2}$$

where Ω_σ and Δ_σ represent the center and width of the Lorentzian distribution of natural frequencies within the population, respectively. This can be further expressed in polar coordinates, defined as $z_\sigma = r_\sigma e^{-i\phi_\sigma}$, and is given by

$$\frac{dr_\sigma}{dt} = -\Delta_\sigma r_\sigma + \frac{1-r_\sigma^2}{2}\sum_{\tau=1}^{M} K_{\sigma\tau}r_\tau\cos(\alpha_{\sigma\tau} + \phi_\tau - \phi_\sigma), \tag{5.3}$$

$$\frac{d\phi_\sigma}{dt} = -\Omega_\sigma + \frac{1+r_\sigma^2}{2r_\sigma}\sum_{\tau=1}^{M} K_{\sigma\tau}r_\tau\sin(\alpha_{\sigma\tau} + \phi_\tau - \phi_\sigma), \tag{5.4}$$

where r_σ and ϕ_σ are the radial and angular components of the order parameter, respectively. The two-population version of this equation has been explored in previous studies [2, 97]. We consider the case where each oscillator population is placed on a ring. If there are M populations, there are $M+1$ trivial solutions: (a) M coherent solutions where all r_σ are identical,

$$r_\sigma = r, \tag{5.5}$$

$$\phi_\sigma(t) = \phi_\sigma(0) + \omega t, \tag{5.6}$$

$$\phi_\sigma(0) = \phi_1(0) + \frac{2\pi q}{M}(\sigma - 1), \tag{5.7}$$

where q is an integer winding number. For simplicity, we assume M is even, in which case q can take M different values $q = -\frac{M}{2}, -\frac{M}{2}+1, \ldots, -1, 0, 1, \ldots, \frac{M}{2}-1$. The case $q = 0$ corresponds to a phase-synchronized state, while $q \neq 0$ corresponds to a twisted state. We employ a top-hat function as the coupling scheme, where $K_{\sigma\tau} = K$ within the coupling range R, and $K_{\sigma\tau} = 0$ otherwise. We assume identical phase lags and natural frequency distributions $\alpha_{\sigma\tau} = \alpha, \Delta_\sigma = \Delta$, and $\Omega_\sigma = 0$. Under this setup, the solutions can be expressed as

$$r = \sqrt{1 - \frac{2\Delta}{Kh(q;R,M)\cos\alpha}}, \tag{5.8}$$

$$\omega = Kh(q;R,M)\sin\alpha - \Delta\tan\alpha, \tag{5.9}$$

where

$$h(q;R,M)=\begin{cases}2R+1 & \text{if } q=0,\\ \frac{\sin\frac{\pi q(2R+1)}{M}}{\sin\frac{\pi q}{M}} & \text{if } q\neq 0.\end{cases} \tag{5.10}$$

(b) 1 incoherent solution, where $r_\sigma = 0$. Additionally, there are many non-trivial solutions that cannot be expressed explicitly.

As we saw in Section 1.2, in the non-local Kuramoto-Sakaguchi phase oscillator model, when the phase lag α is sufficiently smaller than $\pi/2$, the system is attracted to a coherent steady state. However, as α approaches $\pi/2$, a chimera state emerges, where the oscillators are spatially split into coherent and incoherent groups. In the OA-reduced M-population KS model, a similar situation arises when α is much smaller than $\pi/2$, and the system enters a coherent steady state (i.e., the trivial solution Eq. (5.5)(5.6)(5.7) or the non-trivial solutions described in the next section). However, as α approaches $\pi/2$, the system exhibits significantly different behavior due to the influence of the amplitude r.

5.2 Spatiotemporal pattern

The following numerical results were obtained for the parameters $M = 1000$, $R = 40$, $\Delta = 0.01$, and $K = 0.045$. Time integration was performed using the fourth-order Runge-Kutta method with a time step of 0.01. Figure 5.1 shows the spatiotemporal patterns of $r_\sigma(t)$ for different values of α. In Figure 5.1(a), for smaller values of α, starting from random initial conditions, the system directly enters a coherent state (either fully synchronized or twisted state). In Figures (b) and (c), we observe that the system exhibits metastable behavior: in the red regions, the amplitude r_σ of the oscillators is almost equal and very close to the coherent solution given by Eq. (B.3), while during other time intervals, the oscillators are only partially synchronized. Here, the partially synchronized state refers to a scenario where different populations exhibit varying degrees of synchrony (r_σ), and both r_σ and ϕ_σ show a disordered spatial arrangement. As the parameter α increases, the proportion of time that the system spends in the partially synchronized state grows, until only the partially synchronized state remains (Figure 5.1(d)). With further increases in α, the system displays another form of metastable behavior, switching between the partially synchronized state and the modulated state (Figure 5.1(e)). In the modulated state, the system exhibits spatially structured synchrony, where consecutive populations with $r_\sigma \approx r$ alternate with

populations where $r \approx 0$. This arrangement forms a unique pattern of alternating synchronized and unsynchronized populations, which we refer to as the modulated state. The characteristic width of this spatial periodic arrangement increases as the coupling range R increases. Finally, when α approaches very close to 0.5π, this metastable behavior disappears once again, and the system becomes completely disordered, where all $r_\sigma = 0$ (Figure 5.1(h)).

5.3 Traveling wave solutions

For smaller values of α, the system reaches a trivial coherent state described by Eq. (5.5)-(5.7). Depending on the initial conditions, the system will settle into a stable coherent state with a specific value of q. However, as α increases, the system transitions to a non-trivial steady state. These non-trivial solutions have values close to the coherent solutions but exhibit non-uniform spatial distributions and propagate at a constant speed, as shown in Figures 5.2(a) and (b). We use the phase difference $\psi_\sigma = \phi_{\sigma+1} - \phi_\sigma$ instead of the phase variable ϕ_σ to represent the system's state more intuitively. If the sign of the parameter q is reversed, the direction of wave propagation will also reverse. For different values of q, the system exhibits different α thresholds, beyond which the traveling wave state emerges. This is illustrated in Figure 5.2(c), where the standard deviation of r_σ is used as an indicator. Once this threshold is surpassed, further increases in α lead to an increase in wave amplitude.

How do the system's parameters affect the coherent state? We conducted a linear stability analysis of the coherent state. We introduced small perturbations δr_σ and ψ_σ to each oscillator's r and ϕ, and obtained $2M$ eigenvalues λ_m (see Appendix B). The eigenvalues λ_m are functions of Δ, α, K, h. For convenience, we define $A = Kh$, as it represents the product of coupling strength and coupling distance, making it intuitive that a larger A would more likely lead to synchronization in the system.

The linear stability ranges of different coherent states under various parameter conditions as α varies are shown in Figure 5.3. In the black regions, $2M - 1$ eigenvalues have negative real parts, with only one eigenvalue having a zero real part. In the yellow regions, at least one eigenvalue has a positive real part. Figure (a) shows the case with fixed Δ. Small A and large α cause the coherent state to become unstable, which is consistent with empirical knowledge. Figure (b) shows the case with fixed A. When Δ exceeds a certain threshold, the coherent state becomes unstable. From Eq. B.3, a threshold $\Delta < Kh/2$ can be calculated, but the actual linear stability range is

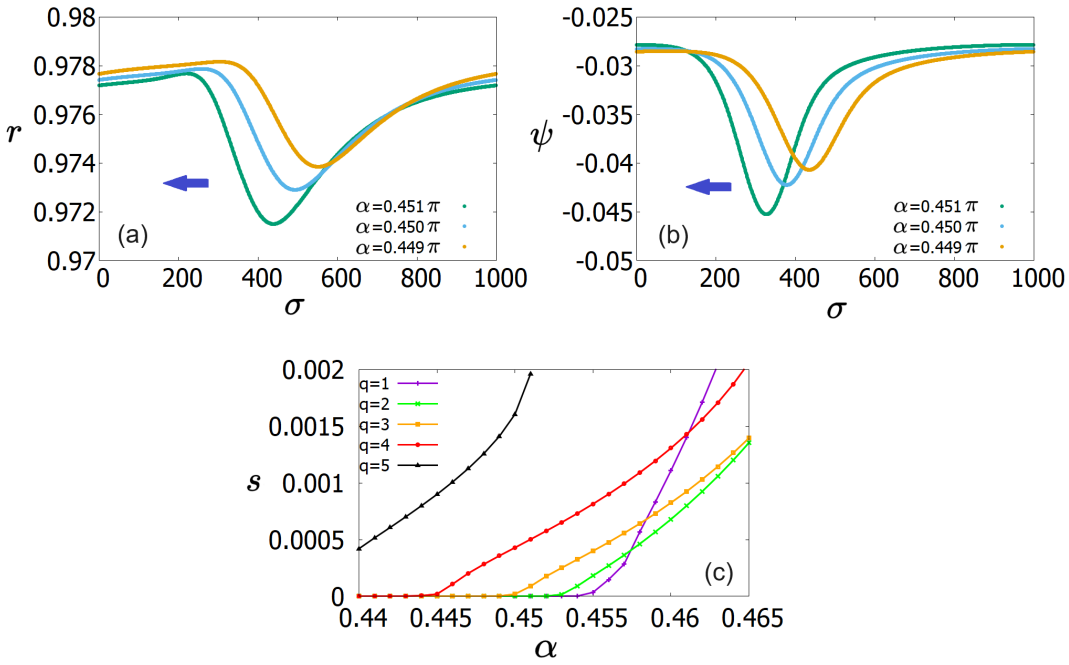

FIGURE 5.2: Traveling wave solutions with $q = -5$ for $\alpha = 0.449\pi, 0.450\pi, 0.451\pi$. (a) The amplitude and (b) phase difference between nearest neighbors. The arrow shows the traveling direction of the wave. (c) Standard deviation s of the amplitude. For $s = 0$, the system is in a trivial coherent state. For $s > 0$, the system exhibits a traveling wave. The threshold varies for different q. Figures are reprinted from [85].

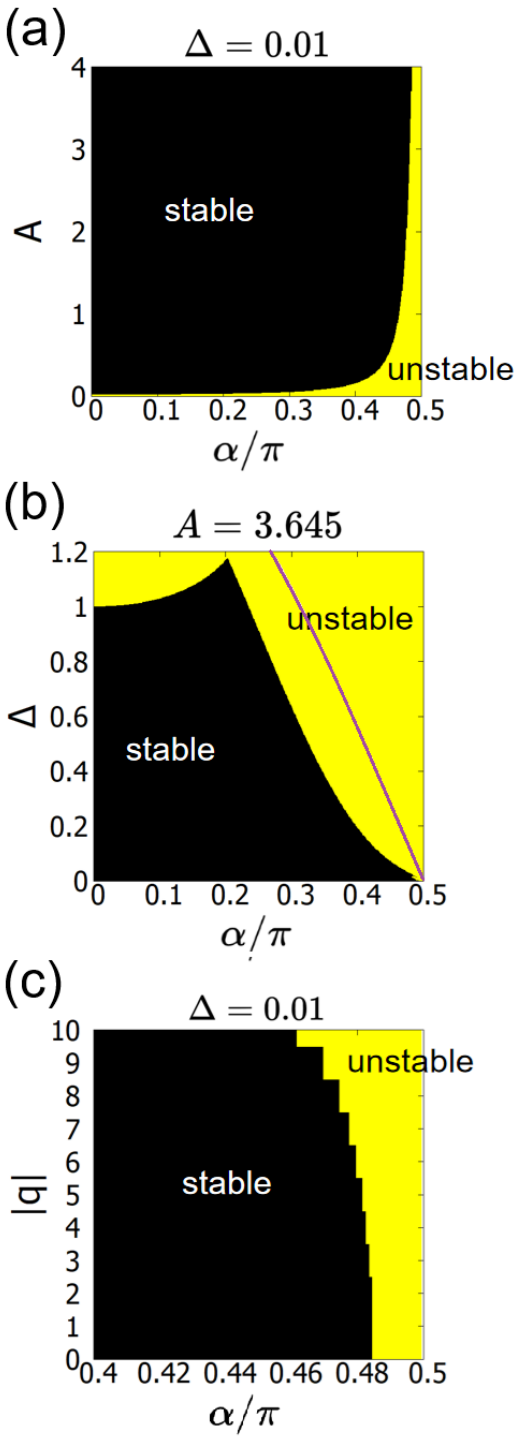

FIGURE 5.3: Linear stability diagram of the coherent state with $|q| = 0, 1, \ldots, 10$. The black area shows the parameter range where the coherent state is neutrally stable. The yellow area shows where the coherent state is unstable. Figures are reprinted from [85].

smaller. Figure (c) shows the case with fixed Δ, where it is evident that the stability range of the coherent state decreases as q increases.

It is worth noting that within the parameter range where the system exhibits traveling wave solutions, the coherent solution is also linearly stable. However, extensive simulations show that even if both solutions are stable, all initial conditions eventually converge to the traveling wave solution. This suggests that the traveling wave solution has a larger basin of attraction compared to the coherent solution with the same q value.

5.4 Metastability

As mentioned earlier, before reaching a steady state, the system transitions between different metastable states in a certain range of α. Figure 5.4 shows an example with $\alpha = 0.458\pi$. During the first 5000 time units, the system enters and exits the coherent state four times. In these coherent states, the spatially averaged amplitude of the oscillators is close to the value given by Eq.(B.3), and the average phase difference $\overline{\psi}$ remains constant throughout each metastable period (see Figure5.4(d)). We can determine how many transitions the system undergoes by counting the number of continuous segments where $\overline{\psi}$ remains unchanged. In the example shown in Figure 5.4, the system undergoes dozens of such transitions before finally stabilizing.

The lifetimes of the stable coherent states that the system reaches under different values of α, as well as the number of transitions between different coherent states during this process, are shown in Figure 5.5. As α increases, the lifetime of the transition process exhibits exponential growth. It can be observed that when α exceeds 0.46π, there are no lifetimes shorter than 500,000 time units. Additionally, for $\alpha > 0.46\pi$, the number of transitions begins to decrease. This is because fluctuations in the system start to dominate, leading to a weakened attraction towards the coherent states. Around $\alpha = 0.46\pi$, the system exhibits the strongest metastability.

For $0.485\pi < \alpha < 0.495\pi$, the system shows a novel state we call the modulated state. This state is characterized by a spatially periodic modulation of the amplitude of the oscillators. The system again displays metastable behavior between the partially synchronized state and modulated state (Fig. 5.1(e)). We define the variance of the amplitude

$$\chi = \langle V \rangle_T , \tag{5.11}$$

$$V(t) = \frac{1}{M} \sum_{\sigma=1}^{M} \left(r_\sigma(t) - \langle r_\sigma(t) \rangle \right)^2 , \tag{5.12}$$

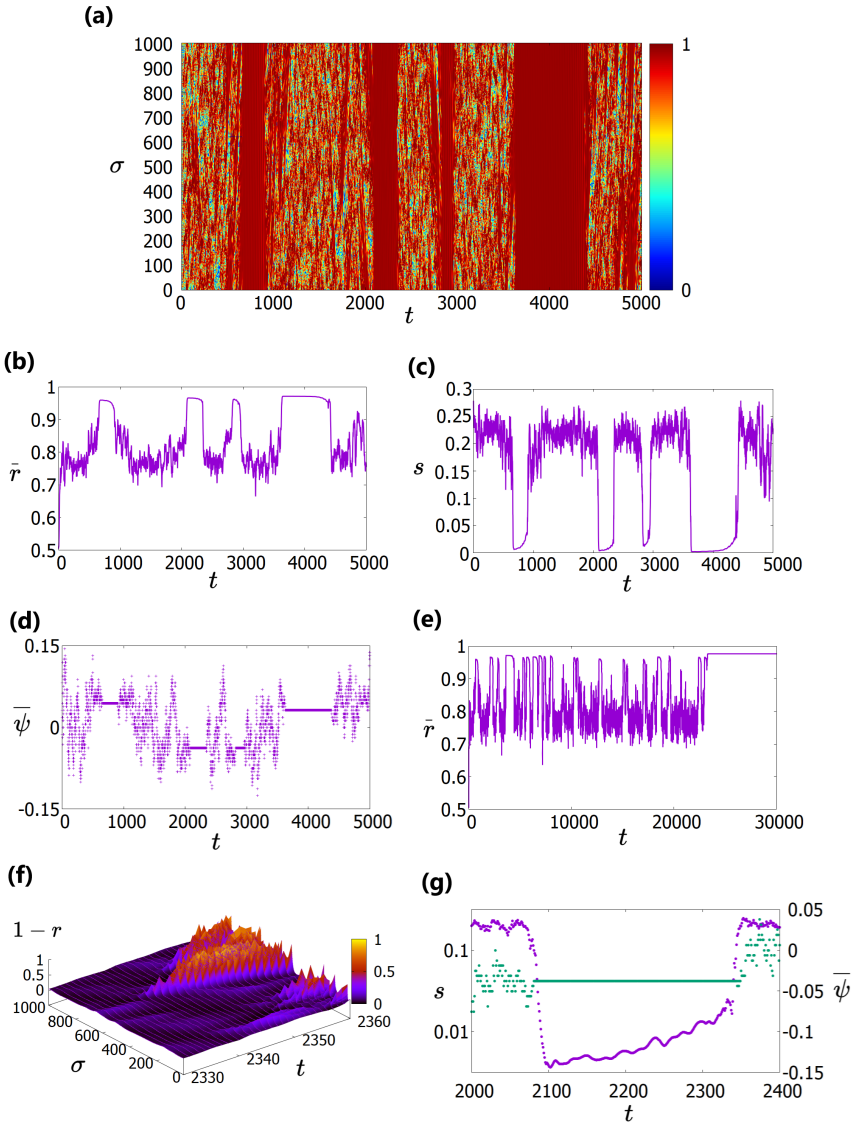

FIGURE 5.4: Transition between coherent and partially synchronized states for $\alpha = 0.458\pi$. (a) Spatiotemporal pattern of r_σ. In the time window $t \in [0, 5000]$, the system has experienced 4 coherent states: [656,904], [2081,2344], [2817,2956], [3622,4381]. Time evolution of the (b) spatially averaged amplitude $\bar{r}(t)$ and (c) standard deviation of amplitude s for $t < 5000$. (d) Time evolution of the average phase difference of neighbor oscillators $\overline{\psi}(t)$. It is constant in the coherent state and the corresponding twist number is $q = \overline{\psi}M/2\pi$. In this example, the 4 coherent states are $q =$ 7,6,6,5 respectively. (e) $\bar{r}(t)$ on a longer timescale. The system eventually enters a stable coherent state at $t \approx 23260$. (f) Spatiotemporal pattern of $1r_\sigma$ in the time window [2330:2360] showing the collapse of the coherent state. (g) Time evolution of the standard deviation of the amplitude s (logscale, purple) and the average phase difference ψ (green) in the time window [2000,2400] showing the transitions between the incoherent and coherent states. Figures are reprinted from [85].

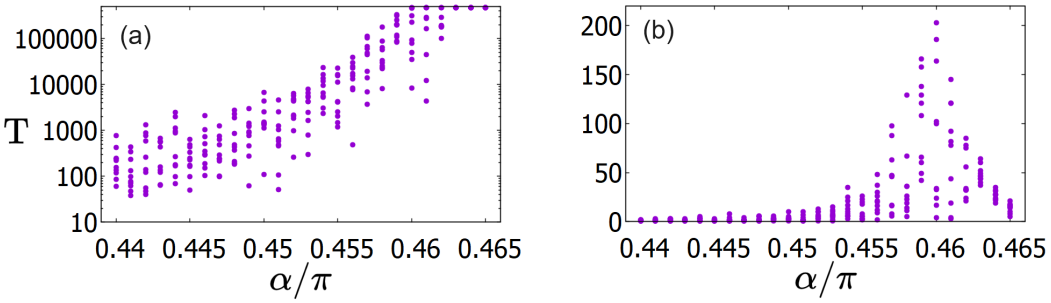

FIGURE 5.5: For each α, 10 different initial conditions were taken, and the simulations were run up to $t = 500000$. (a) The lifetime of the transition process. (b) The number of coherent states system goes through within 500000 time units. We define that if $\overline{\psi}(t)$ remains constant for more than 25 time units, the system is considered to have entered a coherent state. This choice of threshold does not qualitatively change the result. Figures are reprinted from [85].

where $\langle V \rangle_T$ means the time average, to characterize these different states (it was also used in the previous study [139] to evaluate the degree of chimera behavior in the system). Fig. 5.6 shows the dependence of χ on α. Time average is taken over $0 \geq t \geq 5000$, and 30 trials with different initial conditions for each value of α are shown. When $\alpha < \alpha_1 \approx 0.44\pi$, the system rapidly settles into a stable coherent state with a constant r, and hence the variance of r is almost zero. When $\alpha_1 < \alpha < \alpha_2 \approx 0.465\pi$, the system exhibits metastable behavior, transitioning back and forth between coherent and partially synchronized state (Fig. 5.4(b)), leading to an increase in χ as the proportion of time spent in the partially synchronized state grows. When $\alpha_2 < \alpha < \alpha_3 \approx 0.485\pi$, the system enters a persistent partially synchronized state, and the slow increase in χ is due to the increasing amplitude dispersion within the partially synchronized state. When $\alpha_3 < \alpha < \alpha_4 \approx 0.495\pi$, the system exhibits either a modulated state or metastable behavior between the modulated and partially synchronized states. In the latter case, χ is larger than the partially synchronized state since the modulated state has a larger dispersion of r. This explains the branching behavior of χ. Finally, when $\alpha_4 < \alpha \leq 0.5\pi$, the amplitudes of all oscillators gradually decrease to zero.

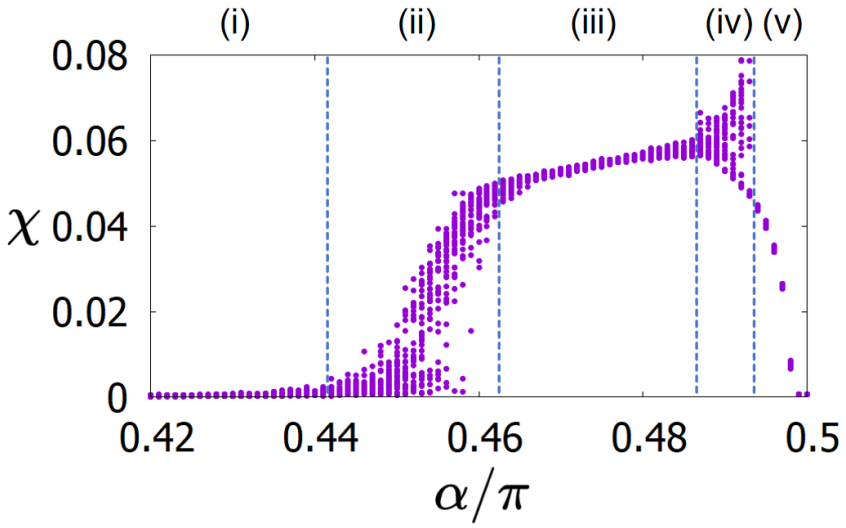

FIGURE 5.6: Time average of the spatial variance of the amplitude χ. Different states of the system are characterized by χ. The dotted lines show α_1, α_2, α_3 and α_4. (i) $0 \leq \alpha < \alpha_1$: coherent state. (ii) $\alpha_1 < \alpha < \alpha_2$: metastable transition between coherent state and partially synchronized state. (iii)$\alpha_2 < \alpha < \alpha_3$: partially synchronized state. (iv)$\alpha_3 < \alpha < \alpha_4$: metastable transition between partially synchronized state and modulated state. (v)$\alpha_4 \leq \alpha < 0.5$: incoherent state. Figures are reprinted from [85].

5.5 Conclusion

We studied the Ott-Antonsen-reduced M-population Kuramoto-Sakaguchi oscillator model and discovered a rich variety of dynamical behaviors by varying the phase lag parameter α. Unlike the ordinary KS phase oscillator model [30, 68, 84, 91], which typically only shows the coexistence of synchronized and unsynchronized states, we found that this system exhibits new metastable behaviors. In this system, the amplitude variable r plays a crucial role, making the phase space of the system extremely complex, which in turn leads to the emergence of new attractors in the form of traveling waves. Unlike other amplitude-related behaviors, such as amplitude chimeras [173, 174], this system continuously transitions between different states. It remains for some time on a trajectory close to the coherent state attractor (without entering its basin of attraction) and then deviates at certain moments to partially synchronize for a period, before once again approaching the vicinity of the coherent state. The transitions between these metastable states are not driven by external disturbances or noise but are instead triggered by the inherent complex structure of the phase space in this high-dimensional nonlinear system. This metastability is attributed to the inhomogeneity Δ within the populations (with Δ set to 0, the mean-field behavior of the population is equivalent to that of the original KS phase oscillator).

Metastability, which is the coexistence of segregated and integrated neural dynamics, is considered a hallmark of brain activity in neuroscience [157]. Key brain functions are thought to be encoded by the coexistence of segregation (where neuron assemblies tend to differentiate and operate independently) and integration (where neuron assemblies tend to synchronize). Furthermore, recent studies have found a connection between the value of α and the ratio of electrical and chemical synapses in the brain [24]. By extending the OA-reduced M-population KS model to the brain network, we can link the microscopic and macroscopic descriptions and capture the microscopic properties of the underlying neuronal system. Given that this model exhibits both the association with synaptic properties and metastable behavior, it is a promising candidate for brain network modeling.

Chapter 6

Conclusion

This dissertation presents a comprehensive exploration of the effects of frustration induced by nonlocal coupling with a phase delay on the collective dynamics of coupled phase oscillators. Through three interconnected studies, I have sought to address the broader question of how complex synchronization patterns and chimera states emerge in systems where oscillators (i) interact repulsively, (ii) have mobility, or (iii) have a hierarchical network structure. The underlying goal was to investigate the mechanisms that lead to partial synchronization, desynchronization, and metastable dynamics, and to determine how these mechanisms apply to both physical systems and biological networks, particularly in neuroscience.

1. Nonlocally Coupled Oscillators with Repulsive Coupling

   The first study investigated the dynamics of nonlocally coupled oscillators with repulsive interactions, a less explored area compared to attractive coupling. Oscillators arranged on a one-dimensional ring were coupled nonlocally with a phase lag parameter α, introducing frustration. The study aimed to understand how repulsive coupling shapes synchronization and phase transitions, revealing the emergence of chimera states—coexisting coherent (twisted) and incoherent regions.

   Through spatiotemporal plots and linear stability analysis, the conditions for twisted state stability were identified. Increasing α drove transitions from incoherent states to chimera states and eventually to a phase dominated by coherent twisted states. Comparisons with Z2-symmetric directed percolation (DP2) highlighted similarities, including two twisted states analogous to DP2's absorbing states and incoherent regions acting as transient intermediates akin to DP2's active sites. However, the oscillator system differed by exhibiting traveling waves originating from incoherent regions, a feature absent in DP2, due to the continuous nature of phase variables.

The fraction of incoherent regions displayed a power-law decay near the critical transition, with distinct critical exponents compared to DP2. These findings underscore how repulsive coupling and continuous phase dynamics lead to unique behaviors, extending the understanding of universality in coupled systems.

2. Impact of Mobility on Oscillator Synchronization

   The second study explored the role of mobility in nonlocally coupled oscillator systems, extending the investigation into how spatial dynamics influence synchronization and pattern formation. Unlike static systems, where oscillators are fixed in space, this study considered a scenario in which oscillators could move, dynamically altering their coupling neighborhoods. Mobility was introduced as a stochastic process, where oscillators randomly swapped positions within a defined range, adding an additional layer of complexity to the system.

   We first found that mobility destabilizes twisted states with large $|q|$ and enlarges the attraction basin of twisted states with small $|q|$, and the decay of the root mean square of $|q|$ follows a power law. Also, we examine the timescales associated with the randomization and restoration of coherence by analyzing mobility and coupling independently. Through this comparison, we identify the critical mobility threshold at which twisted states become unstable. Moreover, a novel mesh-like spatiotemporal pattern is identified.

   By revealing how mobility enhances interaction dynamics and affects stability, the study provides insights into applications ranging from mobile sensor networks to models of neuronal activity with rewiring capabilities.

3. Hierarchical Oscillator Networks

   The third study investigated the dynamics of hierarchical networks composed of M-populations of phase oscillators. Each population was treated as a distinct unit which followed the Kuramoto-Sakaguchi dynamics. The hierarchical structure gave rise to metastable states, where populations exhibited transient synchronization before transitioning to the partially synchronized state. This metastability is attributed to the inhomogeneity of the intrinsic frequency Δ within the populations. Besides, a non-trivial traveling wave solution was observed in specific parameter regimes.

This study demonstrated that hierarchical coupling introduces new dimensions of complexity to oscillator dynamics, enabling the emergence of metastable behaviors and rich spatiotemporal patterns. These findings are connected to hierarchical structures in the brain, where partial synchronization and metastable dynamics are believed to play key roles in cognitive functions. The model provided a theoretical basis for understanding how hierarchical coupling can regulate transitions between functional states in neural systems.

These three studies are unified by a central question: how does frustration shape the emergence of synchronization and desynchronization in coupled oscillator systems? The research aims to identify the mechanisms driving complex dynamical states, such as chimera states and metastability, and to understand their transitions under varying conditions, including coupling functions, mobility, and network structure. While each study focuses on distinct system characteristics, they collectively contribute to a comprehensive understanding of how different factors influence synchronization.

The motivation for this research stems from an interest in brain dynamics, where synchronization and desynchronization are fundamental to cognitive processes. Inspired by these phenomena, the studies explore the conditions under which synchronized and desynchronized states coexist and transition, offering insights into real-world systems like brain networks.

The results demonstrate that frustration is a key factor in forming chimera states, mobility profoundly alters the synchronization landscape, and hierarchical network structures enable metastable dynamics. In conclusion, this dissertation fulfills its goal of exploring the role of frustration in coupled oscillator systems. The insights presented here provide a cohesive framework for understanding complex dynamical behaviors and pave the way for future studies on synchronization in both theoretical and applied contexts.

Appendix A

Ott-Antonsen Reduction of m-population of KS model

Let us consider Kuramoto-Sakaguchi model with m populations of N oscillators,

$$\frac{\mathrm{d}\theta_k^\sigma}{\mathrm{d}t} = \omega_k^\sigma - \sum_{\tau=1}^{m} \frac{K_{\sigma\tau}}{N} \sum_{l=1}^{N} \sin(\theta_k^\sigma - \theta_l^\tau + \alpha), \tag{A.1}$$

where θ_k^σ is the phase of the k-th oscillator of popluation σ.

Considering the thermodynamic limit where $N \to \infty$, the order parameter for each population can be defined as

$$z_\sigma(t) = \int_{-\infty}^{\infty} \int_0^{2\pi} f_\sigma(\omega^\sigma, \theta^\sigma, t) e^{i\theta^\sigma} \mathrm{d}\theta^\sigma \mathrm{d}\omega^\sigma, \tag{A.2}$$

where $f_\sigma(\omega^\sigma, \theta^\sigma, t)$ is the probability density of oscillators in population σ, obeying the continuity equation

$$\frac{\partial f_\sigma}{\partial t} + \frac{\partial}{\partial \theta^\sigma}(f_\sigma v_\sigma) = 0, \tag{A.3}$$

where $v_\sigma(\omega^\sigma, \theta^\sigma, t)$ is their velocity, given by

$$\begin{aligned}
v_\sigma &= \omega^\sigma - \sum_{\tau=1}^{m} K_{\sigma\tau} \int_{-\infty}^{\infty} \int_0^{2\pi} f_\tau(\omega^\tau, \theta^\tau, t) \sin(\theta^\sigma - \theta^\tau + \alpha_{\sigma\tau}) \mathrm{d}\theta^\tau \mathrm{d}\omega^\tau \\
&= \omega^\sigma - \sum_{\tau=1}^{m} K_{\sigma\tau} \mathrm{Im} \left[\int_{-\infty}^{\infty} \int_0^{2\pi} f_\tau(\omega^\tau, \theta^\tau, t) e^{i(\theta^\sigma - \theta^\tau + \alpha_{\sigma\tau})} \mathrm{d}\theta^\tau \mathrm{d}\omega^\tau \right] \\
&= \omega^\sigma - \sum_{\tau=1}^{m} K_{\sigma\tau} \mathrm{Im} \left[e^{i(\theta^\sigma + \alpha_{\sigma\tau})} z_\tau^*(t) \right] \\
&= \omega^\sigma - \sum_{\tau=1}^{m} \frac{K_{\sigma\tau}}{2i} \left[e^{i(\theta^\sigma + \alpha_{\sigma\tau})} z_\tau^*(t) - e^{-i(\theta^\sigma + \alpha_{\sigma\tau})} z_\tau(t) \right].
\end{aligned} \tag{A.4}$$

Using the Ott-Antonsen ansatz [115], $f_\sigma(\omega^\sigma, \theta^\sigma, t)$ can be expanded to a Fourier series of θ with a set of specific coefficients $f_{\sigma,n}(\omega^\sigma, t) = [a(\omega^\sigma, t)]^n$,

$$f_\sigma(\omega^\sigma, \theta^\sigma, t) = \frac{g_\sigma(\omega^\sigma)}{2\pi}\left\{1 + \sum_{n=1}^{\infty}[a_\sigma(\omega^\sigma, t)]^n e^{in\theta^\sigma} + c.c.\right\}. \tag{A.5}$$

Putting Eq. (A.5) into Eq. (A.2), so that $z_\sigma(t)$ can be written as a function of a,

$$\begin{aligned} z_\sigma(t) &= \int_{-\infty}^{\infty}\int_0^{2\pi}\frac{g_\sigma(\omega^\sigma)}{2\pi}\left\{1 + \sum_{n=1}^{\infty}[a_\sigma(\omega^\sigma, t)]^n e^{in\theta^\sigma} + c.c.\right\} e^{i\theta^\sigma}\mathrm{d}\theta^\sigma\mathrm{d}\omega^\sigma \\ &= \int_{-\infty}^{\infty}\int_0^{2\pi}\frac{g_\sigma(\omega^\sigma)}{2\pi}[a_\sigma(\omega^\sigma, t)]^*\mathrm{d}\theta^\sigma\mathrm{d}\omega^\sigma \\ &= \int_{-\infty}^{\infty} g_\sigma(\omega^\sigma)[a_\sigma(\omega^\sigma, t)]^*\mathrm{d}\omega^\sigma. \end{aligned} \tag{A.6}$$

Putting Eq. (A.5) into Eq. (A.3),

$$\begin{aligned} 0 &= \frac{\partial f_\sigma}{\partial t} + \frac{\partial}{\partial\theta^\sigma}(f_\sigma v_\sigma) \\ &= \frac{g_\sigma(\omega^\sigma)}{2\pi}\left\{\sum_{n=1}^{\infty}\left[n a_\sigma^{n-1}\frac{\partial a_\sigma}{\partial t}e^{in\theta^\sigma} + n(a_\sigma^*)^{n-1}\frac{\partial a_\sigma^*}{\partial t}e^{-in\theta^\sigma}\right]\right\} \\ &\quad + \frac{g_\sigma(\omega^\sigma)}{2\pi}\sum_{n=1}^{\infty}\left[ina_\sigma^n e^{in\theta^\sigma} - in(a_\sigma^*)^n e^{-in\theta^\sigma}\right] \\ &\quad \times\left\{\omega^\sigma - \sum_{\tau=1}^{m}\frac{K_{\sigma\tau}}{2i}\left[e^{i(\theta^\sigma+\alpha_{\sigma\tau})}z_\tau^* - e^{-i(\theta^\sigma+\alpha_{\sigma\tau})}z_\tau\right]\right\} \\ &\quad + \frac{g_\sigma(\omega^\sigma)}{2\pi}\left\{1 + \sum_{n=1}^{\infty}[a_\sigma^n e^{in\theta^\sigma} + (a_\sigma^*)^n e^{-in\theta^\sigma}]\right\} \\ &\quad \times\left\{-\sum_{\tau=1}^{m}\frac{K_{\sigma\tau}}{2i}\left[ie^{i(\theta^\sigma+\alpha_{\sigma\tau})}z_\tau^* + ie^{-i(\theta^\sigma+\alpha_{\sigma\tau})}z_\tau\right]\right\}. \end{aligned} \tag{A.7}$$

Extract the coefficients of the 1st-order term $e^{i\theta^\sigma}$,

$$\begin{aligned} 0 &= \frac{\partial a_\sigma}{\partial t}e^{i\theta^\sigma} + i\omega^\sigma a_\sigma e^{i\theta^\sigma} + \sum_{\tau=1}^{m}K_{\sigma\tau}a_\sigma^2 e^{i(\theta^\sigma-\alpha_{\sigma\tau})}z_\tau \\ &\quad - \sum_{\tau=1}^{m}\frac{K_{\sigma\tau}}{2}\left[e^{i(\theta^\sigma+\alpha_{\sigma\tau})}z_\tau^* + a_\sigma^2 e^{i(\theta^\sigma-\alpha_{\sigma\tau})}z_\tau\right], \\ \frac{\partial a_\sigma}{\partial t} &= -i\omega^\sigma a_\sigma + \sum_{\tau=1}^{m}\frac{K_{\sigma\tau}}{2}\left[e^{i\alpha_{\sigma\tau}}z_\tau^* - a_\sigma^2 e^{-i\alpha_{\sigma\tau}}z_\tau\right]. \end{aligned} \tag{A.8}$$

By choosing a Lorentzian distribution with center Ω_σ and width Δ_σ,

$$\begin{aligned} g_\sigma(\omega^\sigma) &= \frac{1}{\pi}\frac{\Delta_\sigma}{(\omega^\sigma-\Omega_\sigma)^2+\Delta_\sigma^2} \\ &= \frac{1}{2\pi i}\left[\frac{1}{\omega^\sigma-\Omega_\sigma-i\Delta_\sigma}-\frac{1}{\omega^\sigma-\Omega_\sigma+i\Delta_\sigma}\right], \end{aligned} \tag{A.9}$$

Eq. A.6 can be calculated by closing the contour by a large semicircle in the lower half ω^σ-plane, where the integral is given by the residue of the pole at $\omega^\sigma = \Omega_\sigma - i\Delta_\sigma$,

$$\begin{aligned} z_\sigma(t) &= \int_{-\infty}^{\infty} g_\sigma(\omega^\sigma)[a_\sigma(\omega^\sigma,t)]^* \mathrm{d}\omega^\sigma \\ &= \frac{1}{2\pi i}\int_{-\infty}^{\infty}\left\{\frac{[a_\sigma(\omega^\sigma,t)]^*}{\omega^\sigma-\Omega_\sigma-i\Delta_\sigma}-\frac{[a_\sigma(\omega^\sigma,t)]^*}{\omega^\sigma-\Omega_\sigma+i\Delta_\sigma}\right\}\mathrm{d}\omega^\sigma \\ &= -\mathrm{Res}\left(\frac{[a_\sigma(\omega^\sigma,t)]^*}{\omega^\sigma-\Omega_\sigma+i\Delta_\sigma}, \omega^\sigma=\Omega_\sigma-i\Delta_\sigma\right) \\ &= [a_\sigma(\Omega_\sigma-i\Delta_\sigma,t)]^*. \end{aligned} \tag{A.10}$$

Finally, using Eq. A.8, the dynamics of the order parameter $z_\sigma(t)$ can be represented as follow,

$$\frac{\mathrm{d}z_\sigma^*}{\mathrm{d}t} = -(\Delta_\sigma+i\Omega_\sigma)z_\sigma^* + \sum_{\tau=1}^{m}\frac{K_{\sigma\tau}}{2}\left[e^{i\alpha_{\sigma\tau}}z_\tau^* - e^{-i\alpha_{\sigma\tau}}z_\tau(z_\sigma^*)^2\right]. \tag{A.11}$$

Then we can rewrite these equations in polar coordinates $z_\sigma = r_\sigma e^{-i\phi_\sigma}$ where r and ϕ are the radial and angular components of order parameter respectively.

$$\begin{aligned} \frac{\mathrm{d}}{\mathrm{d}t}(r_\sigma e^{i\phi_\sigma}) &= -(\Delta_\sigma+i\Omega_\sigma)r_\sigma e^{i\phi_\sigma} \\ &+ \sum_{\tau=1}^{m}\frac{K_{\sigma\tau}}{2}\left[r_\tau e^{i(\alpha_{\sigma\tau}+\phi_\tau)} - r_\tau r_\sigma^2 e^{-i(\alpha_{\sigma\tau}+\phi_\tau-2i\phi_\sigma)}\right], \end{aligned} \tag{A.12}$$

$$\mathrm{Re(LHS)} = \frac{\mathrm{d}r_\sigma}{\mathrm{d}t}\cos\phi_\sigma - r_\sigma\sin\phi_\sigma\frac{\mathrm{d}\phi_\sigma}{\mathrm{d}t}, \tag{A.13}$$

$$\mathrm{Im(LHS)} = \frac{\mathrm{d}r_\sigma}{\mathrm{d}t}\sin\phi_\sigma + r_\sigma\cos\phi_\sigma\frac{\mathrm{d}\phi_\sigma}{\mathrm{d}t}, \tag{A.14}$$

$$\begin{aligned}
\mathrm{Re}(\mathrm{RHS}) &= \Omega_\sigma r_\sigma \sin\phi_\sigma - \Delta_\sigma r_\sigma \cos\phi_\sigma \\
&+ \sum_{\tau=1}^{m} \frac{K_{\sigma\tau}}{2}\left[r_\tau \cos(\alpha_{\sigma\tau}+\phi_\tau) - r_\tau r_\sigma^2 \cos(\alpha_{\sigma\tau}+\phi_\tau-2\phi_\sigma)\right], \quad \text{(A.15)} \\
\mathrm{Im}(\mathrm{RHS}) &= -\Omega_\sigma r_\sigma \cos\phi_\sigma - \Delta_\sigma r_\sigma \sin\phi_\sigma \\
&+ \sum_{\tau=1}^{m} \frac{K_{\sigma\tau}}{2}\left[r_\tau \sin(\alpha_{\sigma\tau}+\phi_\tau) + r_\tau r_\sigma^2 \sin(\alpha_{\sigma\tau}+\phi_\tau-2\phi_\sigma)\right], \quad \text{(A.16)}
\end{aligned}$$

Comparing Eq. (A.13) and Eq. (A.14), we get

$$\begin{aligned}
\frac{\mathrm{d}r_\sigma}{\mathrm{d}t} &= \mathrm{Im}(\mathrm{RHS})\sin\phi_\sigma + \mathrm{Re}(\mathrm{RHS})\cos\phi_\sigma, \\
\frac{\mathrm{d}\phi_\sigma}{\mathrm{d}t} &= \frac{1}{r_\sigma}\left[\mathrm{Im}(\mathrm{RHS})\cos\phi_\sigma - \mathrm{Re}(\mathrm{RHS})\sin\phi_\sigma\right],
\end{aligned}$$

So the dynamics of the order parameter of this system can be written as:

$$\begin{aligned}
\frac{\mathrm{d}r_\sigma}{\mathrm{d}t} &= -\Delta_\sigma r_\sigma + \frac{1-r_\sigma^2}{2}\sum_{\tau=1}^{m} K_{\sigma\tau} r_\tau \cos(\alpha_{\sigma\tau}+\phi_\tau-\phi_\sigma), \quad \text{(A.17)} \\
\frac{\mathrm{d}\phi_\sigma}{\mathrm{d}t} &= -\Omega_\sigma + \frac{1+r_\sigma^2}{2r_\sigma}\sum_{\tau=1}^{m} K_{\sigma\tau} r_\tau \sin(\alpha_{\sigma\tau}+\phi_\tau-\phi_\sigma). \quad \text{(A.18)}
\end{aligned}$$

Appendix B

Linear Stability Analysis of m-population OA-KS Model

We apply the linear stability analysis to the m-population OA-KS model. The populations are on a ring with a coupling range R. $K_{\sigma\tau}, \alpha_{\sigma\tau}, \Delta_\sigma$ are set identical, and Ω_σ is set to 0.

$$\frac{\mathrm{d}r_\sigma}{\mathrm{d}t} = -\Delta r_\sigma + \frac{1-r_\sigma^2}{2} K \sum_{\tau=\sigma-R}^{\sigma+R} r_\tau \cos(\alpha + \phi_\tau - \phi_\sigma), \tag{B.1}$$

$$\frac{\mathrm{d}\phi_\sigma}{\mathrm{d}t} = \frac{1+r_\sigma^2}{2r_\sigma} K \sum_{\tau=\sigma-R}^{\sigma+R} r_\tau \sin(\alpha + \phi_\tau - \phi_\sigma). \tag{B.2}$$

One obvious attractor of this system is the synchronization solution:

$$r_\sigma = r, \tag{B.3}$$

$$\phi_\sigma(t) = \phi_\sigma(0) + \omega t, \tag{B.4}$$

$$\phi_\sigma(0) = \phi_1(0) + \frac{2\pi q}{M}(\sigma - 1), \tag{B.5}$$

where q is the twist number. The constant value r can be calculated as follows:

$$0 = -\Delta r + \frac{1-r^2}{2} K r \sum_{\tau=\sigma-R}^{\sigma+R} \cos(\alpha + \phi_\tau - \phi_\sigma). \tag{B.6}$$

Considering that $\phi_\tau - \phi_\sigma = (\tau - \sigma)\frac{2\pi q}{M}$, and let $n = \tau - \sigma$, we can easily get

$$r = \sqrt{1 - \frac{2\Delta}{K\sum_{n=-R}^{R}\cos\left(\alpha + \frac{2\pi q}{M}n\right)}}, \tag{B.7}$$

$$\omega = \frac{1+r^2}{2}K\sum_{n=-R}^{R}\sin\left(\alpha + \frac{2\pi q}{M}n\right). \tag{B.8}$$

For synchronous state ($q = 0$),

$$r = \sqrt{1 - \frac{2\Delta}{K(2R+1)\cos\alpha}}, \tag{B.9}$$

$$\begin{aligned}\omega &= \frac{1+r^2}{2}K(2R+1)\sin\alpha \\ &= \left[K(2R+1) - \frac{\Delta}{\cos\alpha}\right]\sin\alpha,\end{aligned} \tag{B.10}$$

For twisted states ($q \neq 0$), the summation term can also be written in a simple form:

$$\sum_{n=-R}^{R}\cos\left(\alpha + \frac{2\pi q}{M}n\right) = h(q;R,M)\cos\alpha, \tag{B.11}$$

$$\sum_{n=-R}^{R}\sin\left(\alpha + \frac{2\pi q}{M}n\right) = h(q;R,M)\sin\alpha \tag{B.12}$$

$$h(q;R,M) = \begin{cases} 2R+1 & \text{if } q = 0 \\ \frac{\sin\frac{\pi q(2R+1)}{M}}{\sin\frac{\pi q}{M}} & \text{if } q \neq 0 \end{cases}. \tag{B.13}$$

Thus,

$$r = \sqrt{1 - \frac{2\Delta}{Kh(q;R,M)\cos\alpha}}, \tag{B.14}$$

$$\begin{aligned}\omega &= \frac{1+r^2}{2}Kh(q;R,M)\sin\alpha \\ &= \left(Kh(q;R,M) - \frac{\Delta}{\cos\alpha}\right)\sin\alpha.\end{aligned} \tag{B.15}$$

Notice that $h(q;R,M)$ is always smaller than $2R+1$, so for $\alpha < 0.5\pi$, the twisted states have a smaller r than the synchronous state.

Substituting $r^* + \delta r$ and $\phi^* + \delta\phi$ into eq. (B.1)(B.2) and linearizing it, We get,

$$\begin{aligned}
f_\sigma &= \frac{\mathrm{d}}{\mathrm{d}t}\delta r_\sigma \\
&= \left(-\Delta - Kr_\sigma \sum_{\tau=\sigma-R}^{\sigma+R} r_\tau \cos(\alpha+\phi_\tau-\phi_\sigma)\right)\delta r_\sigma \\
&+ \frac{1-r_\sigma^2}{2}K \sum_{\tau=\sigma-R}^{\sigma+R} \cos(\alpha+\phi_\tau-\phi_\sigma)\delta r_\tau \\
&+ \frac{1-r_\sigma^2}{2}K \sum_{\tau=\sigma-R}^{\sigma+R} r_\tau \sin(\alpha+\phi_\tau-\phi_\sigma)\delta\phi_\sigma \\
&- \frac{1-r_\sigma^2}{2}K \sum_{\tau=\sigma-R}^{\sigma+R} r_\tau \sin(\alpha+\phi_\tau-\phi_\sigma)\delta\phi_\tau, \qquad \text{(B.16)} \\
g_\sigma &= \frac{\mathrm{d}}{\mathrm{d}t}\delta\phi_\sigma \\
&= \frac{r_\sigma^2-1}{2r_\sigma^2}K \sum_{\tau=\sigma-R}^{\sigma+R} r_\tau \sin(\alpha+\phi_\tau-\phi_\sigma)\delta r_\sigma \\
&+ \frac{1+r_\sigma^2}{2r_\sigma}K \sum_{\tau=\sigma-R}^{\sigma+R} \sin(\alpha+\phi_\tau-\phi_\sigma)\delta r_\tau \\
&- \frac{1+r_\sigma^2}{2r_\sigma}K \sum_{\tau=\sigma-R}^{\sigma+R} r_\tau \cos(\alpha+\phi_\tau-\phi_\sigma)\delta\phi_\sigma \\
&+ \frac{1+r_\sigma^2}{2r_\sigma}K \sum_{\tau=\sigma-R}^{\sigma+R} r_\tau \cos(\alpha+\phi_\tau-\phi_\sigma)\delta\phi_\tau. \qquad \text{(B.17)}
\end{aligned}$$

The Jacobian is

$$J = \begin{pmatrix}
\frac{\partial f_1}{\partial r_1} & \cdots & \frac{\partial f_1}{\partial r_M} & \frac{\partial f_1}{\partial \phi_1} & \cdots & \frac{\partial f_1}{\partial \phi_M} \\
\vdots & \ddots & \vdots & \vdots & \ddots & \vdots \\
\frac{\partial f_M}{\partial r_1} & \cdots & \frac{\partial f_M}{\partial r_M} & \frac{\partial f_M}{\partial \phi_1} & \cdots & \frac{\partial f_M}{\partial \phi_M} \\
\frac{\partial g_1}{\partial r_1} & \cdots & \frac{\partial g_1}{\partial r_M} & \frac{\partial g_1}{\partial \phi_1} & \cdots & \frac{\partial g_1}{\partial \phi_M} \\
\vdots & \ddots & \vdots & \vdots & \ddots & \vdots \\
\frac{\partial g_M}{\partial r_1} & \cdots & \frac{\partial g_M}{\partial r_M} & \frac{\partial g_M}{\partial \phi_1} & \cdots & \frac{\partial g_M}{\partial \phi_M}
\end{pmatrix} \qquad \text{(B.18)}$$

This matrix can be divided into 4 big blocks. In each of the 4 blocks, all diagonal elements are equal, all off-diagonal elements are equal, but the diagonal and off-diagonal elements are different from each other. Let $A = Kh(q; R, M)$ and r is the solution,

$$\begin{aligned}
\frac{\partial f_\sigma}{\partial r_\sigma} &= \Delta - A\cos\alpha \\
\frac{\partial f_\sigma}{\partial r_\tau} &= \Delta \\
\frac{\partial f_\sigma}{\partial \phi_\sigma} &= \Delta r\tan\alpha \\
\frac{\partial f_\sigma}{\partial \phi_\tau} &= -\Delta r\tan\alpha \\
\frac{\partial g_\sigma}{\partial r_\sigma} &= -\frac{\Delta\tan\alpha}{r} \\
\frac{\partial g_\sigma}{\partial r_\tau} &= \frac{\sin\alpha - \Delta\tan\alpha}{r} \\
\frac{\partial g_\sigma}{\partial \phi_\sigma} &= \Delta - 1 \\
\frac{\partial g_\sigma}{\partial \phi_\tau} &= 1 - \Delta
\end{aligned}$$

We can calculate the eigenvalue of this matrix analytically as follows. First, we rearrange it to create a new matrix that contains $n \times n$ small 2×2 blocks, where all diagonal blocks are identical, and all off-diagonal blocks are identical.

$$J = \begin{pmatrix}
\frac{\partial f_\sigma}{\partial r_\sigma} & \frac{\partial f_\sigma}{\partial \phi_\sigma} & \cdots & \frac{\partial f_\sigma}{\partial r_\tau} & \frac{\partial f_\sigma}{\partial \phi_\tau} & \cdots & \frac{\partial f_\sigma}{\partial r_\tau} & \frac{\partial f_\sigma}{\partial \phi_\tau} \\
\frac{\partial g_\sigma}{\partial r_\sigma} & \frac{\partial g_\sigma}{\partial \phi_\sigma} & \cdots & \frac{\partial g_\sigma}{\partial r_\tau} & \frac{\partial g_\sigma}{\partial \phi_\tau} & \cdots & \frac{\partial g_\sigma}{\partial r_\tau} & \frac{\partial g_\sigma}{\partial \phi_\tau} \\
\vdots & \vdots & \ddots & \vdots & \vdots & \ddots & \vdots & \vdots \\
\frac{\partial f_\sigma}{\partial r_\tau} & \frac{\partial f_\sigma}{\partial \phi_\tau} & \cdots & \frac{\partial f_\sigma}{\partial r_\sigma} & \frac{\partial f_\sigma}{\partial \phi_\sigma} & \cdots & \frac{\partial f_\sigma}{\partial r_\tau} & \frac{\partial f_\sigma}{\partial \phi_\tau} \\
\frac{\partial g_\sigma}{\partial r_\tau} & \frac{\partial g_\sigma}{\partial \phi_\tau} & \cdots & \frac{\partial g_\sigma}{\partial r_\sigma} & \frac{\partial g_\sigma}{\partial \phi_\sigma} & \cdots & \frac{\partial g_\sigma}{\partial r_\tau} & \frac{\partial g_\sigma}{\partial \phi_\tau} \\
\vdots & \vdots & \ddots & \vdots & \vdots & \ddots & \vdots & \vdots \\
\frac{\partial f_\sigma}{\partial r_\tau} & \frac{\partial f_\sigma}{\partial \phi_\tau} & \cdots & \frac{\partial f_\sigma}{\partial r_\tau} & \frac{\partial f_\sigma}{\partial \phi_\tau} & \cdots & \frac{\partial f_\sigma}{\partial r_\sigma} & \frac{\partial f_\sigma}{\partial \phi_\sigma} \\
\frac{\partial g_\sigma}{\partial r_\tau} & \frac{\partial g_\sigma}{\partial \phi_\tau} & \cdots & \frac{\partial g_\sigma}{\partial r_\tau} & \frac{\partial g_\sigma}{\partial \phi_\tau} & \cdots & \frac{\partial g_\sigma}{\partial r_\sigma} & \frac{\partial g_\sigma}{\partial \phi_\sigma}
\end{pmatrix} \tag{B.19}$$

Then, according to the Bloch theorem, the eigenvalues of this matrix are the same as the following n small 2×2 matrices.

$$\begin{aligned}
& \begin{pmatrix} \frac{\partial f_\sigma}{\partial r_\sigma} + \frac{\partial f_\sigma}{\partial r_\tau} e^{i\frac{2\pi}{M}m} & \frac{\partial f_\sigma}{\partial \phi_\sigma} + \frac{\partial f_\sigma}{\partial \phi_\tau} e^{i\frac{2\pi}{M}m} \\ \frac{\partial g_\sigma}{\partial r_\sigma} + \frac{\partial g_\sigma}{\partial r_\tau} e^{i\frac{2\pi}{M}m} & \frac{\partial g_\sigma}{\partial \phi_\sigma} + \frac{\partial g_\sigma}{\partial \phi_\tau} e^{i\frac{2\pi}{M}m} \end{pmatrix} \\
= & \begin{pmatrix} \Delta - A\cos\alpha + \Delta e^{i\frac{2\pi}{M}m} & \Delta r\tan\alpha - \Delta r\tan\alpha e^{i\frac{2\pi}{M}m} \\ -\frac{\Delta\tan\alpha}{r} + \frac{\sin\alpha - \Delta\tan\alpha}{r} e^{i\frac{2\pi}{M}m} & \Delta - 1 + (1-\Delta)e^{i\frac{2\pi}{M}m} \end{pmatrix} \\
= & \begin{pmatrix} a_m & b_m \\ c_m & d_m \end{pmatrix}
\end{aligned} \tag{B.20}$$

where $m = 1, 2, \ldots, M$. So the eigenvalues are:

$$\lambda_{m\pm} = \frac{(a+d) \pm \sqrt{(a+d)^2 - 4(ad-bc)}}{2} \tag{B.21}$$

$$\begin{aligned}
a + d &= 2\Delta - A\cos\alpha - 1 + e^{i\frac{2\pi}{M}m} \\
(a+d)^2 &= (2\Delta - 1 - A\cos\alpha)^2 + (4\Delta - 2 - 2A\cos\alpha)e^{i\frac{2\pi}{M}m} + e^{i\frac{4\pi}{M}m} \\
&= (2\Delta - A\cos\alpha)^2 - (4\Delta - 2 - 2A\cos\alpha)\left(1 - e^{i\frac{2\pi}{M}m}\right) - \left(1 - e^{i\frac{4\pi}{M}m}\right) \\
ad &= (\Delta - 1)\left(\Delta - A\cos\alpha + A\cos\alpha e^{i\frac{2\pi}{M}m} - \Delta e^{i\frac{4\pi}{M}m}\right) \\
&= (\Delta - 1)\left[\Delta\left(1 - e^{i\frac{2\pi}{M}m}\right) - A\cos\alpha\left(1 - e^{i\frac{4\pi}{M}m}\right)\right] \\
bc &= -\Delta^2\tan^2\alpha + \Delta\sin\alpha\tan\alpha e^{i\frac{2\pi}{M}m} + (\Delta^2\tan^2\alpha - \Delta\sin\alpha\tan\alpha)e^{i\frac{4\pi}{M}m} \\
&= -\Delta\tan\alpha\left[\sin\alpha\left(1 - e^{i\frac{2\pi}{M}m}\right) + (\Delta\tan\alpha - \sin\alpha)\left(1 - e^{i\frac{4\pi}{M}m}\right)\right]
\end{aligned}$$

Rewrite it as the following form:

$$\lambda_{m\pm} = \frac{C_0 + e^{i\frac{2\pi}{M}m} \pm \sqrt{C_1 + C_2 e^{i\frac{2\pi}{M}m} + C_3 e^{i\frac{4\pi}{M}m}}}{2} \tag{B.22}$$

where

$$\begin{aligned}
C_0 &= 2\Delta - 1 - A\cos\alpha \\
C_1 &= (A\cos\alpha - 1)^2 - 4\Delta^2\tan^2\alpha \\
C_2 &= (A\cos\alpha - 1)(2 - 4\Delta) + 4\Delta\sin\alpha\tan\alpha \\
C_3 &= (2\Delta - 1)^2 + 4(\Delta^2\tan^2\alpha - \Delta\sin\alpha\tan\alpha)
\end{aligned}$$

Then we extract the real part of the eigenvalue. Since the square root term is

$$\begin{aligned} & \sqrt{C_1 + C_2 e^{i\frac{2\pi}{M}m} + C_3 e^{i\frac{4\pi}{M}m}} \\ = & \sqrt{C_1 + C_2\cos\left(\frac{2\pi}{M}m\right) + C_3\cos\left(\frac{4\pi}{M}m\right) + i\left(C_2\sin\left(\frac{2\pi}{M}m\right) + C_3\sin\left(\frac{4\pi}{M}m\right)\right)} \end{aligned}$$

let the real part and imaginary part of the square root term be x and y, and use the formulation

$$\mathrm{Re}(\sqrt{x+iy}) = \begin{cases} 0 & \text{if } x = 0 \\ (x^2+y^2)^{\frac{1}{4}}\cos\left(\frac{1}{2}\tan^{-1}(x,y)\right) & \text{if } x \neq 0 \end{cases}$$

Finally, the real part of eigenvalues are

$$\mathrm{Re}(\lambda_{m\pm}) = \frac{C_0 + \cos\left(\frac{2\pi}{M}m\right) \pm (x^2+y^2)^{\frac{1}{4}}\cos\left(\frac{1}{2}\tan^{-1}(x,y)\right)}{2} \tag{B.23}$$

$$\begin{aligned} x &= C_1 + C_2\cos\left(\frac{2\pi}{M}m\right) + C_3\cos\left(\frac{4\pi}{M}m\right) \\ y &= C_2\sin\left(\frac{2\pi}{M}m\right) + C_3\sin\left(\frac{4\pi}{M}m\right) \end{aligned}$$

Appendix C

Derivation of the KS model from the QIF model:

The original derivation is from Ref. [24]. The QIF model is described by the following equation:

$$\tau \frac{dV_i}{dt} = V_i^2 + \eta_i + \epsilon I_{i,\text{syn}}(t) \tag{C.1}$$

where V_i is the membrane potential of neuron i, τ is the membrane time constant, η_i represents an external current (which can vary for each neuron), and $I_{i,syn}(t)$ contains both chemical and electrical synaptic inputs. The parameter ϵ indicates that the coupling is weak.

To convert the QIF model into the Kuramoto model, the phase resetting curve (PRC) needs to be calculated. The PRC describes how the phase of a neuron changes when it receives a small perturbation. For an isolated QIF neuron (no synaptic input), the membrane potential has the solution:

$$V_i(t) = \sqrt{\eta_i} \tan\left(\frac{t\sqrt{\eta_i}}{\tau} - \frac{\pi}{2}\right) \tag{C.2}$$

with the oscillation frequency:

$$\omega_i = \frac{2\sqrt{\eta_i}}{\tau} \tag{C.3}$$

A phase variable θ_i is defined in the interval $[0, 2\pi)$ as:

$$\theta_i = \omega_i t = 2 \arctan\left(\frac{V_i}{\sqrt{\eta_i}}\right) + \pi \tag{C.4}$$

If a small perturbation δV is applied to the membrane potential, the phase will shift according to the PRC. The resulting PRC for the QIF neuron is:

$$\mathrm{PRC}(\theta_i, \delta V) = 2 \arctan\left(\frac{\delta V}{\sqrt{\eta_i}} - \cot\left(\frac{\theta_i}{2}\right)\right) + \pi - \theta_i \tag{C.5}$$

Next, we can apply the weak coupling approximation, assuming that the perturbation to the membrane potential is small $|\delta V| \ll 1$. In this case, the PRC can be linearized:

$$\mathrm{PRC}(\theta_i, \delta V) \approx Z(\theta_i)\delta V \tag{C.6}$$

where $Z(\theta_i)$ is the phase sensitivity function (or infinitesimal PRC). For the QIF model, the iPRC is:

$$Z(\theta_i) = \frac{1 - \cos(\theta_i)}{\sqrt{\eta_i}} \tag{C.7}$$

Using this result, we can derive the Winfree model for the weakly coupled QIF neurons, which describes the phase dynamics of neuron:

$$\dot{\theta}_i = \omega_i + \frac{\epsilon}{\tau}(1 - \cos\theta_i) \sum_{j=1}^{N} P(\theta_i, \theta_j) \tag{C.8}$$

To further simplify the model, let us assume that the external current η_i has weak heterogeneity and can be written as the average $\overline{\eta}$ plus a small distributed term $\epsilon\chi_i$:

$$\eta_i = \bar{\eta} + \epsilon\chi_i \tag{C.9}$$

Under this assumption, the weak coupling ϵ implies that both the coupling terms and the heterogeneity are small. The authors then use the method of averaging, where the phase θ_i is split into a fast oscillation part Φ and a slow phase drift ϕ_i:

$$\theta_i = \Phi + \phi_i \tag{C.10}$$

After applying the averaging approximation, the slow phase dynamics are governed by:

$$\dot{\phi}_i = \frac{\epsilon}{\tau N} \sum_{j=1}^{N} \Gamma(\phi_j - \phi_i) \tag{C.11}$$

where the interaction function $\Gamma(\phi_j - \phi_i)$ is given by:

$$\Gamma(\phi_j - \phi_i) = \frac{\chi_i}{\sqrt{\bar{\eta}}} + g\sin(\phi_j - \phi_i) + \frac{J}{\pi}(1 - \cos(\phi_j - \phi_i)) \tag{C.12}$$

Through the steps above, we reduce the QIF model to a form resembling the Kuramoto model. The final equation for the Kuramoto model is:

$$\dot{\theta}_i = \omega_i + \frac{K}{N}\sum_{j=1}^{N}\sin(\theta_j - \theta_i - \alpha) + \sin\alpha \tag{C.13}$$

where the coupling strength K and phase lag parameter α are related to the QIF model's chemical and electrical coupling strengths:

$$K = \frac{\epsilon}{\tau}\sqrt{\left(\frac{J}{\pi}\right)^2 + g^2} \tag{C.14}$$

$$\alpha = \arctan\left(\frac{J/\pi}{g}\right) \tag{C.15}$$

References

[1] D. M. Abrams and S. H. Strogatz. "Chimera States for Coupled Oscillators". *Phys. Rev. Lett.* 93 (2004), 174102.

[2] D. M. Abrams et al. "Solvable Model for Chimera States of Coupled Oscillators". *Phys. Rev. Lett.* 101 (2008), 084103.

[3] R. G. Andrzejak et al. "All together now: Analogies between chimera state collapses and epileptic seizures". *Sci. Rep.* 6 (2016), 23000.

[4] S. Ares et al. "Collective modes of coupled phase oscillators with delayed coupling". *Phys. Rev. Lett.* 108 (2012), 204101.

[5] P. Ashwin, S. Coombes, and R. Nicks. "Mathematical frameworks for oscillatory network dynamics in neuroscience". *J. Math. Neurosci.* 6 (2016), 1–92.

[6] B. C. Bag, K. Petrosyan, and C.-K. Hu. "Influence of noise on the synchronization of the stochastic Kuramoto model". *Phys. Rev. E* 76 (2007), 056210.

[7] T. Banerjee et al. "Networks of coupled oscillators: From phase to amplitude chimeras". *Chaos* 28 (2018).

[8] B. K. Bera et al. "Spike chimera states and firing regularities in neuronal hypernetworks". *Chaos* 29 (2019).

[9] F. Böhm et al. "Amplitude-phase coupling drives chimera states in globally coupled laser networks". *Phys. Rev. E* 91 (2015), 040901.

[10] M. I. Bolotov, G. V. Osipov, and A. Pikovsky. "Marginal chimera state at cross-frequency locking of pulse-coupled neural networks". *Phys. Rev. E* 93 (2016), 032202.

[11] M. I. Bolotov et al. "Breathing chimera in a system of phase oscillators". *JETP Lett.* 106 (2017), 393–399.

[12] T. Bountis et al. "Chimera states in a two–population network of coupled pendulum–like elements". *Eur. Phys. J. Spec. Top.* 223 (2014), 721–728.

[13] M. Breakspear, S. Heitmann, and A. Daffertshofer. "Generative models of cortical oscillations: neurobiological implications of the Kuramoto model". *Front. Hum. Neurosci.* 4 (2010), 190.

[14] P. Brown. "Oscillatory nature of human basal ganglia activity: relationship to the pathophysiology of Parkinson's disease". *J. Mov. Disord.* 18 (2003), 357–363.

[15] J. Buck and E. Buck. "Mechanism of Rhythmic Synchronous Flashing of Fireflies". *Science* 159 (1968), 1319–1327.

[16] A. Buscarino et al. "Dynamical network interactions in distributed control of robots". *Chaos* 16 (2006), 015116.

[17] A. Buscarino et al. "Interaction between synchronization and motion in a system of mobile agents". *Chaos* 26 (2016), 116302.

[18] J. Cabral et al. "Role of local network oscillations in resting-state functional connectivity". *Neuroimage* 57 (2011), 130–139.

[19] P. L. Carlen et al. "The role of gap junctions in seizures". *Brain Res. Rev.* 32 (2000), 235–241.

[20] H. Choi and S. Mihalas. "Synchronization dependent on spatial structures of a mesoscopic whole-brain network". *PLOS Comput. Biol.* 15 (2019), e1006978.

[21] M. Choi et al. "Synchronization in a system of globally coupled oscillators with time delay". *Phys. Rev. E* 61 (2000), 371.

[22] D. Chowdhury and M. Cross. "Synchronization of oscillators with long-range power law interactions". *Phys. Rev. E* 82 (2010), 016205.

[23] A. L. Christensen, R. O'Grady, and M. Dorigo. "From fireflies to fault-tolerant swarms of robots". *IEEE Trans. Evol. Comput.* 13 (2009), 754–766.

[24] P. Clusella, B. Pietras, and E. Montbrió. "Kuramoto model for populations of quadratic integrate-and-fire neurons with chemical and electrical coupling". *Chaos* 32 (2022), 013105.

[25] J. J. Collins and I. N. Stewart. "Coupled nonlinear oscillators and the symmetries of animal gaits". *J. Nonlinear Sci.* 3 (1993), 349–392.

[26] S. Danø, P. G. Sørensen, and F. Hynne. "Sustained oscillations in living cells". *Nature* 402 (1999), 320–322.

[27] L. G. Dominguez et al. "Enhanced synchrony in epileptiform activity? Local versus distant phase synchronization in generalized seizures". *J. Neurosci.* 25 (2005), 8077–8084.

[28] F. Dorfler and F. Bullo. "Synchronization and transient stability in power networks and nonuniform Kuramoto oscillators". *SIAM J. Control Optim.* 50 (2012), 1616–1642.

[29] F. Dörfler, M. Chertkov, and F. Bullo. "Synchronization in complex oscillator networks and smart grids". *Proc. Natl. Acad. Sci. U. S. A.* 110 (2013), 2005–2010.

[30] Y. Duguet and Y. L. Maistrenko. "Loss of coherence among coupled oscillators: From defect states to phase turbulence". *Chaos* 29 (2019), 121103.

[31] O. D'Huys et al. "Synchronization properties of network motifs: Influence of coupling delay and symmetry". *Chaos* 18 (2008).

[32] M. G. Earl and S. H. Strogatz. "Synchronization in oscillator networks with delayed coupling: A stability criterion". *Phys. Rev. E* 67 (2003), 036204.

[33] G. B. Ermentrout and N. Kopell. "Parabolic bursting in an excitable system coupled with a slow oscillation". *SIAM J. Appl. Math.* 46 (1986), 233–253.

[34] J. Fell and N. Axmacher. "The role of phase synchronization in memory processes". *Nat. Rev. Neurosci.* 12 (2011), 105–118.

[35] G. Filatrella, A. H. Nielsen, and N. F. Pedersen. "Analysis of a power grid using a Kuramoto-like model". *Eur. Phys. J. B* 61 (2008), 485–491.

[36] P. Fries. "A mechanism for cognitive dynamics: neuronal communication through neuronal coherence". *Trends Cogn. Sci.* 9 (2005), 474–480.

[37] P. Fries. "Neuronal gamma-band synchronization as a fundamental process in cortical computation". *Annu. Rev. Neurosci.* 32 (2009), 209–224.

[38] N. Fujiwara, J. Kurths, and A. Díaz-Guilera. "Synchronization in networks of mobile oscillators". *Phys. Rev. E* 83 (2011), 025101(R).

[39] N. Fujiwara, J. Kurths, and A. Díaz-Guilera. "Synchronization of mobile chaotic oscillator networks". *Chaos* 26 (2016), 094824.

[40] L. V. Gambuzza et al. "Experimental investigation of chimera states with quiescent and synchronous domains in coupled electronic oscillators". *Phys. Rev. E* 90 (2014), 032905.

[41] A. Ghosh, B Chance, and E. Pye. "Metabolic coupling and synchronization of NADH oscillations in yeast cell populations". *Arch. Biochem. Biophys.* 145 (1971), 319–331.

[42] S. Ghosh and S. Jalan. "Emergence of chimera in multiplex network". *Int. J. Bifurc. Chaos* 26 (2016), 1650120.

[43] G. Giacomin, K. Pakdaman, and X. Pellegrin. "Global attractor and asymptotic dynamics in the Kuramoto model for coupled noisy phase oscillators". *Nonlinearity* 25 (2012), 1247.

[44] W. Gilpin, M. S. Bull, and M. Prakash. "The multiscale physics of cilia and flagella". *Nat. Rev. Phys.* 2 (2020), 74–88.

[45] T. Girnyk, M. Hasler, and Y. Maistrenko. "Multistability of twisted states in non-locally coupled Kuramoto-type models". *Chaos* 22 (2012).

[46] K. Glomb et al. "Computational models in electroencephalography". *Brain Topogr.* 35 (2022), 142–161.

[47] J. Gómez-Gardenes et al. "Motion-induced synchronization in metapopulations of mobile agents". *Phys. Rev. E* 87 (2013), 032814.

[48] J. C. González-Avella, M. G. Cosenza, and M. San Miguel. "Localized coherence in two interacting populations of social agents". *Physica A* 399 (2014), 24–30.

[49] R. Gopal et al. "Observation and characterization of chimera states in coupled dynamical systems with nonlocal coupling". *Phys. Rev. E* 89 (2014), 052914.

[50] M. V. Goremyko et al. "Numerical analysis of the chimera states in the multilayered network model". *Dynamics and Fluctuations in Biomedical Photonics XIV*. Vol. 10063. 2017, 212–217.

[51] M. V. Goremyko et al. "Interaction of chimera states in a multilayered network of nonlocally coupled oscillators". *Tech. Phys. Lett.* 43 (2017), 712–715.

[52] P. Hagmann et al. "Mapping the structural core of human cerebral cortex". *PLOS Biol.* 6 (2008), e159.

[53] C. Hammond, H. Bergman, and P. Brown. "Pathological synchronization in Parkinson's disease: networks, models and treatments". *Trends Neurosci.* 30 (2007), 357–364.

[54] S. W. Haugland, L. Schmidt, and K. Krischer. "Self-organized alternating chimera states in oscillatory media". *Sci. Rep.* 5 (2015), 9883.

[55] G. Heimer et al. "Synchronizing activity of basal ganglia and pathophysiology of Parkinson's disease". *Parkinson's Disease and Related Disorders*. Vienna: Springer Vienna, 2006, 17–20.

[56] S. Herculano-Houzel. "The human brain in numbers: a linearly scaled-up primate brain". *Front. Hum. Neurosci.* 3 (2009), 857.

[57] H. Hinrichsen. "Non-equilibrium critical phenomena and phase transitions into absorbing states". *Adv. Phys.* 49 (2000), 815–958.

[58] H. Hinrichsen. "Stochastic lattice models with several absorbing states". *Phys. Rev. E* 55 (1997), 219–226.

[59] A. L. Hodgkin and A. F. Huxley. "A quantitative description of membrane current and its application to conduction and excitation in nerve". *Physiol. J.* 117 (1952), 500.

[60] A. B. Holder, M. L. Zuparic, and A. C. Kalloniatis. "Gaussian noise and the two-network frustrated Kuramoto model". *Physica D* 341 (2017), 10–32.

[61] P. Hövel et al. "Chimera states in neuronal systems of excitability type-i". *Proceedings of ECCS 2014: European Conference on Complex Systems*. Springer. 2016, 247–258.

[62] E. M. Izhikevich. "Phase models with explicit time delays". *Phys. Rev. E* 58 (1998), 905.

[63] P. Jaros et al. "Multi-headed chimera states in coupled pendula". *Eur. Phys. J. Spec. Top.* 224 (2015), 1605–1617.

[64] K. Jung, S. B. Eickhoff, and O. V. Popovych. "Tractography density affects whole-brain structural architecture and resting-state dynamical modeling". *NeuroImage* 237 (2021), 118176.

[65] V. Kaminker and R. Wackerbauer. "Alternating activity patterns and a chimeralike state in a network of globally coupled excitable Morris-Lecar neurons". *Chaos* 29 (2019).

[66] L. Kang et al. "A two-layered brain network model and its chimera state". *Sci. Rep.* 9 (2019), 14389.

[67] T. Kapitaniak et al. "Imperfect chimera states for coupled pendula". *Sci. Rep.* 4 (2014), 6379.

[68] K. Kawase and N. Uchida. *Critical Behavior at the Onset of Multichimera States in a Coupled-Oscillator Array*. 2019. arXiv: 1907.07285.

[69] J. Kelso. *Dynamic patterns: The self-organization of brain and behavior*. MIT Press, 1995.

[70] P.-J. Kim et al. "Pattern formation in a two-dimensional array of oscillators with phase-shifted coupling". *Phys. Rev. E* 70 (2004), 065201.

[71] C. Kirst, M. Timme, and D. Battaglia. "Dynamic information routing in complex networks". *Nat. Commun.* 7 (2016), 11061.

[72] T. König et al. "Decreased EEG synchronization in Alzheimer's disease and mild cognitive impairment". *Neurobiol. Aging* 26 (2005), 165–171.

[73] Y Kuramoto and D Battogtokh. "Coexistence of Coherence and Incoherence in Nonlocally Coupled Phase Oscillators". *Nonlin. Phenom. Complex Syst.* 5 (2002), 380–385.

[74] Y. Kuramoto. "Self-entrainment of a population of coupled non-linear oscillators". *International Symposium on Mathematical Problems in Theoretical Physics: January 23–29, 1975, Kyoto University, Kyoto/Japan*. Springer. 1975, 420–422.

[75] C. R. Laing. "Chimera states in heterogeneous networks". *Chaos* 19 (2009).

[76] C. R. Laing. "Chimeras on a ring of oscillator populations". *Chaos* 33 (2023).

[77] C. R. Laing. "Disorder-induced dynamics in a pair of coupled heterogeneous phase oscillator networks". *Chaos* 22 (2012).

[78] C. R. Laing. "The dynamics of chimera states in heterogeneous Kuramoto networks". *Physica D* 238 (2009), 1569–1588.

[79] C. R. Laing, K. Rajendran, and I. G. Kevrekidis. "Chimeras in random non-complete networks of phase oscillators". *Chaos* 22 (2012).

[80] K. Lehnertz et al. "Synchronization phenomena in human epileptic brain networks". *J. Neurosci. Methods* 183 (2009), 42–48.

[81] J.-C. Leloup and A. Goldbeter. "Modeling the circadian clock: from molecular mechanism to physiological disorders". *Bioessays* 30 (2008), 590–600.

[82] G. Lemoult et al. "Directed percolation phase transition to sustained turbulence in Couette flow". *Nat. Phys.* 12 (2016), 254–258.

[83] B. Li and N. Uchida. "Effect of mobility on collective phase dynamics of nonlocally coupled oscillators with a phase lag". *Phys. Rev. E* 106 (2022), 054210.

[84] B. Li and N. Uchida. "Large-scale spatiotemporal patterns in a ring of nonlocally coupled oscillators with a repulsive coupling". *Phys. Rev. E* 104 (2021), 054210.

[85] B. Li and N. Uchida. "Metastability of multi-population Kuramoto–Sakaguchi oscillators". *Chaos* 35 (2025), 013105.

[86] X. Li, T. Xu, and J. Li. "Synchronization and chimera states in a multilayer neuronal network with unidirectional interlayer links". *Eur. Phys. J. Spec. Top.* 228 (2019), 2419–2427.

[87] C. Liu et al. "Cellular Construction of a Circadian Clock: Period Determination in the Suprachiasmatic Nuclei". *Cell* 91 (1997), 855–860.

[88] Y. Liu et al. "Chimera state in a two-dimensional network of coupled genetic oscillators". *EPL* 127 (2019), 40001.

[89] N. Lotfi and A. H. Darooneh. "Existence of chimera-like state in community structured networks". *Int. J. Mod. Phys. C* 31.05 (2020), 2050069.

[90] R. Ma, J. Wang, and Z. Liu. "Robust features of chimera states and the implementation of alternating chimera states". *EPL* 91 (2010), 40006.

[91] Y. L. Maistrenko et al. "Cascades of multiheaded chimera states for coupled phase oscillators". *Int. J. Bifurcation Chaos Appl. Sci. Eng.* 24 (2014), 1440014.

[92] S. Majhi and D. Ghosh. "Alternating chimeras in networks of ephaptically coupled bursting neurons". *Chaos* 28 (2018).

[93] S. Majhi and D. Ghosh. "Amplitude death and resurgence of oscillation in networks of mobile oscillators". *EPL* 118 (2017), 40002.

[94] S. Majhi et al. "Chimera states in neuronal networks: A review". *Phys. Life Rev.* 28 (2019), 100–121.

[95] E. A. Martens. "Bistable chimera attractors on a triangular network of oscillator populations". *Phys. Rev. E* 82 (2010), 016216.

[96] E. A. Martens. "Chimeras in a network of three oscillator populations with varying network topology". *Chaos* 20 (2010).

[97] E. A. Martens, C. Bick, and M. J. Panaggio. "Chimera states in two populations with heterogeneous phase-lag". *Chaos* 26 (2016), 094819.

[98] E. A. Martens et al. "Chimera states in mechanical oscillator networks". *Proc. Natl. Acad. Sci. U. S. A.* 110 (2013), 10563–10567.

[99] T. M. Massie et al. "Cycles, phase synchronization, and entrainment in single-species phytoplankton populations". *Proc. Natl. Acad. Sci. U. S. A.* 107 (2010), 4236–4241.

[100] A. Mihara and R. O. Medrano-T. "Stability in the Kuramoto–Sakaguchi model for finite networks of identical oscillators". *Nonlinear Dyn.* 98 (2019), 539–550.

[101] A. Mishra et al. "Traveling chimera pattern in a neuronal network under local gap junctional and nonlocal chemical synaptic interactions". *Opera Med. Physiol.* 1 (2017), 14–18.

[102] E. Montbrió, D. Pazó, and J. Schmidt. "Time delay in the Kuramoto model with bimodal frequency distribution". *Phys. Rev. E* 74 (2006), 056201.

[103] A. E. Motter et al. "Spontaneous synchrony in power-grid networks". *Nat. Phys.* 9 (2013), 191–197.

[104] L. Mukhametov, A. Y. Supin, and I. Polyakova. "Interhemispheric asymmetry of the electroencephalographic sleep patterns in dolphins". *Brain Res.* (1977).

[105] R. Mukherjee and A. Sen. "Amplitude mediated chimera states with active and inactive oscillators". *Chaos* 28 (2018).

[106] S. Nkomo, M. R. Tinsley, and K. Showalter. "Chimera and chimera-like states in populations of nonlocally coupled homogeneous and heterogeneous chemical oscillators". *Chaos* 26 (2016), 094826.

[107] S. Nkomo, M. R. Tinsley, and K. Showalter. "Chimera states in populations of nonlocally coupled chemical oscillators". *Phys. Rev. Lett.* 110 (2013), 244102.

[108] R. Noori et al. "Activity-dependent myelination: A glial mechanism of oscillatory self-organization in large-scale brain networks". *Proc. Natl. Acad. Sci. U. S. A.* 117 (2020), 13227–13237.

[109] A. Nordenfelt, A. Wagemakers, and M. A. Sanjuán. "Frequency dispersion in the time-delayed Kuramoto model". *Phys. Rev. E* 89 (2014), 032905.

[110] G. Ódor, J. Kelling, and G. Deco. "The effect of noise on the synchronization dynamics of the Kuramoto model on a large human connectome graph". *Neurocomputing* 461 (2021), 696–704.

[111] K. P. O'Keeffe, H. Hong, and S. H. Strogatz. "Oscillators that sync and swarm". *Nat. Commun.* 8 (2017), 1–13.

[112] I. Omelchenko et al. "Nonlinearity of local dynamics promotes multi-chimeras". *Chaos* 25 (2015), 083104.

[113] I. Omelchenko et al. "When Nonlocal Coupling between Oscillators Becomes Stronger: Patched Synchrony or Multichimera States". *Phys. Rev. Lett.* 110 (2013), 224101.

[114] O. E. Omel'chenko and E. Knobloch. "Chimerapedia: coherence–incoherence patterns in one, two and three dimensions". *New J. Phys* 21 (2019), 093034.

[115] E. Ott and T. M. Antonsen. "Low dimensional behavior of large systems of globally coupled oscillators". *Chaos* 18 (2008), 037113.

[116] J. C. Pang, L. L. Gollo, and J. A. Roberts. "Stochastic synchronization of dynamics on the human connectome". *NeuroImage* 229 (2021), 117738.

[117] F. Parastesh et al. "Synchronization patterns in a blinking multilayer neuronal network". *Eur. Phys. J. Spec. Top.* 228 (2019), 2465–2474.

[118] F. Peruani, E. M. Nicola, and L. G. Morelli. "Mobility induces global synchronization of oscillators in periodic extended systems". *New J. Phys.* 12 (2010), 093029.

[119] S. Petkoski, J. M. Palva, and V. K. Jirsa. "Phase-lags in large scale brain synchronization: Methodological considerations and in-silico analysis". *PLOS Comput. Biol.* 14 (2018), e1006160.

[120] S. Petkoski et al. "Heterogeneity of time delays determines synchronization of coupled oscillators". *Phys. Rev. E* 94 (2016), 012209.

[121] G. Petrungaro, K. Uriu, and L. G. Morelli. "Mobility-induced persistent chimera states". *Phys. Rev. E* 96 (2017), 062210.

[122] G. Petrungaro, K. Uriu, and L. G. Morelli. "Synchronization dynamics of mobile oscillators in the presence of coupling delays". *Phys. Rev. E* 99 (2019), 062207.

[123] B. Pietras and A. Daffertshofer. "Network dynamics of coupled oscillators and phase reduction techniques". *Phys. Rep.* 819 (2019), 1–105.

[124] A. Pikovsky, M. Rosenblum, and J. Kurths. *Synchronization: A Universal Concept in Nonlinear Sciences*. Cambridge: Cambridge University Press, 2001.

[125] A. Ponce-Alvarez et al. "Resting-state temporal synchronization networks emerge from connectivity topology and heterogeneity". *PLOS Comput. Biol.* 11 (2015), e1004100.

[126] D. Popa, A. T. Popescu, and D. Paré. "Contrasting activity profile of two distributed cortical networks as a function of attentional demands". *J. Neurosci.* 29 (2009), 1191–1201.

[127] N. C. Rattenborg, C. J. Amlaner, and S. L. Lima. "Behavioral, neurophysiological and evolutionary perspectives on unihemispheric sleep". *Neurosci. Biobehav. Rev.* 24 (2000), 817–842.

[128] N. C. Rattenborg. "Do birds sleep in flight?" *Naturwissenschaften* 93 (2006), 413–425.

[129] J. A. Roberts et al. "Metastable brain waves". *Nat. Commun.* 10 (2019), 1056.

[130] D. P. Rosin et al. "Transient scaling and resurgence of chimera states in networks of Boolean phase oscillators". *Phys. Rev. E* 90 (2014), 030902.

[131] A Rothkegel and K. Lehnertz. "Irregular macroscopic dynamics due to chimera states in small-world networks of pulse-coupled oscillators". *New J. Phys.* 16 (2014), 055006.

[132] C. Rummel et al. "A systems-level approach to human epileptic seizures". *Neuroinformatics* 11 (2013), 159–173.

[133] H. Sakaguchi and Y. Kuramoto. "A soluble active rotater model showing phase transitions via mutual entertainment". *Prog. Theor. Phys.* 76 (1986), 576–581.

[134] M. Sano and K. Tamai. "A universal transition to turbulence in channel flow". *Nat. Phys.* 12 (2016), 249–253.

[135] R. Schmidt et al. "Kuramoto model simulation of neural hubs and dynamic synchrony in the human cerebral connectome". *BMC Neurosci.* 16 (2015), 1–13.

[136] E. Schöll. "Synchronization patterns and chimera states in complex networks: Interplay of topology and dynamics". *Eur. Phys. J. Spec. Top.* 225 (2016), 891–919.

[137] H. G. Schuster and P. Wagner. "Mutual entrainment of two limit cycle oscillators with time delayed coupling". *Prog. Theor. Phys.* 81 (1989), 939–945.

[138] G. C. Sethia, A. Sen, and G. L. Johnston. "Amplitude-mediated chimera states". *Phys. Rev. E* 88 (2013), 042917.

[139] M. Shanahan. "Metastable chimera states in community-structured oscillator networks". *Chaos* 20 (2010).

[140] J. Shena et al. “Turbulent chimeras in large semiconductor laser arrays”. *Sci. Rep.* 7 (2017), 1–8.

[141] I. A. Shepelev et al. “New type of chimera structures in a ring of bistable FitzHugh–Nagumo oscillators with nonlocal interaction”. *Phys. Lett. A* 381 (2017), 1398–1404.

[142] S.-i. Shima and Y. Kuramoto. “Rotating spiral waves with phase-randomized core in nonlocally coupled oscillators”. *Phys. Rev. E* 69 (2004), 036213.

[143] F. Sivrikaya and B. Yener. “Time synchronization in sensor networks: a survey”. *IEEE Netw.* 18 (2004), 45–50.

[144] P. S. Skardal and J. G. Restrepo. “Hierarchical synchrony of phase oscillators in modular networks”. *Phys. Rev. E* 85 (2012), 016208.

[145] L. Smirnov et al. “Disorder fosters chimera in an array of motile particles”. *Phys. Rev. E* 104 (2021), 034205.

[146] J. C. Smith et al. “Pre-Bötzinger complex: a brainstem region that may generate respiratory rhythm in mammals”. *Science* 254 (1991), 726–729.

[147] S. H. Strogatz, R. E. Kronauer, and C. A. Czeisler. “Circadian pacemaker interferes with sleep onset at specific times each day: role in insomnia”. *Am. J. Physiol. Regul. Integr. Comp. Physiol.* 253 (1987), R172–R178.

[148] S. H. Strogatz et al. “Crowd synchrony on the Millennium Bridge”. *Nature* 438 (2005), 43–44.

[149] A. Takamatsu, T. Fujii, and I. Endo. “Time delay effect in a living coupled oscillator system with the plasmodium of Physarum polycephalum”. *Phys. Rev. Lett.* 85 (2000), 2026.

[150] K. A. Takeuchi et al. “Directed Percolation Criticality in Turbulent Liquid Crystals”. *Phys. Rev. Lett.* 99 (2007), 234503.

[151] D. Tanaka. “General chemotactic model of oscillators”. *Phys. Rev. Lett.* 99 (2007), 134103.

[152] J. Tang et al. “Noise and delay sustained chimera state in small world neuronal network”. *Sci. China Technol. Sci.* 62 (2019), 1134–1140.

[153] P. Tewarie et al. “Interlayer connectivity reconstruction for multilayer brain networks using phase oscillator models”. *New J. Phys.* 23 (2021), 063065.

[154] M. R. Tinsley, S. Nkomo, and K. Showalter. "Chimera and phase-cluster states in populations of coupled chemical oscillators". *Nat. Phys.* 8 (2012), 662–665.

[155] R. I. Tivadar and M. M. Murray. "A primer on electroencephalography and event-related potentials for organizational neuroscience". *Organ. Res. Methods* 22 (2019), 69–94.

[156] E. Tognoli and J. S. Kelso. "Brain coordination dynamics: true and false faces of phase synchrony and metastability". *Prog. Neurobiol.* 87 (2009), 31–40.

[157] E. Tognoli and J. S. Kelso. "The metastable brain". *Neuron* 81 (2014), 35–48.

[158] J. F. Totz et al. "Spiral wave chimera states in large populations of coupled chemical oscillators". *Nat. Phys.* 14 (2018), 282–285.

[159] N. Tsigkri-DeSmedt et al. "Multi-chimera States in the Leaky Integrate-and-Fire Model". *Procedia Comput. Sci.* 66 (2015). 4th International Young Scientist Conference on Computational Science, 13–22.

[160] L. Tumash et al. "Stability of amplitude chimeras in oscillator networks". *EPL* 117 (2017), 20001.

[161] N. Uchida. "Many-Body Theory of Synchronization by Long-Range Interactions". *Phys. Rev. Lett.* 106 (2011), 064101.

[162] P. J. Uhlhaas and W. Singer. "Neural Synchrony in Brain Disorders: Relevance for Cognitive Dysfunctions and Pathophysiology". *Neuron* 52 (2006), 155–168.

[163] K. Uriu et al. "Dynamics of mobile coupled phase oscillators". *Phys. Rev. E* 87 (2013), 032911.

[164] P. Villegas, P. Moretti, and M. A. Munoz. "Frustrated hierarchical synchronization and emergent complexity in the human connectome network". *Sci. Rep.* 4 (2014), 5990.

[165] W.-H. Wang et al. "Chimera dynamics in nonlocally coupled moving phase oscillators". *Front. Phys.* 14 (2019), 1–8.

[166] X.-J. Wang. "Neurophysiological and computational principles of cortical rhythms in cognition". *Physiol. Rev.* 90 (2010), 1195–1268.

[167] Z. Wang and Z. Liu. "A brief review of chimera state in empirical brain networks". *Front. Physiol.* 11 (2020), 532099.

[168] G. Weerasinghe et al. "Optimal closed-loop deep brain stimulation using multiple independently controlled contacts". *PLOS Comput. Biol.* 17 (2021), e1009281.

[169] D. A. Wiley, S. H. Strogatz, and M. Girvan. "The size of the sync basin". *Chaos* 16 (2006), 015103.

[170] H. R. Wilson and J. D. Cowan. "Excitatory and inhibitory interactions in localized populations of model neurons". *Biophys. J.* 12 (1972), 1–24.

[171] J. Xie, E. Knobloch, and H.-C. Kao. "Multicluster and traveling chimera states in nonlocal phase-coupled oscillators". *Phys. Rev. E* 90 (2014), 022919.

[172] M. S. Yeung and S. H. Strogatz. "Time delay in the Kuramoto model of coupled oscillators". *Phys. Rev. Lett.* 82 (1999), 648.

[173] A. Zakharova, M. Kapeller, and E. Schöll. "Amplitude chimeras and chimera death in dynamical networks". *J. Phys. Conf. Ser.* Vol. 727. 1. IOP Publishing. 2016, 012018.

[174] A. Zakharova, M. Kapeller, and E. Schöll. "Chimera Death: Symmetry Breaking in Dynamical Networks". *Phys. Rev. Lett.* 112 (2014), 154101.

[175] Y. Zhu, Z. Zheng, and J. Yang. "Chimera states on complex networks". *Phys. Rev. E* 89 (2014), 022914.

[176] A. Ziaeemehr et al. "Frequency-dependent organization of the brain's functional network through delayed-interactions". *Neural Netw.* 132 (2020), 155–165.

List of Work

Papers

- B. Li and N. Uchida, "Large-scale spatiotemporal patterns in a ring of nonlocally coupled oscillators with a repulsive coupling", *Phys. Rev. E* **104**, 054210 (2021).
- B. Li and N. Uchida, "Effect of mobility on collective phase dynamics of nonlocally coupled oscillators with a phase lag", *Phys. Rev. E* **106**, 054210 (2022).
- B. Li and N. Uchida, "Metastability of multi-population Kuramoto-Sakaguchi oscillators", *Chaos* **35**, 013105 (2025).

Conference Posters

- B. Li and N. Uchida, "The analogy between multi-twisted states in 1-dimensional nonlocal coupled oscillator array and absorbing state transition", JPS 2021 Autumn Meeting (21pPSL-23), 2021.9.21, online
- B. Li and N. Uchida, "Collective phase dynamics of non-locally coupled mobile oscillators with a phase lag", JPS 2023 Spring Meeting (22pPSL-22), 2023.3.22, online
- B. Li and N. Uchida, "Collective dynamics of nonlocally-coupled phase oscillators with phase lag and mobility", STATPHYS28 (PSa-127), 2023.8.7, Tokyo

Acknowledgements

First and foremost, I would like to express my deepest gratitude to my advisor, Professor Uchida, for his invaluable guidance and support throughout my research journey. His insightful advice and meticulous feedback on my thesis have been instrumental in shaping this work.

I am also deeply thankful to my labmates in the research group. The discussions during seminars and casual interactions have significantly made my research experience both productive and enjoyable.

I extend my heartfelt thanks to Professor Kawakatsu and the members of Nakayoshi Seminar for their thoughtful suggestions and encouragement. Their feedback has broadened my perspective and contributed greatly to the refinement of my work.

To my parents, I owe my deepest appreciation for their unwavering support and encouragement throughout my academic journey. Their belief in my abilities has been a constant source of motivation, and their sacrifices have provided me with the foundation to pursue my dreams.

I am grateful for the financial support provided by the JST and Tohoku university (Grant Number JPMJFS2102 and JPMJSP2114) that made this research possible. The research grants not only supported my academic endeavors but also eased the financial burden of living expenses, allowing me to focus wholeheartedly on my studies.

Finally, I would like to acknowledge all the teachers, friends, and colleagues who have supported me in ways big and small during this journey. Whether through kind words, intellectual stimulation, or moral support, their contributions have been invaluable in shaping both this work and my personal growth.

To everyone who has walked alongside me during this journey, I extend my sincerest thanks.